

Automatic detection of detached and erroneous electrodes in Electrical Impedance Tomography

Yednekachew Worku Asfaw

Thesis submitted to the
Faculty of Graduate and Postdoctoral Studies
In partial fulfilment of the requirements
For the MASc degree in Electrical Engineering

Ottawa-Carleton Institute for Electrical and Computer Engineering
School of Information Technology and Engineering
University of Ottawa

© Yednekachew Worku Asfaw, Ottawa, Canada, 2005

To my family

LIST OF ABBREVIATIONS

n	Additive Gaussian noise
Y	Admittance matrix
$\tilde{\phi}$	Approximated Potential over FEM Element
j	Boundary Current Density
BME	Boundary Element Method
e_i	Candidate electrode
$\Delta\sigma$	Change in conductivity
x	Change in log conductivity
$\delta\mathbf{H}^{(r)}$	Change in sensitivity matrix for electrode r
$\Delta\mathbf{u}$	Change in voltage electrode potentials
CT	Computed Tomography
σ	Conductivity
\mathbf{R}_x	Co-variance for x
\mathbf{R}_n	Co-variance for noise
J	Current Density
$D(\xi)$	Difference between $F(\xi)$ and voltage measurements
\mathbf{z}_j	Difference measurements from e_j
z	Difference voltage measurement
EIDORS	Electrical Impedance and Diffuse Optical Reconstruction Software
E	Electric Field
EIT	Electrical Impedance Tomography
ECG	Electrocardiogram
EEG	Electroencephalogram
EM	Expectation Maximization
EMG	Electromyogram
$\hat{\mathbf{z}}_j$	Estimate of \mathbf{z}_j
E_j	Estimation error or norm of the difference between \mathbf{z}_j and $\hat{\mathbf{z}}_j$

ϕ_i	FEM nodal potential values
N_i	FEM Basis functions
FEM	Finite Element Method
x	General input signal
y	General output signal
μ	Hyper parameter value
ISRA	Image Space Restoration Algorithm
\mathbf{x}_∞	Infinite mean for \mathbf{x}
\mathbf{H}_0	Initial sensitivity matrix
MAP	Maximum <i>a posteriori</i>
MRI	Magnetic Resonance Imaging
ML	Maximum Likelihood
MVC	Maximum Voluntary Contraction
Ω	Medium
$\partial \Omega$	Medium Boundary
$F(\xi)$	Non-linear forward operator
PET	Positron Emission Tomography
PER	Prediction Error Ratio
\mathbf{B}	Reconstruction matrix
$\mathbf{B}(e_i, e_j)$	Reconstruction matrix without contributions from electrodes e_i and e_j .
\mathbf{Q}	Regularization matrix
ϕ	Scalar Potential
\mathbf{S}_j	Selector matrix of e_j
\mathbf{H}	Sensitivity matrix
S	Set containing all electrodes
S'	Set without e_i
SNR	Signal to Noise Ratio
SVD	Singular Value Decomposition
T_i	Sum of E_j for candidate electrode e_i

D_i	Total difference of T_i from other T values
C	Vector of injection current values
p	Vector of unknown nodal, voltage and current electrode potentials
u	Voltage electrode potentials
W	Weights for compensation using regularization scheme

ABSTRACT

Electrical Impedance Tomography (EIT) is an imaging technique which calculates the conductivity distribution within a medium from voltage measurements made at a series of electrodes on the medium's surface. Unfortunately, the electrodes can become detached or poorly connected, such that the measured data cannot be used. This thesis presents an automatic approach to detect such erroneous electrodes via the image reconstruction model.

The method calculates an estimate of the data at an electrode, based on the measurements from all other electrodes. In order to detect an erroneous electrode amongst N electrodes, all sets of $N-1$ electrodes are tested, and the set with the best match between measurements and estimate is identified as the one which excludes the erroneous electrode.

Tests performed on experimental data for 2D EIT showed similar classification to those made by a trained user. A detection parameter PER is developed, and a detection threshold of -22 ± 2 dB is recommended based analysis of simulated erroneous data. Extension of the method into 3D EIT showed similar results as that of 2D EIT.

ACKNOWLEDGEMENTS

I extend my sincere gratitude and appreciation to the people who made this master thesis possible. My special thanks to my supervisor Dr. Andy Adler for giving me his unrestrained advice and encouragement. His valuable suggestions during the course of the work are greatly acknowledged. In the past two years, he has taught me about the process of research and helped me develop my skills in the medical imaging field. I am grateful for the time he spent explaining the subject matter, and going over material of this thesis.

I would like to thank Richard Bayford for encouraging the original idea of the work. I am indebted to Camille and Tanya for proof reading my work. I would like to pass my sincere thanks to Armin, Lo-Sing, Victor, Tan, Tam, Richard, Liva and Mustafa for motivating and encouraging me in many ways through out our university years.

I also want to thank my family, who taught me the value of hard work by their own example. I would like to share this moment of happiness with Etete, Abeyaye, and the rest of the family who rendered me enormous support every step of the way.

Finally, I would like to thank the University of Ottawa, faculty of Engineering, for providing me with financial support.

Sincerely,

Yednekachew Asfaw

Table of Contents

LIST OF ABBREVIATIONS	ii
ABSTRACT	v
ACKNOWLEDGEMENTS	vi
Table of Contents	vii
Table of Figures	ix
Introduction	1
1.1 Clinical application of EIT.....	2
1.2 Comparison with other medical devices.....	3
1.3 Thesis objective	4
Background	6
2.1 Electrical Impedance Tomography.....	6
2.2 Finite Element method and Electromagnetism.....	8
2.2.1 Electromagnetic properties of the human body.....	8
2.2.2 Electrode Models	9
2.2.3 Forward Model and Finite Element Method.....	11
2.2.4 Finite Element Method Meshes	13
2.3 Inverse Theory and Regularization.....	15
2.3.1 Inverse Theory	15
2.3.2 EIT as ill-posed and ill-conditioned problem	16
2.3.3 Regularization Techniques.....	16
2.4 Image reconstruction in EIT	18
2.5 MAP based regularized image reconstruction	20
Characterization of Electrodes	24
3.1 Classification of Electrodes	24
3.2 Sources of error in applications using electrodes	27
3.2.1 Electrocardiogram.....	28
3.2.2 Electroencephalogram.....	28
3.2.3 Electromyography.....	30
3.3 Measurement errors and noise in EIT.....	31
3.3.1 Electronic interference.....	31
3.3.2 Hardware.....	31
3.3.3 Detached and misplaced electrodes	32
3.3.4 Electrode placement patterns and number	33
3.3.5 FEM mesh elements and electrode models.....	34
3.3.6 Non-Stationary noise and EIT	34
3.4 Electrode error compensation in EIT.....	36
3.4.1 Compensation for positional variation of electrodes	36
3.4.2 Image reconstruction with missing data	37
Electrode Error detection	39
4.1 Heuristic detection	40
4.2 Detection through image reconstruction.....	41
4.2.1 Methodology for detection.....	42
4.3 Electrode Error Detection in Static Imaging.....	45
4.4 Drive Patterns and Detection	46

4.5	Implementation	47
4.6	Data	48
4.6.1	Simulated Erroneous Data	48
4.6.2	Real Erroneous Data	50
4.7	Results	51
4.7.1	Experimental data with simulated error	51
4.7.2	Erroneous experimental data	52
4.7.3	Simulated data with error	54
4.7.4	Multiple erroneous electrodes	56
4.7.5	Compensation of erroneous data	57
4.8	Discussion	58
Error Detection in 3D EIT		60
5.1	Finite Element Model and forward problem in EIDORS3D	61
5.2	Regularization in EIDORS3D	62
5.3	Electrode error detection in EIDORS3D	63
5.4	Data	63
5.5	Result	64
5.6	Discussion	65
Detection of Multiple Erroneous Electrodes		67
6.1	Identification of Multiple erroneous electrodes	67
6.2	Multiple erroneous electrodes detection method	69
6.3	Data	71
6.4	Result	71
6.4.1	Simulated Erroneous Data	71
6.4.2	Erroneous experimental data	72
6.5	Discussion	76
Conclusion		78
Future Work.....		79
Bibliography		82
Appendix 1: Using Jackknife method for detection		89
Appendix 2: Analysis of Electrode error with time		91
Appendix 3: 2D erroneous electrode detection code.....		92
Appendix 4: 3D erroneous electrode detection code.....		96
Appendix 5: Multiple erroneous electrode detection code.....		99

Table of Figures

Figure 1.1 Human lung imaging: Inspiration and expiration.....	4
Figure 1.2 Heart activity monitor with EIT	4
Figure 2.1 Common EIT setup.....	7
Figure 2.2 Cross Section of the Human body cavity	9
Figure 2.3 Nodal Basis functions over a triangle element.....	11
Figure 2.4 Voltage and Current distribution with electrode pair [8 9].	14
Figure 2.5 Circular mesh for EIT with 256 elements, for a 16 electrode system	14
Figure 2.6 Newton Raphson Algorithm.....	19
Figure 3.1 Common surface electrode	25
Figure 3.2 Electrode-skin impedance equivalent circuit.....	25
Figure 3.3 Electrode placement on the scalp for EEG measurement	29
Figure 3.4 Example of non-stationary noise in images.....	35
Figure 3.5 Example of non-stationary signal in ECG varying over time	35
Figure 4.1 Upper threshold and lower threshold	40
Figure 4.2 Pseudo code for detection of an erroneous electrode.....	43
Figure 4.3 Illustration of electrode sets S and S'	43
Figure 4.4 Block diagram of calculation for estimation error E_j	44
Figure 4.5 Data available for an eight electrode EIT system using adjacent drive.	46
Figure 4.6 Block Diagram for generating simulated data.....	49
Figure 4.7 Reconstructed images of EIDORS3D	50
Figure 4.8 GUI used for classification of selected data by expert users.....	51
Figure 4.9 T vs. Erroneous electrode for experimental data with simulated error.....	52
Figure 4.10 Electrode detection in real data.	53
Figure 4.11 WGN to clean data: 0dB noise has a visually little imperceptible impact	54
Figure 4.12 SNR vs. PER (\pm std dev) on simulated data.....	55
Figure 4.13 T vs. Erroneous electrode for real erroneous data..	56
Figure 4.14 Compensation of Erroneous electrodes.....	57
Figure 5.1 Finite Element mesh in EIDORS3D with two electrode rings.....	61
Figure 5.2 Simulated conductivity difference.....	64
Figure 5.3 SNR vs. PER (\pm std dev)	65
Figure 6.1 Two erroneous electrodes.....	68
Figure 6.2 Estimation error scheme for two erroneous electrodes	69
Figure 6.3 Pseudo code for detection of two erroneous electrodes.	70
Figure 6.4 Detection of two erroneous electrodes using simulated noise of -10dB	72
Figure 6.5: T graph for two erroneous electrode detection.....	73
Figure 6.6 Single electrode detection method.....	74
Figure 6.7 Two electrode detection method	75
Figure A1.1 Detection using the Jackknife method: electrode 5 is erroneous.....	90
Figure A2.1 Average change of estimation error.....	91

Chapter 1

Introduction

In medical imaging, as well as in several other fields, there is interest in being able to “see inside” objects – to view the internal structure of a medium. Typically, this is accomplished using measurement devices that introduce energy and measure its interaction with the medium. For example, the chest radiograph uses X-rays to image the lungs. Similarly, Magnetic Resonance Imaging (MRI) provides 3D images of tissue based on the interaction of radio frequency energy with the hydrogen in the body, allowing imaging of the concentration of water. This thesis is concerned with Electrical Impedance Tomography (EIT), a technology to measure the internal impedance distribution using surface measurements. Electrical current is applied to the medium and the voltage at the surface is measured using electrodes; using this information, the measured voltage, injected current and geometry of the medium are then used to determine the impedance distribution. Such technologies have widespread applications, such as determining flow and contents of pipes, detection of land mines (Church *et al*, 2001) and measurement of organ function of the human body.

Currently, the most common use and research focus is for medical applications: to measure organ functions in the human body. This chapter explores the feasibility of EIT technology in clinical applications and compares it to other medical imaging technologies. Based on this background information, the goal of the thesis is discussed in the last section.

1.1 Clinical application of EIT

Medical imaging technologies may be classified using two types of imaging: anatomical imaging and functional imaging. Anatomical imaging systems can identify the location and shape of an organ; examples of such systems are Computed Tomography (CT) and Magnetic Resonance Imaging (MRI). In functional imaging, the aim is to measure the physiological processes, and the requirement for a high resolution image is much less; examples are Positron Emission Tomography (PET), angiography, and EIT.

Even though EIT images do provide the location of the organs, they cannot identify structure due to their low resolution. However, EIT is able to perform functional imaging for physiological process that causes change in impedance, such as those associated with fluid and gas movement in the body. Hence, blood or fluid circulation, respiration and digestive system activity can be imaged using EIT technology.

This thesis is especially interested in applications of EIT to study air and blood flow in the lungs. The conductivity of both air and blood contrasts with that of the surrounding tissues, where blood is more conductive than air. For example, EIT can help identify changes in conductivity pattern caused by pulmonary diseases. These diseases are classified as restrictive or obstructive: restrictive diseases decrease the tidal volume capacity of the lungs, and obstructive diseases increase resistance to airflow affecting the rate of change in the tidal volume. For example, a restrictive disease such as pulmonary edema is due to fluid accumulation in the lung. Several studies have shown EIT to be able to detect the increases in lung conductivity due to the progression of edema (e.g. Adler *et al.*, 1997). These results can aid clinicians in early diagnosis, treatment or monitoring of the pathology.

1.2 Comparison with other medical devices

According to Leksell (1991), an ideal measurement device has the following parameters: accuracy, repeatability, sensitivity, and minimal invasiveness. In addition, the device ought to be inexpensive and non-cumbersome. These criteria cannot be fulfilled by one single medical device and usually some compromise is required. In this section EIT is compared with two anatomical imaging systems, chest radiography and Magnetic Resonance Imaging (MRI), and one functional imaging system, Positron Emission Tomography (PET).

Chest radiography is a plain film x-ray of the chest. It has minimal cumbersomeness, minimal invasiveness and low cost. It allows identification of the pathologies from the characteristic of the image by trained clinicians but it cannot be used for monitoring since excessive exposure to radiation is harmful to patients.

MRI provides 3D images of tissue based on the interaction of radio frequency and water concentration of the body. MRI has the ability to measure only the lung fluids of interest while rejecting the contribution from blood fluid. The cost and cumbersomeness of the apparatus do not allow for use in patient monitoring.

PET generates a 3D image of the distribution of a radioactive tracer. By selecting a particular tracer it is possible to measure blood volume, intravascular volume, and the gas volume. But again the cost and cumbersomeness of the technique prevents it from becoming a monitoring device.

Even though EIT has low resolution images it shows significant promise as a functional lung imaging system. It is non-invasive and minimally cumbersome making it desirable for patient monitoring. In comparison to MRI and CT, it is inexpensive, requiring a small measurement system with relatively small computing power. The technique is capable of producing a low resolution cross section of the thorax in 2D; and in 3D application it is able to produce an internal image of a large portion of the thorax. Figure 1.1 shows the

cross sectional image of human lungs during quiet breathing. The change in impedance near the center of images is indicative of heart activity. Figure 1.2 shows change in impedance in the heart area and the corresponding Electrocardiogram signal. These results illustrate EIT's potential for clinical applications. Studies of sensitivity and accuracy of EIT in clinical applications are ongoing and show promising results (see chapter 3) (Blott *et al.*, 1998).

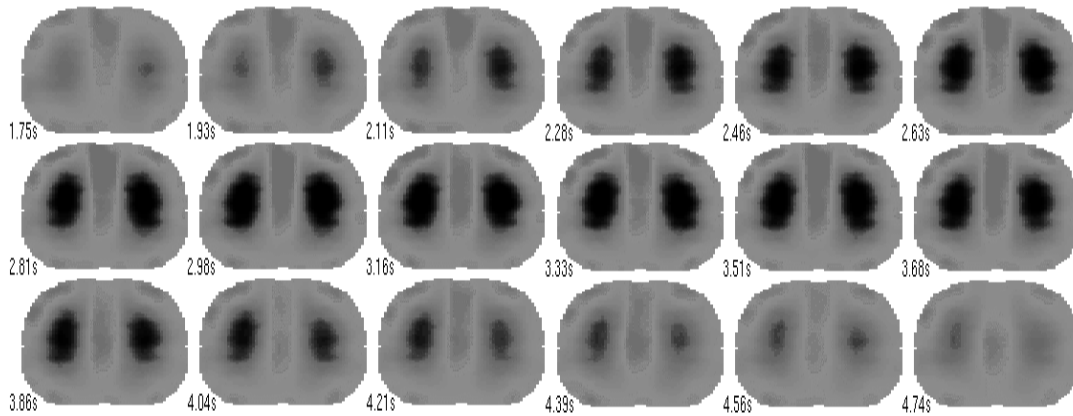


Figure 1.1 Human lung imaging: Inspiration and expiration (Adapted from Adler (1996))

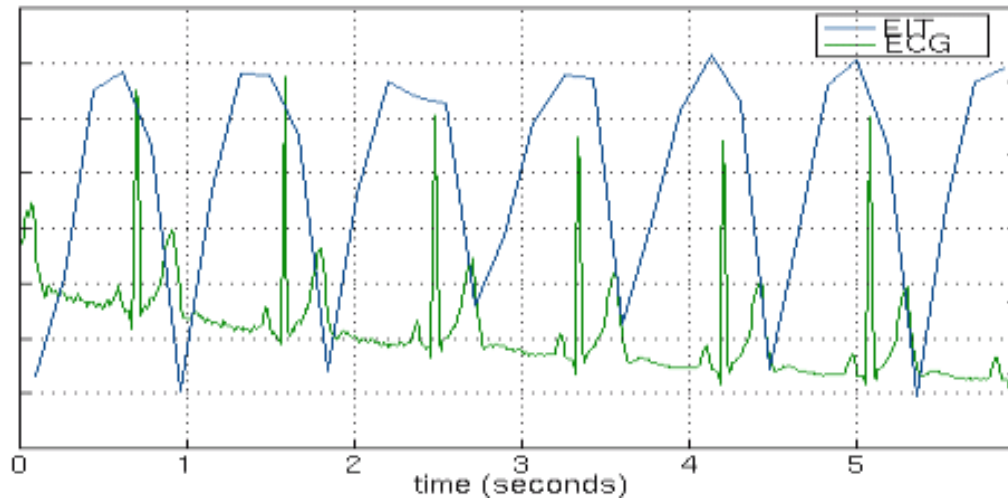


Figure 1.2 Heart activity monitor with EIT(Adapted from Adler (1996))

1.3 Thesis objective

EIT has several promising areas of clinical application. The low cost, non-cumbersomeness, and non-invasive nature of the technology makes it a good candidate for patient monitoring. For example, it is able to continuously image the heart and lungs in patients in intensive or critical care. Since EIT requires attaching several electrodes

and wires to the patient, one important difficulty with experimental and clinical EIT measurements is the care required in attaching the electrodes to ensure accurate voltage measurements. Many conditions can cause electrodes to give false readings, such as errors due to electronics noise (Al-Hatib, 1998, Meeson *et al*, 1996), and poor electrode contact due to patient movement (Blott *et al*, 1998), or sweat and peripheral edema, especially in long term monitoring applications (Lozano *et al*, 1995).

In order for EIT to become an acceptable clinical device, it is important to address the problem of erroneous data due to detached and improperly connected electrodes. In some experimental applications, erroneous data can be discarded and reproduced after correctly placing/attaching the electrode. However, in long term monitoring applications reproducing the data is impossible. In this case, given a set of data containing measurements with errors, it is desired to calculate an image based on the remaining good data. In order to accomplish this, Adler (2004) developed a methodology to reconstruct EIT images in the presence of single electrode errors. One limitation of that work is the requirement that the erroneous electrodes be identified to the algorithm by a human operator. The ability to automatically identify erroneous electrodes is a potentially important capability for clinical and experimental applications of EIT. The goal of this thesis is to develop and validate a method that automatically detects the presence and location of electrodes producing erroneous data.

Before we present the method for detection of erroneous electrodes, we discuss the physics of the problem and relevant mathematical technique in chapter 2. Chapter 3 covers the work done towards understanding the causes of errors in EIT data, and reviews methods developed for reducing those errors. In addition, other applications such as electroencephalogram (EEG) and ECG that use electrodes are explored. Chapter 4 covers the theory and results of the method developed for erroneous electrode detection for 2D EIT. Extensions of this method for 3D EIT and for multiple electrode detection are explored in chapter 5 and 6, respectively. Finally, the work is concluded in chapter 7 along with possible future work.

Chapter 2

Background

This chapter introduces the measurement systems and reconstruction algorithms for EIT. In section 2.1 we look at the most commonly used hardware setup. The mathematical approach for solving EIT is divided into two parts: the forward problem and the inverse problem. The forward problem deals with estimation of the potential distribution in the medium. The inverse problem calculates the internal impedance distribution from the voltage distribution. Section 2.2 covers a detailed analysis of the forward problem and the mathematical principle for estimation of potential inside the human body using finite element methods. The inverse problem is based on the principles of inverse theory. The concept of inverse theory and regularization is discussed in section 2.3. Section 2.4 and 2.5 discuss image reconstruction techniques that are non-regularized and regularized, respectively.

2.1 *Electrical Impedance Tomography*

EIT is an imaging technique which calculates the electrical conductivity distribution within a medium from electrical measurements made at a series of electrodes on the medium surface. EIT data are acquired by successively applying a low amplitude audio frequency current across each pair of electrodes while measuring the voltage differences produced on all other pairs of electrodes. The measurement system usually has 8, 16 or 32 electrodes; for each current pattern, all electrode pairs, except ones used for current injection, are used to measure the voltage. At each pair of electrodes, a difference signal is calculated by subtracting one voltage from the other and then amplifying the result. Data collected are then sent to the imaging system for analysis. Figure 2.1 shows a block diagram of this process.

Inside the data acquisition controller these difference signals are demodulated and read by an analog to digital converter. The demodulator reads the amplitude of the measured

difference signal while removing electrical signals produced by physiological processes (such as the ECG) by rejecting contributions to the signal that are not at the current injection frequency. After current injection and voltage reading are performed across all electrode pairs, data are sent to a computer that calculates the EIT image. This data set represents the conductivity distribution of the subject at the time of data acquisition.

EIT poses minimal electrical risk to the patient. Studies of the cutaneous sensitivity of humans to electrical simulation as a function of frequency indicates the sensitivity is quite high to current at low frequencies, but it decreases significantly with increasing frequency (Dalziel, 1956; Geddes, 1971). For the experimental data used in this thesis, the current (1mA) used was approximately one tenth of the level required for perception. The current levels required to cause muscle contraction for cutaneous current injection are more than ten times higher than the perception values (Adler, 1995).

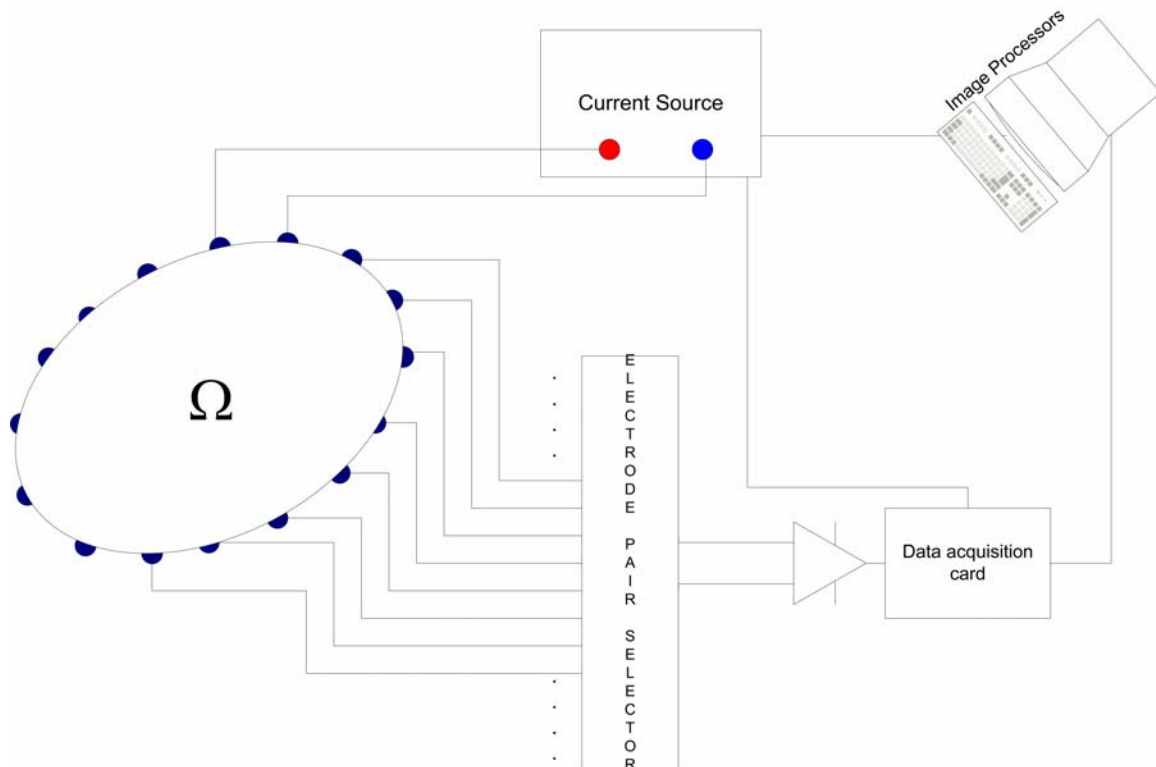


Figure 2.1 Common EIT setup

2.2 *Finite Element method and Electromagnetism*

The electrical potential inside the human body is calculated from Maxwell's equations using the finite element method. Appropriate modelling of the body/electrode interface is necessary to define the boundary conditions. This section covers these issues in detail starting with the electromagnetic properties of the human body. It is followed by a section that explores the various ways the body/electrodes can be modelled. Finally, the finite element method is described and the forward problem is formalized.

2.2.1 **Electromagnetic properties of the human body**

Different tissues of the human body are shown to have different electrical characteristics. Most tissue can be considered isotropic, with the exception of muscles and brain tissue which is anisotropic. The cross section of human body cavity in Figure 2.2 shows the possible cluster of the different tissues (lungs) and muscles (heart). To simplify the mathematical model, the human body is assumed to be homogenous and isotropic, where the constitutive parameters such as the conductivity and permittivity are independent of position and direction. Thus, the relationship between the current density, electric field and potential can be described through Maxwell's equations. The body (Ω) is modelled as a closed and bounded subset of three-dimensional space with smooth boundary ($\partial \Omega$) and uniform conductivity (σ). The electric field (\mathbf{E}) enclosed in Ω is expressed in terms of the scalar potential ϕ

$$\mathbf{E} = -\nabla\phi \quad (2.1)$$

The current density (\mathbf{J}) is given by the multiplication of the conductivity and electric field can be computed as:

$$\mathbf{J} = -\sigma\nabla\phi \quad (2.2)$$

Because there are no interior current sources at the frequency of EIT stimulation in the human body the fields can be described in terms of a scalar voltage potential satisfying Kirchoff's voltage law:

$$\nabla \cdot \sigma \nabla \phi = 0 \quad (2.3)$$

The boundary current density (\mathbf{j}), which is the normal of the current density (\mathbf{J}) is expressed as

$$\mathbf{j} = \sigma \nabla \phi \cdot \mathbf{n} \quad (2.4)$$

Based on these relationships the problem of determining the potential inside the body from boundary measurement is carried out through the finite element method.

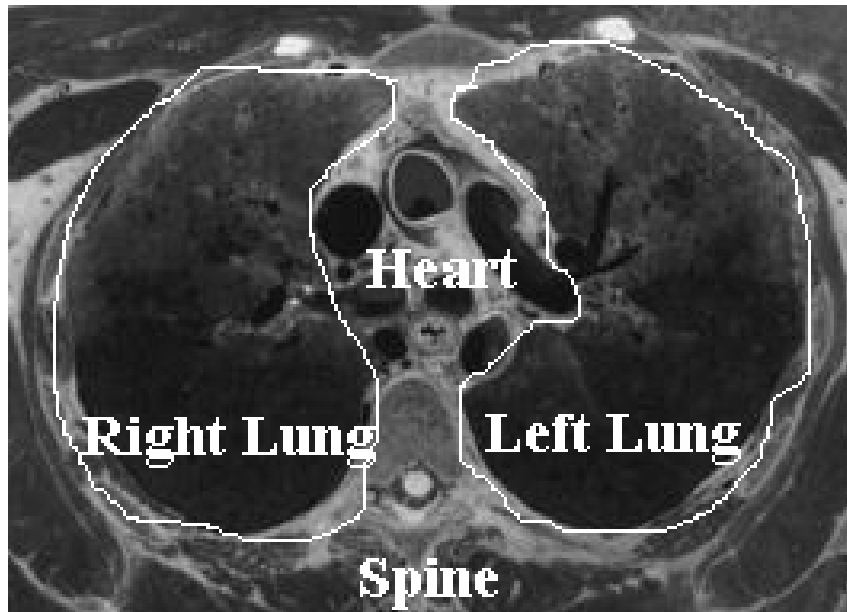


Figure 2.2 Cross Section of the Human body cavity (adapted from *visible human project*: http://www.uchsc.edu/sm/chs/browse/browse_m.html)

2.2.2 Electrode Models

To be able to completely model the human body, it is also necessary to model the interaction of electrodes on the surface. Various methods have been developed (Cheng *et al*, 1989) ranging from the simplest, Point Electrode Model, to the more sophisticated Complete Electrode Model. These methods interact with the finite element model to incorporate the characteristics of the electrode based on the appropriate boundary condition. In the Point Electrode Model the electrode itself is not modeled but the current density is arbitrarily set on all points on the boundary of the body. The model assumes electrodes are perfect conductors ($V|_{\text{electrode}}=u$) and no current flows away from the

electrodes ($\partial u / \partial \mathbf{n} = 0$). The current under on the boundary of the medium is assumed to be:

$$I = \int_{\Omega} \sigma \frac{\partial u}{\partial \mathbf{n}} \quad (2.5)$$

Then, the Newman boundary condition is defined as

$$\sigma \frac{\partial u}{\partial \mathbf{n}} = -\mathbf{J} \cdot \mathbf{n} \quad (2.6)$$

This condition defines conservation of charge on the boundary where the total amount of current injected into the body is equal to the multiple of skin conductivity and skin surface potential (Borsic, 2002). Even though this is a workable model, it does not fully characterize the body/electrode interaction. The Gap Electrode Model improves upon the previous model and considers the discreteness of the electrodes on the body's surface. Consequently, the current density is set to zero on the inter-electrode gap and set to a constant value underneath the electrode.

The assumption that the current density is constant is not accurate considering that it has been shown that electrodes have a higher current density around edges (Tungjitkusolmun, 2000). Moreover, the shunting effect of electrodes where current does not flow inside the body but mostly on the outer edge, is not considered. The Shunt Electrode Model was developed to include the shunting effect of electrodes. This model considers the current density underneath the electrode over the contact surface to be equal to the current injected.

Still, the shunt electrode model does not account for all electrode/body interaction since it does not consider the contact impedance of the electrodes. The Complete Electrode Model incorporates all model characteristics of the shunt electrode model and the contact impedance of the electrodes. The model's ability to better characterize the electrode/body interaction has been proven by Cheng *et al* (1989) through laboratory phantoms.

2.2.3 Forward Model and Finite Element Method

The forward model of EIT is the estimation of the potential in Ω given the current stimuli and the boundary condition described by one of the above electrode models discussed in the previous section. The FEM allows an approximate solution to the EIT forward model by discretizing the domain. The FEM models Ω as a number of discrete, non-overlapping elements connected by nodes. The most common element shape chosen are triangular elements and tetrahedral elements for use in 2D and 3D applications, respectively. The edges of the elements are known as nodes (ϕ_i) representing certain discrete value such as nodal potential values in EIT. The voltage on each element is modeled by basis functions (N_i) for each triangular element i . These are interpolating functions that have a value one at a node and zero on the other nodes, forming a “tent-like” functions, as shown in Figure 2.3. The region of support for each nodal basis function is restricted to be within the elements sharing the common node.

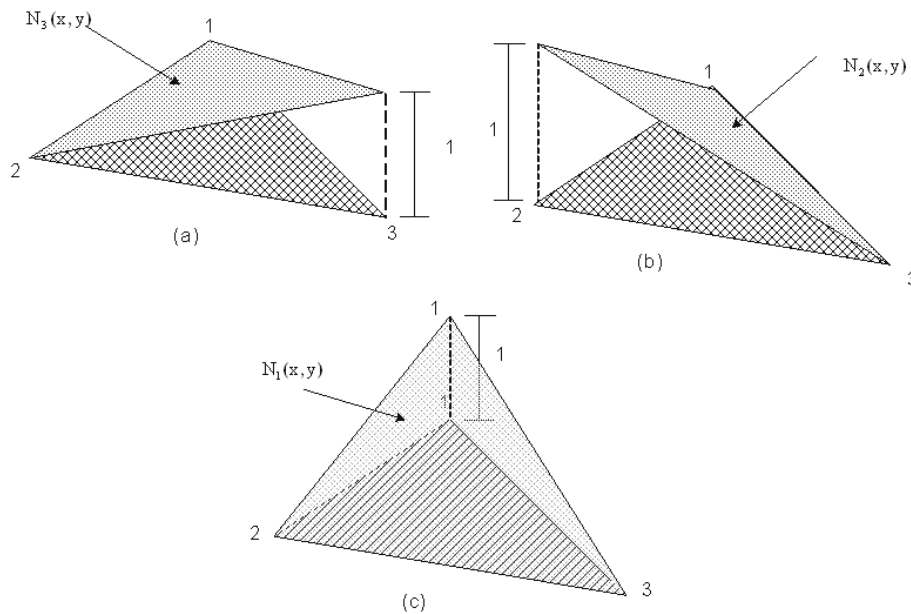


Figure 2.3 Nodal Basis functions over a triangle element

The potential over each element is approximated as

$$\tilde{\phi} = \sum_{i=1}^W \phi_i N_i \quad (2.7)$$

where W is the number of nodes and ϕ_i is nodal potential values. The nodal values ϕ_i are calculated through the weighted residual method (Borsic, 2002) or the Rayleigh-Ritz method (Huebner, 1974). The weighted residual approach estimates the potential distribution that results in the smallest possible residual. Equation (2.3) can be written as:

$$\int_{\Omega_i} (\nabla \cdot \sigma \nabla \tilde{\phi}) w_i = \int_{\Omega_i} r \times w_i = 0 \quad (2.8)$$

Where Ω_i is the region of Ω covered by element i . r is the residual resulting from calculation of equation (2.3). w_i is the weight factor introduced to minimize the residual. The Galerkin Criterion suggests substituting the weight terms with the basis (N_i) for each element.

$$\int_{\Omega_i} (\nabla \cdot \sigma \nabla \tilde{\phi}) N_i = 0 \quad (2.9)$$

The integral of equation (2.9) is carried out over the region (Ω_i). Applying Gauss's Theorem and assembling the matrices resulting from (2.9), the electric potential at each node is expressed in a form of matrix. The unknown potential is solved through the set of linear equations expressed as

$$\mathbf{Y}(\sigma)\mathbf{p} = \mathbf{c} \quad (2.10)$$

where \mathbf{p} is a vector of unknown nodal potentials, voltage electrode potentials, and current electrode potentials. The \mathbf{c} vector is a collection of the injection current values. \mathbf{Y} is the Admittance matrix, which is dependent on the conductivity (σ). The assembly of this matrix is described in detailed by Borsic (2002). The above equation is the formal setup for the forward problem. Equation (2.10) can be solved through such direct method as Cholesky factorization if the matrix size is not exceedingly large. Most reconstruction algorithms (Section 2.4) use a linearized approach, which leads to expression of the forward model as

$$\mathbf{u} = \mathbf{H}\boldsymbol{\sigma} \quad (2.11)$$

where \mathbf{H} is a Jacobian matrix expressed with the voltage electrode potentials and background conductivity. \mathbf{u} is the voltage electrode potentials that are already known from the voltage electrode measurements.

$$\mathbf{H} = \begin{bmatrix} \frac{\partial v_1}{\partial \sigma_1} & \dots & \frac{\partial v_1}{\partial \sigma_m} \\ \vdots & \ddots & \vdots \\ \frac{\partial v_m}{\partial \sigma_1} & \dots & \frac{\partial v_m}{\partial \sigma_m} \end{bmatrix} \quad (2.12)$$

The format of the forward model as in equation (2.11) becomes apparent when we discuss regularized reconstruction algorithms.

2.2.4 Finite Element Method Meshes

In 2D Finite Element Method, triangular elements are often used. Triangular elements are divided such that the regions experiencing high change in conductivity have smaller elements, which results in a much more accurate model. These large changes in conductivity mostly occur on the boundary of the object due to the intensity of the current injected (see Figure 2.4). These same arguments are extended into 3D EIT, where tetrahedral elements are used. The accuracy of the resulting potential values from equation (2.10) depends on the shape of the FEM mesh and the total number of elements available. A mesh with a large number of elements generally provides more accurate potential values. The drawback of having a very fine mesh is the computational time spent to generate the forward solution. Consequently, it becomes necessary that the user select an appropriate element size for each application. For the purpose this thesis, we used meshes with 120, 216 and 256 elements.

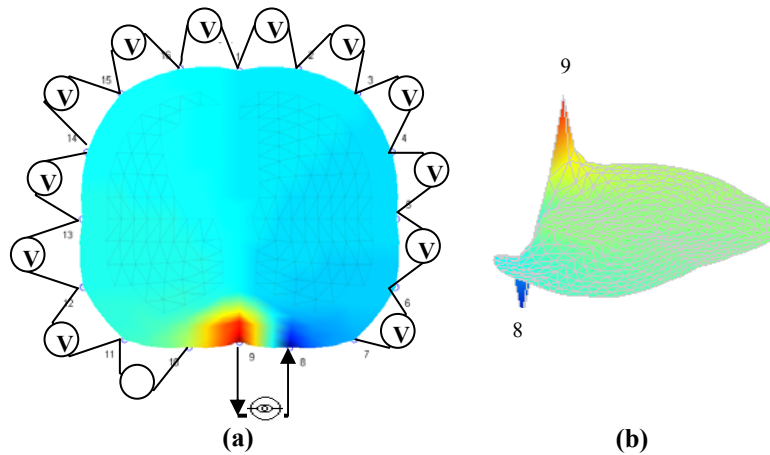


Figure 2.4 Voltage and Current distribution with electrode pair [8 9]: (a) voltage distribution high near the boundary. (b) Current distribution also high close to the injection electrodes.

It is necessary to design a mesh with element geometry that can fit the boundary of the medium appropriately. All real data used in this thesis were from experiments carried out on dogs, which have a thorax shape that is an ellipse with low eccentricity. A circular mesh that closely approximates a canine thorax was used, see Figure 2.5. For human thorax, Borsic (2002) has shown that more accurate results are obtained by using a mesh that accounts for the boundary shape. In addition, varying sizes of triangular elements were used both on the boundary and inside the mesh. Smaller elements are used in regions that are expected to encounter much higher change in conductivity, such as that of the heart area.

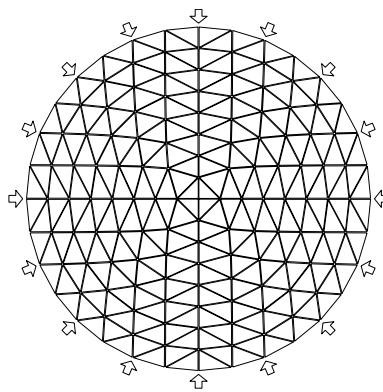


Figure 2.5 Circular mesh for EIT with 256 elements, for a 16 electrode system

2.3 Inverse Theory and Regularization

The previous section discussed the mathematical approach to calculate the potential distribution from the current stimuli and medium geometry. In this section, the ill-posed nature of the EIT problem is established. The concept of inverse theory and the criterion for labelling a problem ill-posed or ill-conditioned is introduced. Finally possible solutions for solving ill-posed and ill-conditioned problems based on regularization are put forth.

2.3.1 Inverse Theory

The generalized form of the measurement process can be expressed as:

$$\mathbf{y} = \mathbf{H}\mathbf{x} + \mathbf{n} \quad (2.13)$$

Where: \mathbf{x} : input signal ($N \times 1$)

\mathbf{y} : output signal ($M \times 1$)

\mathbf{n} : additive noise ($M \times 1$)

\mathbf{H} : system matrix ($M \times N$)

The problem of estimation of unknown input (\mathbf{x}) based on measured output (\mathbf{y}) is common. For example in image restoration, the acquisition of the original image (\mathbf{x}) from the corrupted image (\mathbf{y}) can be calculated given the knowledge of the blurring process (\mathbf{H}). The process is the inverse problem. An inverse problem can be classified as well-posed or ill posed. According to Hadamard (Hansen, 1998) an inverse problem is well-posed if :

1. A solution exists for any data d in the data space
2. A unique solution f exists in the image space
3. The inverse mapping $d \rightarrow f$ is continuous

A problem is ill-posed if one of the above three conditions is not satisfied. Techniques such as model fitting through a least square's estimate (LSE) using singular value decomposition (SVD) were developed with the purpose of finding a solution that closely matches the data (Hansen, 1998). But a unique solution can only be acquired when the

image space is smaller or equal to the data space. Even though the problem of singularities is addressed, the equation is still ill-conditioned when the singular value is small, resulting in a badly reconstructed image.

2.3.2 EIT as ill-posed and ill-conditioned problem

Analyzing the inverse problem of EIT, we can see that the first Hadamard criterion is satisfied since for each voltage measurement data set there is a corresponding conductivity distribution. Lionheart (1997) has shown that the uniqueness only applies to isotropic systems where there are no infinite or zero conductivities. The second criterion of obtaining a unique solution is handled through a reciprocity test, where the data and the resulting conductivity are assumed to match with a certain error bound. The third criterion of continuous inverse mapping of the voltage measurement data set with the resulting conductivity is not satisfied. This is because recovering an unknown conductivity from boundary data causes large changes in the conductivity distribution, which are undetectable by the boundary voltage measurements at a specific precision. The process of finding the proper inverse mapping and unique solution is generally termed as image reconstruction. The two major classes of EIT image reconstruction that successfully solve the ill-posed and ill-conditioned problem of EIT are discussed in section 2.4.

2.3.3 Regularization Techniques

Different mathematical techniques are designed to improve the performance of inverse solutions for ill-conditioned and ill-posed problems. One such solution is constrained Maximum Likelihood (ML) (Hansen, 1998) which relies on the convergence of the solution. ML states: find the input data, x , that gives the most likely output data (y), which is expressed through conditional probability as: $\Pr(y|x)$. The conditional probability expressed using Bayes rule becomes:

$$\Pr(y|x) = \frac{\Pr(x|y)\Pr(y)}{\Pr(x)} = \frac{\Pr(y,x)}{\Pr(x)} \quad (2.14)$$

Where:

$\Pr(y)$: Prior probability of output data y

$\Pr(x)$: Prior probability of input data x

$\Pr(y | x)$: Conditional probability of y given x

$\Pr(x | y)$: Conditional probability of x given y

$\Pr(y, x)$: Joint probability of y and x

A unique solution can be found by maximizing the probability of the output data(y) given input data (x):

$$\tilde{x} = \mathbf{arg\,max}_x \Pr(y | x) \quad (2.15)$$

A number of different iterative algorithms such as Expectation Maximization (EM) and Image Space Restoration Algorithm (ISRA) (Hansen, 1998) are available for solving the equation (2.15). The ML approach for solving inverse problems is based on the assumption that the solution is convergent. In addition, this approach does not incorporate any known information about the input or output data to solve the problem. Incorporating known information into the problem solving allows us to include divergent solutions and improve the chances of acquiring the proper solution. This information is termed as *a priori* and is determined by our belief of what the solution should be. The *a priori* information could be based on state of knowledge of the problem described by subjective probabilities.

Subjective probability is a mathematical framework that is used to represent degree of reasonable belief about a problem (Kreyszig, 1983). Probability densities represent states of knowledge over the space of possibilities and it becomes possible to formulate the general theory of inverse problems as one of statistical inference. This concept allows the prior knowledge to be based on the current state of the problem rather than the overall expectations/assumptions. Bayesian statistics, based on joint and conditional probability, provides a theory of inference that enables us to relate the results of observation with theoretical predictions.

Tikhonov regularization (Hansen, 1998) is one prominent example of regularization with *a priori* information where there is a trade off between the data fitting and certain *a priori* information. For example in image restoration, Tikhonov regularization controls the data

fitting while smoothing the resulting image. Maximum a *posteriori* (MAP) is the approach used for image reconstruction of EIT (section 2.5).

2.4 Image reconstruction in EIT

Image reconstructions are developed for static and difference imaging techniques. Static image reconstruction uses one set of data to carry out the image reconstruction; while difference image reconstruction uses two sets of data and calculates a difference in conductivity.

Static Image Reconstruction: A modified form of the Newton-Raphson algorithm was introduced by Yorkey (1987) to apply for static image reconstruction. This technique assumes a homogenous conductivity and initially uses the FEM to simulate the voltage measurements. The conductivity is subsequently modified to better approximate the voltage measurements in an iterative manner as shown in Figure 2.6. Unfortunately, this type of iterative technique can become unstable if the model geometry is not accurate (Adler, 1996). Many groups have made improvements to this algorithm, but it still suffers from sensitivity to errors (Barber, 1988; Korjenevsky, 1997). The sensitivity is due to errors in positioning electrodes on the surface of the body. Variations in electrode positioning significantly affects the conductivity distribution in center of the object, since EIT is more sensitive to changes on the boundary of the medium than changes within the medium (Korjenevsky, 1997).

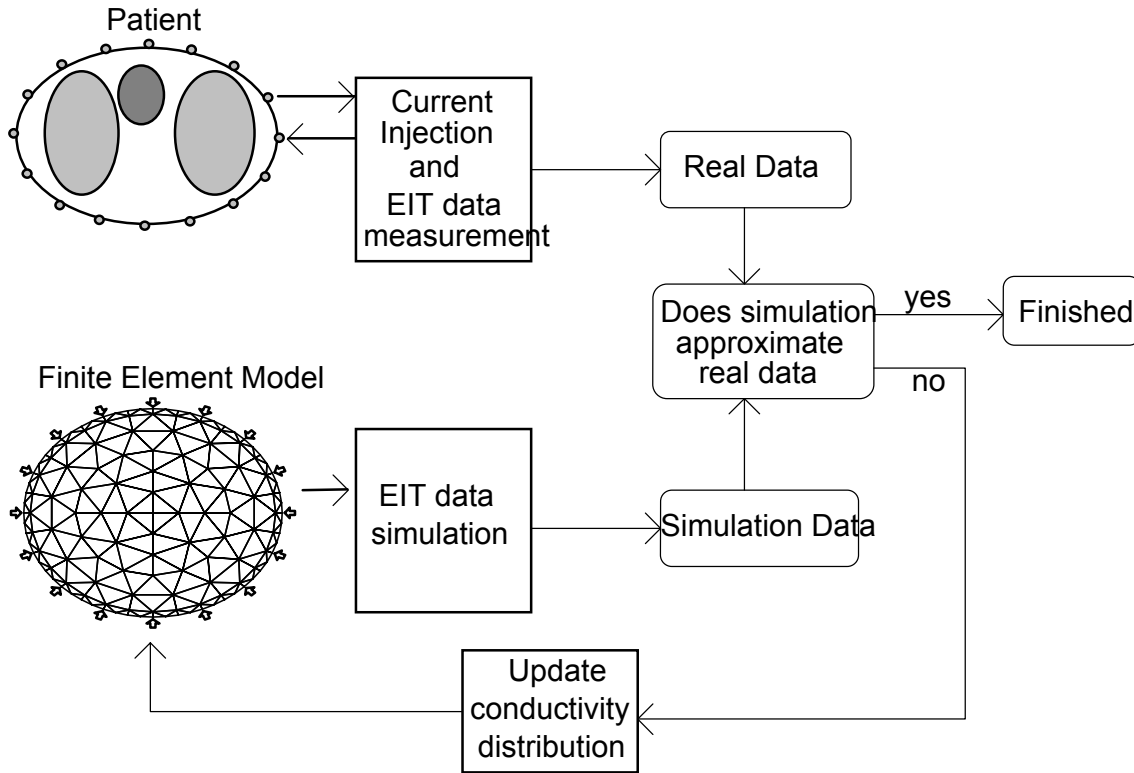


Figure 2.6 Newton Raphson Algorithm (taken from Adler (1995))

Difference Image Reconstruction: This algorithm has the ability to reduce the effect of many of the sources of error by calculating the change in conductivity due to the changes in measurements. Difference EIT allows the forward problem to be a linear function of the conductivity change based on equation (2.11)

$$\Delta \mathbf{u} = \mathbf{H} \Delta \boldsymbol{\sigma} \quad (2.16)$$

Where $\Delta \mathbf{u}$ is the change in voltage measurement and $\Delta \boldsymbol{\sigma}$ is the change in conductivity. \mathbf{H} is the Jacobian or sensitivity matrix describing the linear relationship between $\Delta \boldsymbol{\sigma}$ and $\Delta \mathbf{u}$. Barber (1988) has shown that difference imaging is relatively insensitive to errors in electrode placements as long as these remain constant during the experiment. The linear approximation makes the relationship only valid in a limited range but it is applicable for a wide variety of problems.

Barber (1985) developed the *Equipotential Backprojection* reconstruction algorithm for difference imaging based on backprojection in computed tomography. The potential

measured by a pair of electrode is projected back across equipotential region that is affected by the injection and measurement pair. The above algorithm introduced the problem of streaks across the image of the conductivity. In addition, it was limited to circular geometry and tends to push reconstructed contrasts toward the center of the medium (Adler, 1996).

2.5 MAP based regularized image reconstruction

Several groups have proposed maximum a *posteriori* regularization based difference imaging reconstruction algorithm which incorporates prior information based on the physics and geometry of the problem. This thesis primarily uses the algorithm of Adler (1996), which is described next. An image reconstruction approach was developed based on FEM of the forward problem with a MAP formulation of the image reconstruction. The FEM allows a modelling of an arbitrary geometry, and the MAP formulation states the problem in terms of probabilistic assertions about the original conductivity distribution, measurement system, and measurement noise. This allows a natural interpretation of known system information in terms of the model parameters. For instance, a defective measurement channel indicates a high probability of error on data acquired from that channel.

The linearized forward model based on the image (\mathbf{x}) and noise (\mathbf{n}) is given in equation (2.17)

$$\mathbf{z} = \mathbf{H}\mathbf{x} + \mathbf{n} \quad (2.17)$$

The difference in measurements, \mathbf{z} , is defined for the time interval (t^1, t^2) as

$$\mathbf{z} = \frac{\mathbf{v}_i^1 - \mathbf{v}_i^2}{\frac{1}{2}(\mathbf{v}_i^1 + \mathbf{v}_i^2)} \quad (2.18)$$

where \mathbf{v}_i^1 and \mathbf{v}_i^2 represent the i^{th} voltage measurements at time t^1 and t^2 , respectively.

The change in conductivity (\mathbf{x}) needs to be expressed such that it represents largest possible range. Even though zero and infinite conductivity represent opposite effects of

the voltage; they are not numerically equidistant from the background conductivity. Hence, a parameterization using the log conductivity was introduced

$$\mathbf{x} = \log(\sigma^1) - \log(\sigma^2) \quad (2.19)$$

where σ^1 and σ^2 represent the conductivity at time t^1 and t^2 , respectively.

The MAP approach to image reconstruction defines the solution as the most likely estimate $\hat{\mathbf{x}}$ given the measured signal \mathbf{z} and certain statistical information about the medium. This approach was chosen because it allows an elegant interpretation of the image reconstruction algorithm in terms of the statistical properties of the experimental situation. To simplify the computations, these statistical properties are modelled as Gaussian distribution (mean \mathbf{x}_∞ and co-variance \mathbf{R}_x). Based on this model, the distribution function of the image, $f(\mathbf{x})$, is expressed as

$$f(\mathbf{x}) = \frac{1}{(2\pi)^{N/2} \sqrt{|\mathbf{R}_x|}} e^{-\frac{1}{2}(\mathbf{x} - \mathbf{x}_\infty)^T \mathbf{R}_x^{-1} (\mathbf{x} - \mathbf{x}_\infty)} \quad (2.20)$$

The *a posteriori* distribution function of \mathbf{z} given a conductivity distribution \mathbf{x} is derived from the definition of the problem (2.17).

$$f(\mathbf{z} | \mathbf{x}) = \frac{1}{(2\pi)^{M/2} \sqrt{|\mathbf{R}_n|}} e^{-\frac{1}{2}(\mathbf{z} - \mathbf{Hx})^T \mathbf{R}_n^{-1} (\mathbf{z} - \mathbf{Hx})} \quad (2.21)$$

The noise covariance, \mathbf{R}_n , which measures the noise power in each component of the signal is expressed as

$$\mathbf{R}_n = \mathbf{E}[\mathbf{nn}^t] = \begin{bmatrix} \sigma_1^2 & 0 & \cdots & 0 \\ 0 & \sigma_2^2 & \cdots & 0 \\ \vdots & \vdots & \ddots & \vdots \\ 0 & 0 & \cdots & \sigma_M^2 \end{bmatrix} \quad (2.22)$$

The MAP algorithm estimates $\hat{\mathbf{x}}$ by finding the most likely image for the measurement \mathbf{z} . Accordingly, Bayes' rule is applied to equation (2.21)

$$f(\mathbf{x} | \mathbf{z}) = \frac{f(\mathbf{z} | \mathbf{x})f(\mathbf{x})}{f(\mathbf{z})} \quad (2.23)$$

Which when substituting the individual probability density functions becomes

$$f(\mathbf{x} | \mathbf{z}) = \frac{e^{-\frac{1}{2}[(\mathbf{z} - \mathbf{H}\mathbf{x})^T \mathbf{R}_n^{-1}(\mathbf{z} - \mathbf{H}\mathbf{x}) + (\mathbf{x} - \mathbf{x}_\infty)^T \mathbf{R}_x^{-1}(\mathbf{x} - \mathbf{x}_\infty)]}}{(2\pi)^{(M+N)/2} \sqrt{|\mathbf{R}_x| |\mathbf{R}_n|}} f(\mathbf{z}) \quad (2.24)$$

The MAP solution is chosen as the most likely image, \mathbf{x} , given measurements, \mathbf{z} . This value of \mathbf{x} will maximize $f(\mathbf{x} | \mathbf{z})$. Equation (2.24) is maximized when the exponent in the numerator is minimised

$$\hat{\mathbf{x}} = \underset{\mathbf{x}}{\arg \min} \left[(\mathbf{z} - \mathbf{H}\mathbf{x})^T \mathbf{R}_n^{-1}(\mathbf{z} - \mathbf{H}\mathbf{x}) + (\mathbf{x} - \mathbf{x}_\infty)^T \mathbf{R}_x^{-1}(\mathbf{x} - \mathbf{x}_\infty) \right] \quad (2.25)$$

The estimate can be simplified as

$$\hat{\mathbf{x}} = \left(\mathbf{H}^T \mathbf{R}_n^{-1} \mathbf{H} + \mathbf{R}_x^{-1} \right)^{-1} \left(\mathbf{H}^T \mathbf{R}_n^{-1} \mathbf{z} + \mathbf{R}_x^{-1} \mathbf{x}_\infty \right) \quad (2.26)$$

In the situation when the noise variance is constant across all measurement channels $\mathbf{R}_n^{-1} = \sigma_n^2 \mathbf{W}$. In addition, the expectation of image (\mathbf{x}_∞) is best modeled as zero, since the conductivity change can be equally conductive or non-conductive. \mathbf{R}_x represents the amplitude of the image and the spatial frequency distribution. The lack of high frequency content in EIT images results in high correlation of conductivities elements close to each other. Adler (1996) assumed that pixels that are closer to one another are highly correlated; while pixels that are further apart are uncorrelated. This assumption allows us to regard \mathbf{R}_x as a low-pass filter, but the inversion of this matrix is not always possible due to singularity. As a consequence, a new regularization matrix \mathbf{Q} is reconstructed using the high pass filter characteristic of \mathbf{R}_x^{-1} . A filtering matrix \mathbf{F} is determined from the assumption of Gaussian high-pass filter characteristics. The regularization matrix \mathbf{Q} is expressed as

$$\mathbf{Q} = \sigma_x^2 \mathbf{F}^t \mathbf{F} \quad (2.27)$$

Substituting (2.27) into (2.26), the regularized inverse can be expressed as

$$\begin{aligned}\hat{\mathbf{x}} &= \left(\mathbf{H}^t \mathbf{W} \mathbf{H} + \frac{\sigma_x^2}{\sigma_n^2} \mathbf{Q} \right)^{-1} (\mathbf{H}^t \mathbf{W} \mathbf{z}) \\ &= (\mathbf{H}^t \mathbf{W} \mathbf{H} + \mu \mathbf{Q})^{-1} (\mathbf{H}^t \mathbf{W} \mathbf{z}) = \mathbf{B}(\mu) \mathbf{z}\end{aligned}\tag{2.28}$$

Where μ is the hyper-parameter value that controls the amount of regularization or the high-pass filter (\mathbf{Q}) introduces into the solution. Too much regularization comes at the expense of the amount of detail (resolution) we can retrieve from a given image. The matrix \mathbf{B} is the reconstruction matrix calculated for a specific hyper-parameter. The criteria used to select the hyper-parameter vary from the size of the FEM element to the regularization matrices. Adler (1996) incorporated these criteria by choosing to control noise amplification. The noise figure (NF), the ratio of the output to input SNR, is chosen from knowledge of the signal and noise level present, and the hyper-parameter is determined based on the appropriate NF.

An example of a reconstructed image using the above MAP regularization approach is shown in Figure 1.1. The figure shows a cross section of a human thorax with certain amount of ventilation in both lungs.

Chapter 3

Characterization of Electrodes

The previous chapter introduced the mathematical principles based on the most common approach used to solve forward and inverse problem. This chapter focuses on the study of error and noise in applications that use electrodes, and approaches used to compensate for the errors. We also explore image reconstruction techniques used for compensation of EIT errors. The research in electrode errors and noise in EEG, ECG, EMG and particularly EIT is discussed.

3.1 Classification of Electrodes

Electrodes are metal contacts on a lead through which the electricity travels. The electrode material has different levels of conductivity and thus has an effect on the transfer of electrical charge. The two major types of electrodes for biomedical applications are needle and surface electrode. Since the goal is to analyze electrodes for EIT, which is a non-invasive imaging application, the more invasive needle electrode is not discussed.

Surface electrodes are classified by size, shape, lead, gel type, and reusability (Ksienski, 1992, Luo *et al*, 1992, Kun and Peura, 1995). In addition to the above characteristics, performance of the electrode depends on the skin-electrode impedance determined by the contact area and conductivity of the surface as shown in Figure 3.1. High electrode, skin and tissue conductivity leads to a low skin-electrode impedance and better transfer of electrical charge. In most applications, the resistivity as the current flows out radially from the center pin is considered, and the voltage drop due to thickness is considered zero (Waugaman and Schrader, 1994). The skin-electrode impedance interaction is modelled

by a simple resistive circuit where the electrode and the tissue are considered purely resistive and the skin is an RC circuit, see Figure 3.2.

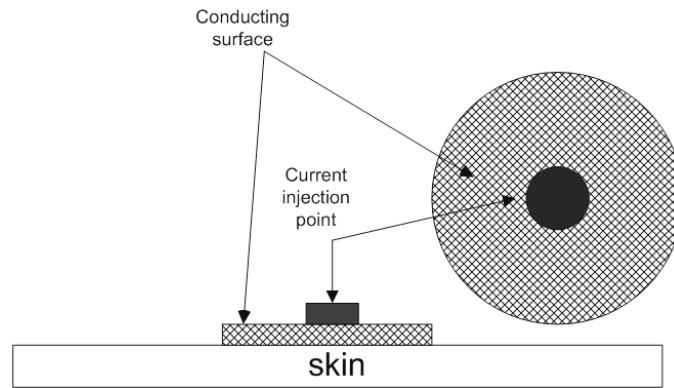


Figure 3.1 Common surface electrode

The type of electrode used must reflect the needs of the application. For example the operating peak to peak voltage of the electrode to be used should be matched with the operating voltage of the device. Furthermore, electrodes used to inject current must provide a uniform current density distribution to allow a more accurate analysis such as voltage measurement in the case of EIT. The different physical characteristics of electrodes and their impact on the conductivity and current density distribution of the electrode are analyzed below.

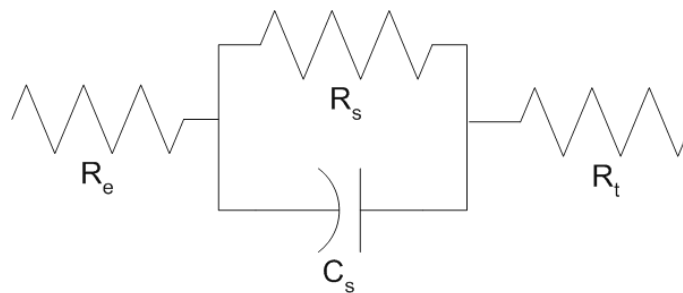


Figure 3.2 Electrode-skin impedance equivalent circuit

Electrode and Gel: The choice of electrode and gel affects the conductivity and current density distribution of the electrode. For instance, platinum iridium electrodes have a higher conductivity (lower resistance) than nickel alloy electrodes (Luo *et al*, 1992). ECG electrodes are pre-gelled with Ag/AgCl to lessen the impact of the skin-electrode impedance that interferes with the actual electrical signal (Seitsonen *et al*, 2000). Patriciu

et al (2001) conducted investigations of the current densities produced by the gel-type surface electrodes. The current density distribution was computed using the finite element model with a tissue like gel slab. The result shows that the gel-type electrode has a non-uniform current density distribution, which can cause electrical skin burns and blood coagulation in gel-type surface electrode. In EIT, the risk of getting skin burns or blood coagulation is minimal due to the low current level (<1mA).

Shape: The current density distribution depends not only on the type of electrode or gel used but also on the shape of the electrode. Tungjitkusolmun *et al* (2000) conducted a study on electrodes for Radio-Frequency Cardiac Ablation where RF current is delivered through the tip of the electrode. The non-uniform distribution of the current density is demonstrated by the increase of the current density distribution on the edge (conductor/insulator boundary) of a circular gel-type electrode exposing the subjects to risk of skin burns. A more uniform current density distribution is achieved by recessing the edge and coating the electrode with a resistive material.

Size: The study of the impact of the size of the electrode was carried out on gel-type electrode and garment type electrode by Patterson and Lockwood (1993). They looked at five different size electrodes to study the impact on the current required to obtain 25% of the Maximal Voluntary Contraction (MVC) of the quadriceps. The total current required for the MVC differed from one subject to another, but for each subject the MVC was not significantly different from one size to another. The two smaller electrodes registered a higher pain rating, which has high correlation to the current density in all subjects. The current density in the skin decreased from 2.7 to 1mA/cm² as the size of the electrode increased from 20 to 60 cm². It is likely that the higher pain rating is due to the increase of the current density over the edges as the distribution is not uniform. The findings conclude that size does not affect the electrical efficiency but does impact the uniformity of the current density distribution.

Reusability: Patterson and Lockwood (1993) observed that the gel-type electrodes are best suited for short term use because they are low cost and do not require any special

fitting. The use of a garment electrode, a conductive cloth type material made into a pocket and filled with electrode gel, is suggested as optimal solution for long term monitoring due to the ease for rapid application and consistency of results over a long period in their research laboratory.

The above properties demonstrate that the electrodes generally do not have uniform current density. Knowledge of the accurate current density of the medium allows a proper modelling of the potential distribution based on the FEM or Boundary Element Method (BEM). Oostendorp and Oosterom (1991) used FEM and BEM, respectively, to estimate the potential distribution of the torso from current density of electrodes for cardiac defibrillation. The different electrode models of skin-impedance interaction and the type of boundary condition applied gave varied results. The results demonstrate that with careful selection of the proper electrode and the right modeling approach the impact of the non-uniformity of the current density can be minimal.

Apart from the above “software solution” for minimizing skin-electrode impedance, Hua *et al* (1993) developed a special electrode known as compound electrode to decrease skin-electrode impedance using a large outer electrode to inject current and small inner electrode to measure voltage. The smaller voltage-measuring electrode allows for a drop in voltage due to reduction of contact impedance. Their results show that the compound electrodes result in reconstructed images that are less sensitive to contact impedance value. Thus, proper selection of electrodes along with the appropriate reconstruction model for EIT can lead to a better imaging system that is less sensitive to measurement errors.

3.2 Sources of error in applications using electrodes

Apart from errors introduced by the physical characteristics of electrodes, there are external causes for error. Electrodes have been used as part of a measurement device in numerous medical applications that precede EIT. Electrocardiogram (ECG), Electroencephalogram (EEG) and Electromyography (EMG) are effective and widely used monitoring techniques. The vulnerability to noise for each device is dependent on

the signal of interest, interference from other electronic devices and the type of electrode used. A concise description of the techniques, their intended use, and their signals of interest are discussed below.

3.2.1 Electrocardiogram

The ECG is a non-invasive test that records the electrical activity of the heart, and is used to determine the heart's rate and rhythm. Depending on the specific test electrodes are placed on the chest, arms or legs. The operating frequency of ECG signals ranges from 0.5 to 200 Hz (Gholam-Hosseini *et al*, 1998). The strength of the signal is much higher on electrodes closer to the heart; hence these electrodes are not significantly affected by noise. Conversely, electrodes at the extremities of the body are highly likely to be impacted by noise. Major sources of noise in ECG are from muscle and electrode problems (Gritzali *et al*, 1988).

A variety of techniques have been developed to estimate and remove the noise in an ECG signal (Gritzali *et al*, 1988; Gholam-Hosseini *et al*, 1998; Ramos and Pallas-Areny, 1996; Perz and Kufner, 1995). The methods range from an adaptive signal approach to remove signals from muscles to a simple band pass filter to remove signals above and below 0.5-170 Hz.

3.2.2 Electroencephalogram

The EEG records brainwave patterns from the continuous electrical signals coming from the brain. The strength of the measured signal ranges from 20 to 100 mV peak to peak over 0-100 Hz (Wright and Kydd, 1992). The operating frequency makes this technique susceptible to TV, radio, power line and other common equipment which operates over the same frequency. In addition, the skull of the subject is a poor conductor and interferes with the transmission of electrical charge from the brain to the skin. The signal strength is also affected by the alignment of the brain cells, which if not aligned properly may cancel one another (Montreal Neurological Institute, 1998). This method is mostly used to diagnose neurological diseases, such as seizures indicated by extreme synchronicity of the neurons generating electrical charge. The electrodes are placed in numerous places of

interest on the scalp after cleaning the particular regions (see Figure 3.3). A special gel or paste helps the electrodes pick up the brain waves more efficiently.

However, the estimation of the brain's activity pattern is shown to be a complicated mathematical problem which requires knowledge of the electrode locations (Khosla *et al*, 1999). As a consequence, the mis-location of scalp electrode leads to estimation errors of the current patterns. The results of Khosla *et al* (1999) and Wang and Gotman (2001) demonstrate that the errors introduced by mis-location, based on realistic head models, are insignificant compared to errors introduced by noise.

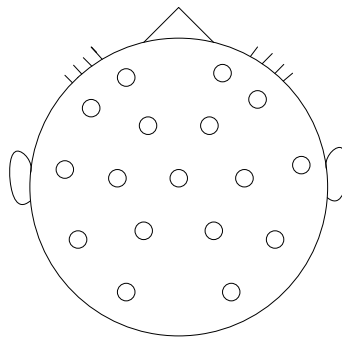


Figure 3.3 Electrode placement on the scalp for EEG measurement

Ollikainen *et al* (2000) investigated the trend of increasing the total number of electrodes on the scalp to improve the spatial resolution of the voltage distributions. They also studied the effects of the electrode size and the contact impedance on the voltage distribution through simulations. The studies led them to conclude that increasing the number of electrodes does not improve the estimate of the voltage distribution due to the shunting effect of electrodes. The optimal number of electrodes vary depending on the electrode size and contact impedance of the electrode. Based on discussion of electrode size and contact impedance, we can deduce that the increase in size and contact impedance heightens the shunting effect.

There are a number of different approaches for the removal and reduction of noise in EEG signals. Methods based on reconstruction theory of phase space for noise removal and reductions in epileptic EEG were developed by Ouyang *et al* (2001). Herrera *et al*

(2000) studied cause and removal of a single event non-white noise from EEG signals based on the wavelet transformation with soft thresholding.

Paloniqpan *et al* (2002) published an interesting approach regarding noise removal in evoked potential signals. Evoked potential signal is generated by the nervous system due to external stimulus. The stimuli used for the study were electrical signals generated by EEG electrodes on the scalp. Consequently, the EEG signals are considered to be noise and are to be removed. The proposed approach uses a two level Principal Component Analysis (PCA) to remove noise and EEG signal from single trial evoked potential signal.

3.2.3 Electromyography

Electromyography is the study of the muscle function through muscle electrical signals. The strength of the signal measured ranges from 0-10mV peak to peak over 50-150 Hz frequency. The operating frequency makes this technique susceptible to TV, radio, power line and other household equipment. The signal strength and its operating frequency vary from surface muscle to deep muscle. For this particular reason, most of the devices use needle electrodes for measurement of deep muscle and standard electrodes on dry shaved skin to reduce the contact impedance.

The causes for noise in EMG range from movement artefact to ECG signal interference. A movement artefact as a result of electrode displacement causes errors in EMG signal in a form of a spike (Ortolan *et al*, 2003). The non-stationary nature of the ECG signal makes the separation complex (Yacoub *et al*, 1994). To improve the signal quality the use of multi-electrode EMG is suggested by Yacoub *et al* (1994). One approach for removal of random electrode noise uses Orthogonal Projection Theory. Adaptive signal processing have been used to remove the ECG signal, and wavelet transformation or non-adaptive digital filtering techniques have been used to remove noise caused by power line interference (Ortolan *et al*, 2003).

3.3 Measurement errors and noise in EIT

Noise and measurement errors in EIT can be due to a number of different factors but the major causes for noise are detached or erroneous electrodes, and electronic interference (Al-Hatib, 1998; Meeson *et al*, 1996; Blott *et al*, 1998; Lozano *et al*, 1995). These noise sources cause imprecise measurements. However, noise sources are not the only causes for imprecise measurements. A number of systematic problems also affect the precision of the measurement acquired by the EIT system. We consider factors such as number of electrodes, number of FEM elements and electrode models as caused for limitation of measurement precision.

3.3.1 Electronic interference

The major devices using electrodes, discussed in section 3.2, were affected by a number of different types of electronic interference due to the low operating frequency. Most EIT systems operate at a much higher frequency (9kHz-1.2MHz) making them less sensitive to this type of electronic interference such as power line. But, sensitivity still exists for all devices that operate in EIT operating frequency. Meeson *et al* (1996) noted a higher level of electrical noise in the clinical environment compared to the laboratory environment. They characterized the system noise based on a four electrode system and a figure of merit for testing EIT systems was created. The figure of merit allows for adjustment of the EIT equipment before data acquisition.

3.3.2 Hardware

Faulty hardware can be the cause for measurement errors or added noise. For example, in the Sheffield APT system, instrumentation amplifiers connected directly to the electrodes are the main contributor of added noise to the measured data (Sansen *et al*, 1992). The voltage driven MICAS EIT System uses a switch matrix along with an amplifier to minimize the impact of cross talk (Sansen *et al*, 1992). But the errors from the switch matrix due to aging of the unit or causing faulty connections are a possibility. Furthermore, Sansen *et al* (1992) states that in a current driven EIT system, systematic errors are introduced due to “parasitic capacitance”. In a single current source, the parasitic capacitances involved in multiplexing cause phase and crosstalk problems,

while in multiple current source systems, the matching of the sources is important (Williams *et al*, 1992). If the above conditions are not accounted for the quality of the image is degraded due to voltage noise (Williams *et al*, 1992). Noise in the current driver has a multiplicative effect in the measured voltage since this noise propagates through the imaged impedance distribution. Noise in the voltage detector electronics will have a signal-independent additive contribution (Frangi *et al*, 2002).

Major faults with the unit could prevent the equipment from functioning. However, smaller errors are eliminated in difference imaging due to the use of the differential voltage. The impact of systematic error common to individual measurement channels is more prevalent in static imaging due to the lack of a reference data set.

3.3.3 Detached and misplaced electrodes

Measurement error due to detached or misplaced electrodes is a major issue in long term monitor using EIT (Lozano *et al*, 1994). Even though every effort is made to place and attach the electrodes properly, an electrode may detach or become poorly connected. The cause is mainly due to aging for the electrode contact and gel, patient movement, sweat or peripheral edema (Lozano *et al*, 1994). Lozano *et al* (1994) showed that measured impedance changes up to 3.6% when one electrode is replaced, and 4.4% when all electrodes are replaced.

The effects of incorrect electrode localization were also studied by Barber and Brown (1988). They used adjacent current patterns and the equipotential backprojection algorithm in the simulations. After randomly misplacing electrodes and collecting the measurement data set, they found that the reconstruction of absolute images is very sensitive to errors in electrode placement. When they simulated these effects on difference imaging, i.e. computed a reference data set with the same misplaced electrode positions as the measurement set, the reconstructed image was almost as good as the one reconstructed from non-error contaminated data sets.

This result demonstrated that difference imaging is quite insensitive to errors in electrode localization. The effects of FEM errors in the electrode localization were also studied by Hu *et al* (1987). They found that the modeling errors in the electrode localization are a much more important source of measurement errors than the electronics of the measurement system and suggested that the precise layout of the electrodes be determined.

3.3.4 Electrode placement patterns and number

Different placement patterns are available to conduct EIT measurements. Booth and Basarab-Horwath (1996) compared three different placement patterns over circular and square phantoms using back-projection reconstruction method with the adjacent measurement pattern. A peripheral placement of electrodes over the circular and square phantom and a distributed placement pattern over square phantom were studied. Their results show that the distributed placement of electrodes produced images that are better able to resolve anomalies at the center of the phantoms than peripheral placement. In addition, distributed placement provides more independent measurements as well as proper spatial distribution. However, we have found no literature to measure the validity of this result in clinical application. A reference is made by Booth and Basarab-Horwath (1996) that the distributed placement is used for EIT imaging for mining.

In addition, the total number of electrodes used affects the accuracy of the measurement. The accuracy improvement is dependent on the number of electrodes combined with the electrode model, the skin-electrode impedance and the size of the electrodes. When the number of electrodes increases, the shunting between electrodes is much greater and the current diffusion into the medium is reduced. Hua *et al* (1993) noted that inter-electrode gap and mismatch of electrodes affect results at high spatial frequency current (>50 KHz) but found it difficult to measure and specify the impact on the FEM model. Thus, it is necessary to conduct a test to determine the optimal number of electrodes and inter-electrode gap based on the type, size, electrode model, spatial current frequency and skin-electrode impedance.

3.3.5 FEM mesh elements and electrode models

In section 2.2.2, we introduced electrode models used for solving the forward problem. Measurement error is reduced when a more accurate model such as complete electrode model is used. Hua *et al* (1993) demonstrated that a FEM model using the complete electrode model does account for shunting and edge effect of the current density distribution. Better matching results were obtained for simple FEM models at low spatial frequency than at high spatial frequency. This is due to the uniformity of current density at low spatial frequency. Overall, the results were improved by using a finer FEM mesh for both boundary and internal FEM elements. According to Hua *et al* (1993), errors in modelling of an electrode are due to the error in determining the contact impedance and results in noise throughout the image. Thus, modelling of the contact impedance within the FEM model helps improve the result of the reconstruction algorithm and reduce the measurement error. They also discovered that high spatial frequency current results in measured voltage with low signal to noise ratio (SNR) introducing error in measured values.

3.3.6 Non-Stationary noise and EIT

This section considers modelling EIT measurement noise. Given a modified generalized signal representation of equation (2.13) that is time dependent

$$y(t)=Hx(t)+a*n(t) \quad (3.1)$$

Where a is the amplitude of the noise signal. Noise classified as stationary does not change its statistical properties over time. Hence, the observation of the noise at interval (t_0, t_1) is the same as observation at $(t_0+\theta, t_1+\theta)$. The parameters of the noise such as mean, variance, and amplitude are independent of time. Hence, Gaussian noise with constant mean and variance and Poisson noise that has the same photons per pixel exposure regardless of time are example of stationary noise.

A non-stationary noise has statistical properties which vary over time. Examples of such noise occur in images, where non-stationary noise occurs due to intermittent interference

by electronic components, see Figure 3.4. In ECG signals, it can be due to electrode error (see Figure 3.5) and in audio and speech due to change in background noise.

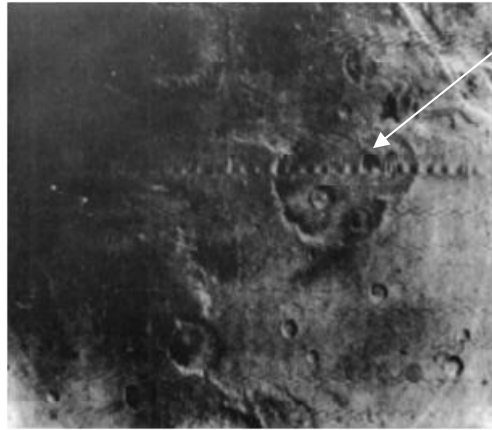


Figure 3.4 Example of non-stationary noise in images. Arrow indicates area of the image affected by non-stationary noise represented by a line across the image

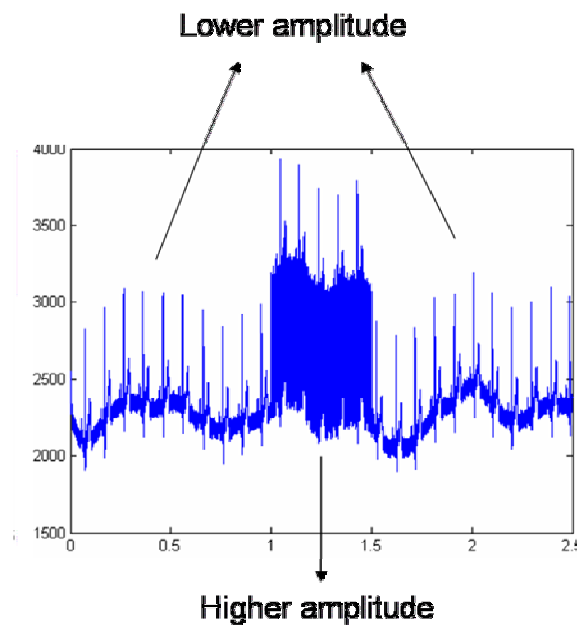


Figure 3.5 Example of non-stationary signal in ECG varying over time. Notice the High amplitude portion of the ECG signal is affected by noise that is time dependent.

In the previous sections, we have demonstrated that noise in EIT is dependent on various factors such as skin movement, sweat, and electronic drift. All these factors are shown to differ in time, changing the characteristics of the noise in EIT. This suggests that noise in EIT has a non-stationary characteristic.

However, the compensation/restoration techniques do not depend on the different difference image but on fixed voltage difference data measured within time difference Δt . The compensation and restoration technique are explored in section 3.4.

3.4 Electrode error compensation in EIT

We have seen the various causes for noise and measurement error in EIT. These problems are usually dealt with by prevention or recovery. The prevention approach deals with the reduction of systematic errors where a level of predictability exists. Thus, measurement errors due to electrode type, inter-electrode gap, positional variation, skin-electrode impedance and hardware can be corrected through a preventive approach. On the other hand, errors due to electrode movement or detachment can be compensated via methods based on recovery approach.

3.4.1 Compensation for positional variation of electrodes

Compensation for positional variation of electrodes in EIT was introduced by Blott *et al* (1998). They propose two approaches: image reconstruction algorithm with reduced sensitivity to electrode position and modifying the sensitivity matrix during measurement. The first approach allows images reconstructed from the voltages for two slightly different electrode configurations to be as similar as possible. Hence image from voltage difference measurement \mathbf{z}_1 and voltage difference measurement \mathbf{z}_2 of a second electrode position should be close to zero. Blott *et al.* note that if the predicted voltage difference measurement is equal to the observed voltage difference measurement the product of the sensitivity matrix (\mathbf{H}) and the reconstruction matrix (\mathbf{B}) should equal \mathbf{I} , the identity matrix. Ideally, the difference of the multiple \mathbf{BH} before and after electrode repositioning should equal to zero:

$$\mathbf{BH}_1 - \mathbf{BH}_2 = \mathbf{B}\delta\mathbf{H}^{(r)} = 0 \quad (3.2)$$

$\delta\mathbf{H}^{(r)}$ is the change in \mathbf{H} when electrode r is moved by a small distance. The reconstruction matrices are also sensitive to electrode misplacement and reduced sensitivity can only be achieved at the expense of data mismatch. Blott *et al.* adapted a weighted approach to allow certain parts of the image, such as the lung area, more variation. The resulting image is much smoother with magnitude and artefact reduced.

The second approach compensates for small movements in the electrode positions by using a modified sensitivity matrix. A regularized reconstruction algorithm that minimizes the mean square value of the change in resistivity with a constraint to the data fit. The sensitivity matrix is recalculated based on initial \mathbf{H}_0 and the change in the sensitivity matrix \mathbf{H}_0 for electrode r $\delta\mathbf{H}^{(r)}$.

$$\mathbf{H} = \mathbf{H}_0 + \sum_r \varepsilon_r \delta\mathbf{H}^{(r)} \quad (3.3)$$

ε_r is the fraction of $\delta\mathbf{H}^{(r)}$ needed to model a small electrode displacement. They propose an iterative solution to solve for the values of ε_r . The sensitivity estimation is repeated until the relative change in mean square value of the change in resistivity is less than 1%. The major advantage of the second approach is the ability to control noise in the images by selection of basis images that are least sensitive to electrode positions.

3.4.2 Image reconstruction with missing data

Errors due to detached, loosely connected, or misplaced electrodes cannot be handled in a preventive manner. In clinical situations, it may be a tedious task to monitor and correct these errors. In the absence of a method for recovery of data, experiments need to be repeated. For EIT applications used to monitor patients, repeating the experiments is impossible and recovery method is necessary. Adler (2004) introduced two methods to compensate for missing data based on image reconstruction with missing data. The methods perform image reconstruction after removal of data from the erroneous electrode.

The first method removes affected measurements by zeroing all values in the reconstruction matrix (\mathbf{B}). However, the removal of the affected data can introduce artefacts into the reconstructed images. The second method deals with erroneous data by introducing a weight factor, based on the variance of measured data, into the regularization scheme. The affected measurement is weighted by its variance, where

infinite noise is considered to have infinite variance and zero weight. Thus, \mathbf{W} of equation (2.28) is modified as follows:

$$\text{Set } \mathbf{W}_{i,i} = \frac{\mathbf{W}_{i,i}}{\sigma_n^2}, \forall \text{ affected measurements } i \quad (3.4)$$

This method clearly demonstrates the possibility of recovering the result from corrupted data. Hence, it is important that there should be a detection method that can work under different measurement patterns, and different number of electrodes. The next chapter introduces one such detection method.

Chapter 4

Electrode Error detection

Various heuristic techniques have been used to detect the presence of erroneous electrodes. For example, a test for the presence of faulty electrodes could be based on analysis of images for artefacts, or a test of the measured voltages for unusually large changes. The disadvantage of such heuristic approaches is the difficulty in defining an image artefact, in relation to an unusual, but accurate, measurement. Specifically, it is difficult to define a threshold for changes that could be applied across different systems and injection patterns.

In order to systematically detect such erroneous electrodes, we propose a method based on comparing the measurements obtained on all electrodes to each other. Since all electrodes measure the same medium, it is reasonable to expect that “good” electrodes will produce measurements consistent with each other. The consistency of a set of electrodes can be verified by estimating the measured data at each electrode in the set, and then comparing the estimate to the actual data measured. A set of electrodes with consistent measurements must contain all “good” electrodes. In order to test an N electrode EIT system, we test all possible sets of $N-1$ electrodes; if only one of the subsets contains all “good” electrodes, then the electrode excluded from that set must be erroneous.

4.1 Heuristic detection

An attempt was made to approach the erroneous electrode detection heuristically. The idea stems from the concept that erroneous electrodes exhibit large changes in measurement data. Based on the drive pattern and threshold, it is possible to tally the total number occurrences of electrodes that result in above threshold measurement. The electrode that has the largest number of occurrence is expected to be the erroneous electrode. Even though the idea is straightforward, the difficulty is in finding a reliable way to select the threshold for a particular data set. One way of selecting a threshold is by developing a measure for “good data”. The data set considered to be good can be acquired at the calibration stage of EIT for each measurement session. The average value of the measurement from the good data can then be considered as the threshold.

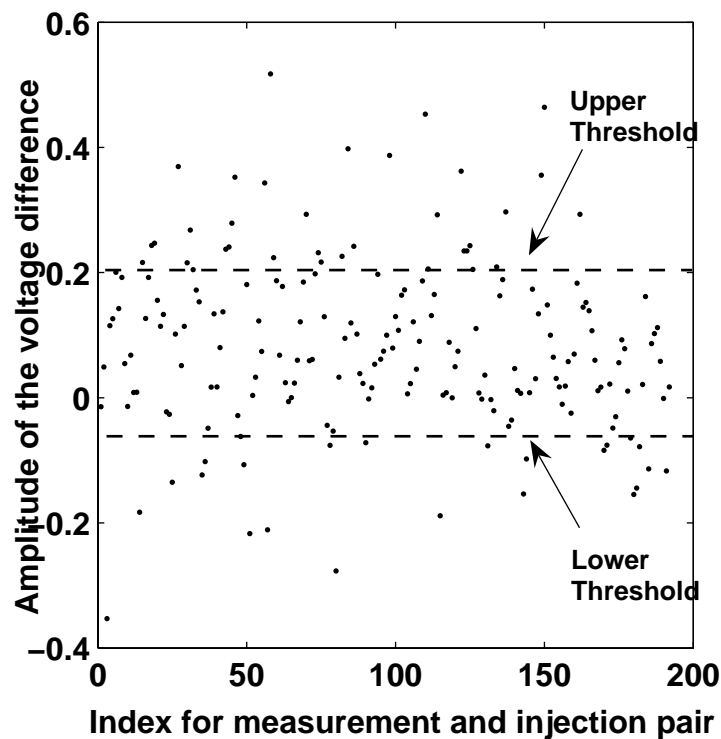


Figure 4.1 Upper threshold and lower threshold

As we can see from Figure 4.1, upper and lower thresholds are selected to isolate data points that are unusually large or small, respectively. The threshold values are the average value of the positive values for the upper threshold and average value of negative

values for lower threshold. Data points above the upper threshold and below the lower threshold are mapped to their respective measurement and injection pair. Electrodes that make up the measurement pair and injection pair are tallied, and the electrode with the maximum tally is labelled as erroneous.

This method functions effectively only in cases where the noise from the erroneous electrode dominates. The lack of an effective way to pick a threshold value, in addition to lack of proper definition for “good data” makes it impossible to rely on this method for consistent detection of electrodes. A more formal heuristic approach is introduced in Appendix 1, where electrode detection is carried out through analysis of certain statistical characteristics of each electrode’s data.

4.2 Detection through image reconstruction

This section proposes a formal approach to detect erroneous electrodes. This work has been accepted for publication in the Journal of Physiological Measurement (Asfaw and Adler, 2005).

We consider EIT difference imaging based on the formulation of Adler and Guardo (1996). The forward model estimates the vector of the change in log conductivity (\mathbf{x}) from a vector of change in difference measurements (\mathbf{z}) and with additive noise (\mathbf{n}). For small changes in \mathbf{x} , the relationship is linearized as in equation (2.17) repeated for convenience:

$$\mathbf{z} = \mathbf{H}\mathbf{x} + \mathbf{n} \quad (2.17) \text{ R}$$

Based on these parameters, the SNR of a measurement is $20 \log \|\mathbf{z}\| / \|\mathbf{n}\|$.

The sensitivity matrix (\mathbf{H}) relates the change in conductivity to change in difference measurements:

$$\mathbf{H}_{i,j} = \left. \frac{\partial \mathbf{z}_i}{\partial \mathbf{x}_j} \right|_{\sigma_b = \sigma_0} \quad (4.1)$$

The EIT image reconstruction algorithm estimates the change in conductivity ($\hat{\mathbf{x}}$) from measurements \mathbf{z} using a MAP regularization framework. $\hat{\mathbf{x}}$ is estimated by maximizing the *a posteriori* probability distribution $f(\mathbf{x}|\mathbf{z}) = f(\mathbf{z}|\mathbf{x})f(\mathbf{x})/f(\mathbf{z})$, which simplifies to:

$$\hat{\mathbf{x}} = [(\mathbf{H}'\mathbf{R}_n^{-1}\mathbf{H} + \mathbf{R}_x)^{-1}\mathbf{H}'\mathbf{R}_n^{-1}] \mathbf{z} = \mathbf{B}\mathbf{z} \quad (4.2)$$

The terms in equation (4.2) can be consolidated into a single reconstruction matrix \mathbf{B} . In order to estimate $\hat{\mathbf{x}}$ using a subset of the available measurements, the noise variance term \mathbf{R}_n on all unused measurements in (4.2) is set to ∞ (Adler, 2004). This has the effect of introducing zeros into \mathbf{R}_n^{-1} at positions on the diagonal corresponding to the unused measurements. We introduce the notation $\mathbf{B}(e_i, e_j)$ for the reconstruction matrix designed not to use measurements made with electrodes e_i and e_j .

4.2.1 Methodology for detection

In order to detect erroneous electrodes, we rephrase the problem to instead detect sets of good (not erroneous) electrodes, from which the erroneous electrodes are excluded. As mentioned previously, a set of good electrodes produces internally consistent data. Such consistency can be verified by estimating the measured data at each electrode in the set, using only measurements on other electrodes, and then comparing the estimate to the actual data measured. Thus, our method analyses difference EIT data from a set of electrodes S , in order to detect the presence of a single erroneous electrode. The above approach is termed as cross-validation of data in statistics (Efron, 1982). Figure 4.2 outlines the basic steps of the method.

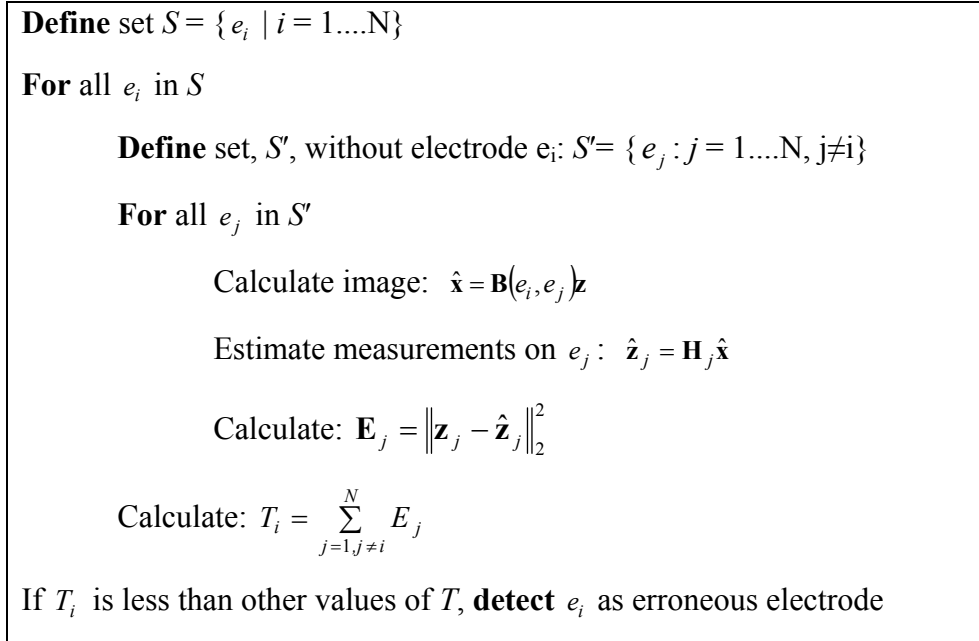


Figure 4.2 Pseudo code for detection of an erroneous electrode.

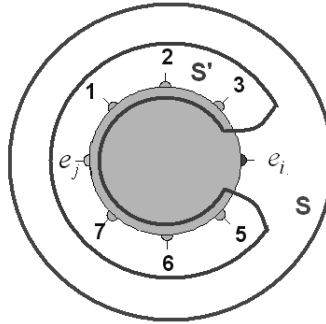


Figure 4.3 Illustration of electrode sets S and S' . To test electrode 4, the estimation error E_j is calculated for each electrode in set S' .

We iterate over each electrode e_i in S , forming a set S' of all electrodes not including e_i . S' is then tested to calculate a parameter T_i which reflects the consistency of measurements among electrodes in S' , and is the sum of estimation errors for all electrodes not including i (Figure 4.3). The estimation error for an electrode j is defined as:

$$E_j = \|\mathbf{z}_j - \hat{\mathbf{z}}_j\|_2^2 \quad (4.3)$$

Figure 4.4 shows a block diagram of steps for calculating E_j . \mathbf{z}_j is the vector of normalized differential measurements made using e_j , and $\hat{\mathbf{z}}_j$ is the estimate of \mathbf{z}_j based on all electrodes in S' except e_j (Figure 4.3), which is calculated by:

$$\hat{\mathbf{z}}_j = \mathbf{H}_j \hat{\mathbf{x}} \quad (4.4)$$

where \mathbf{H}_j represents the rows of the sensitivity matrix \mathbf{H} which correspond to measurements on e_j . $\hat{\mathbf{x}}$ is then calculated from (4.5), without data from electrodes e_i and e_j as

$$\hat{\mathbf{x}} = \mathbf{B}(e_i, e_j) \mathbf{z} \quad (4.5)$$

It is necessary to calculate (4.5) without electrodes e_i and e_j because e_i is not part of S' , and e_j is the electrode being estimated.

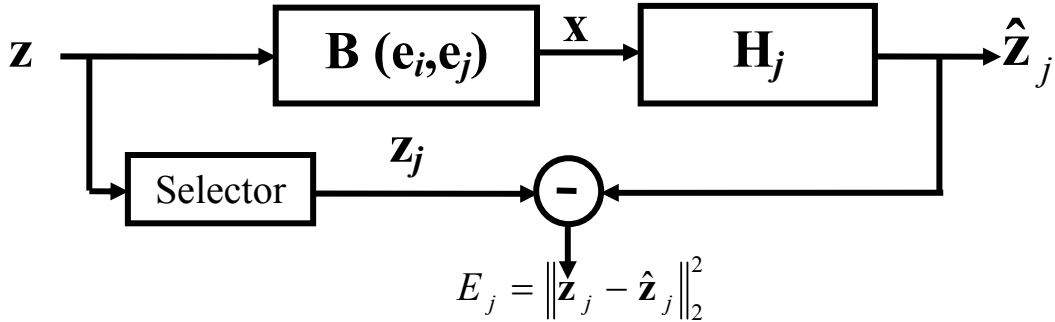


Figure 4.4 Block diagram of calculation for estimation error E_j

In order to efficiently compute \mathbf{E}_j in S' , we define a selector matrix, \mathbf{S}_j , such that $\mathbf{z}_j = \mathbf{S}_j \mathbf{z}$ to isolate the data from electrode e_j . Thus, (4.3) becomes

$$\mathbf{E}_j = \|\mathbf{S}_j [\mathbf{z} - \hat{\mathbf{z}}]\|_2^2 \quad (4.6)$$

Substituting $\hat{\mathbf{z}}$ with (4.4) and (4.5)

$$\mathbf{E}_j = \|\mathbf{S}_j [\mathbf{z} - \mathbf{HB}(e_i, e_j)\mathbf{z}]\|_2^2 \quad (4.7)$$

This can be written as

$$\mathbf{E}_j = \mathbf{z}^T (\mathbf{I} - \mathbf{B}(e_i, e_j)^T \mathbf{H}^T) \mathbf{S}_j^T \mathbf{S}_j (\mathbf{I} - \mathbf{HB}(e_i, e_j)) \mathbf{z} \quad (4.8)$$

The term $(\mathbf{I} - \mathbf{B}(e_i, e_j)^T \mathbf{H}^T) \mathbf{S}_j^T \mathbf{S}_j (\mathbf{I} - \mathbf{HB}(e_i, e_j))$ may be pre-computed, since it does not depend on the data. The T_i value for each e_i is determined by adding all \mathbf{E}_j of the set S' . If all values of T_i are low, S' contains all “good” electrodes, otherwise it contains at least one erroneous electrode. T_i values are tested against each other to detect if any are significantly less than the others. We have developed a simple heuristic measure known as prediction error ratio (*PER*) to measure this property. Initially, we define a parameter \mathbf{D}

$$\mathbf{D}_i = \sum_{j=1}^N |T_i - T_j| \quad (4.9)$$

Data with no error will have comparable T values, small variation in \mathbf{D} , and a ratio of maximum to minimum \mathbf{D} close to one. We express this ratio in dB and call it the *PER*:

$$PER = 20 \log \left[\frac{\min(\mathbf{D})}{\max(\mathbf{D})} \right] \quad (4.10)$$

A high *PER* indicates that the T values are close to one another and the data is consistent, while a low *PER* value indicates an erroneous electrode. *PER* is used to detect the presence of an erroneous electrode, and subsequently, T is used to identify it.

4.3 Electrode Error Detection in Static Imaging

The image reconstruction approach used in static imaging uses one set of data to implement the reconstruction. Consequently, it does not reduce systematic errors in static imaging. However, the detection of erroneous electrodes can be carried out by interpreting the data for difference imaging. A reference data set is selected and difference conductivity is calculated. After a match between the reconstruction image and real data, erroneous electrode detection can be applied as described in section 4.2. The

drawback of the above approach is the increased computation time necessary to carry out the forward and inverse problem for the detection method in addition to the static image reconstruction.

4.4 Drive Patterns and Detection

The method is applicable to adjacent and opposite current drive patterns and could possibly be applied to interleaved current drive patterns (Eyüboğlu, 1996). In adjacent current drive pattern, two adjacent electrodes are used for current injection and the remaining electrodes are used to make voltage measurements as shown in Figure 4.5. Overall, there are $N \times (N-3)$ measurements available when all electrodes give good data. However, when there is one erroneous electrode, the total number of measurements available is reduced to $(N-3) \times (N-4)$. Typically, with sixteen electrodes the remaining “good” data are sufficient to reconstruct a reasonable image (Adler, 2004).

In opposite current drive pattern, two opposite electrodes are used for current injection and the remaining electrodes are used to make voltage measurements as shown in Figure 4.5. There are $N \times (N-4)$ measurements available when all electrodes give good data. When there is one erroneous electrode, the total number of measurements available is reduced to $(N-4) \times (N-4)$.

01	X	X		*	*			X
12	X	X	X	*	*			
23		X	X	X	*			
34	*	*	X	X	X	*	*	*
45	*	*	*	X	X	X	*	*
56				*	X	X	X	
67				*	*	X	X	X
70	X			*	*		X	X
	01	12	23	34	45	56	67	70

(a)

04	X	*	*	X	X	*	*	X
15	X	X		*	X	X		
26		X	X	*	*	X	X	
37			X	X	*		X	X
40	X	*	*	X	X	*	*	X
51	X	X		*	X	X		
62		X	X	*	*	X	X	
73			X	X	*		X	X
	01	12	23	34	45	56	67	70

(b)

Figure 4.5 Data available for an eight electrode EIT system using (a) adjacent drive and (b) opposite drive with one erroneous electrode. The vertical axis represents electrode pairs used for current injection and the horizontal axis those used for voltage measurement. “X” represents data not available from electrodes used for current injection. “*” represents data lost when electrode 4 is erroneous.

The approach to detection of erroneous electrode does not change depending on the current pattern used. However, the performance is affected by the total number of independent measurement available to estimate the data from the candidate electrode. Looking at an eight electrode system, an adjacent current drive pattern has 40 measurements available while opposite drive pattern has only 32 data points. With one erroneous electrode, available data points for adjacent current drive pattern are reduced to 20, by 50%. The opposite current drive pattern has only 16 data points, which is also reduced by 50%. As the number of electrode increases the impact of the removed electrode is diminished. For example, in a 16 electrode system available data points are only reduced 25% by one erroneous electrode.

Overall, as the number of independent measurements increases we expect a more accurate estimation data from an electrode. In opposite current drive pattern only four independent current drive pairs are available and only half of the measurements are unique. On the other hand, an adjacent current drive pattern has measurements the eight independent pairs. Hence, an adjacent current drive pattern could result in a better estimation *vis-a-vis* a more robust detection of erroneous electrode than opposite current drive pattern.

4.5 Implementation

This method was implemented in Matlab, using a FEM mesh of 256 elements on an Athlon 1.8GHz computer, which requires approximately 74 s to pre-compute the values in equation (4.9) and a further 3 s to calculate the *PER* and *T* for each EIT difference data set. The major code base for the forward and inverse solver was implemented by Adler (1996), while the code to implement error detection was written by this author. The forward solver uses a finite element mesh generator able to produce mesh of 64, 120, 216, 256, 576, and 352 with shapes of basic circle, human thorax, and dog thorax. The inverse solver uses the one step MAP image re-constructor formulated in Chapter 2. The Matlab code for the detection algorithm is provided in the Appendices.

4.6 Data

EIT data were obtained from previous experiments (Adler *et al.*, 1997). Mechanically ventilated mongrel dogs had sixteen ECG-style electrodes spaced evenly around the shaved thorax 10 cm above the base of the rib cage, and adjacent drive EIT measurements were acquired. Four animals, of ten, showed some level of electrode errors. Images were calculated corresponding to data measured at each inspiration. To avoid contribution from ECG signals the measurements were taken 100ms after the QRS peak.

4.6.1 Simulated Erroneous Data

The characteristic of noise in EIT was considered in Chapter 3; the noise may come from different sources, and it could display different statistical characteristics. Since the focus of this thesis is detection of erroneous electrodes a generalized Gaussian noise model is used, however the methods are applicable to general noise. We have also shown that noise in EIT is non-stationary with varying statistics, such as mean and variance, over time. However, detection is performed on a single difference measurement over a time difference Δt . The noise characteristics over Δt are treated as non-stationary Gaussian. Thus, simulated erroneous data are generated using representative non-erroneous data and additive Gaussian noise. Elements of the measured difference data vector, \mathbf{z} , vary significantly in magnitude from each other, by up to four orders of magnitude. The low level signal of the difference measurement is dominated by noise significantly unless the additive noise also reflects this difference. Therefore, the signal power is measured and the additive noise data will have relative magnitude for each data point.

A simulated erroneous data are assumed to have one erroneous electrode from either adjacent or opposite drive pattern measurement. Gaussian noise is added to all data related to the electrode selected to be erroneous. Simulated erroneous data for an adjacent drive pattern are generated from representative clean data. For the opposite drive pattern, we do not have access to experimental data; therefore simulated data were used. The ability to manipulate the data set gives us the opportunity to test the performance of the method and its sensitivity to noise. However, there are important issues in using

simulated data to validate inverse solutions. These issues have been called the “inverse crime” (Lionheart, 2004). The next section explains the concept of “inverse crime” and its implications in validation of methods that use forward and inverse model approach.

4.6.1.1 Inverse Crime

The term “inverse crime” is used when the forward and inverse model geometry are identical, and thus data simulation and reconstruction use the same model (Wirgin, 2004). This means that any inadequacies in the model may be masked. For this reason, results from a study in which simulation data are generated via an “inverse crime” are regarded with scepticism. In order to avoid this problem, the synthetic data should be modelled through a separate forward solver that is geometrically different from the inverse solver. In this work, this is accomplished by simulating data using the forward solver of EIDORS 3D, while the inverse calculations are based on the work of Adler and Guardo (1996). EIDORS 3D provides us with a toolbox to simulate and obtain the estimated measured difference voltage measurements, and is discussed in chapter 5. The block diagram of Figure 4.6 demonstrates the steps taken to generate and create simulated erroneous data.



Figure 4.6 Block Diagram for generating simulated data

The data generated by EIDORS 3D are based on a three dimensional model and the MAP inverse solver in works two dimensions, and only requires data from only one ring of electrodes. The expected image through the synthesis in EIDORS3D is shown in Figure 4.7. Comparing it to the reconstruction using the MAP solver we see that we have obtained the expected results.

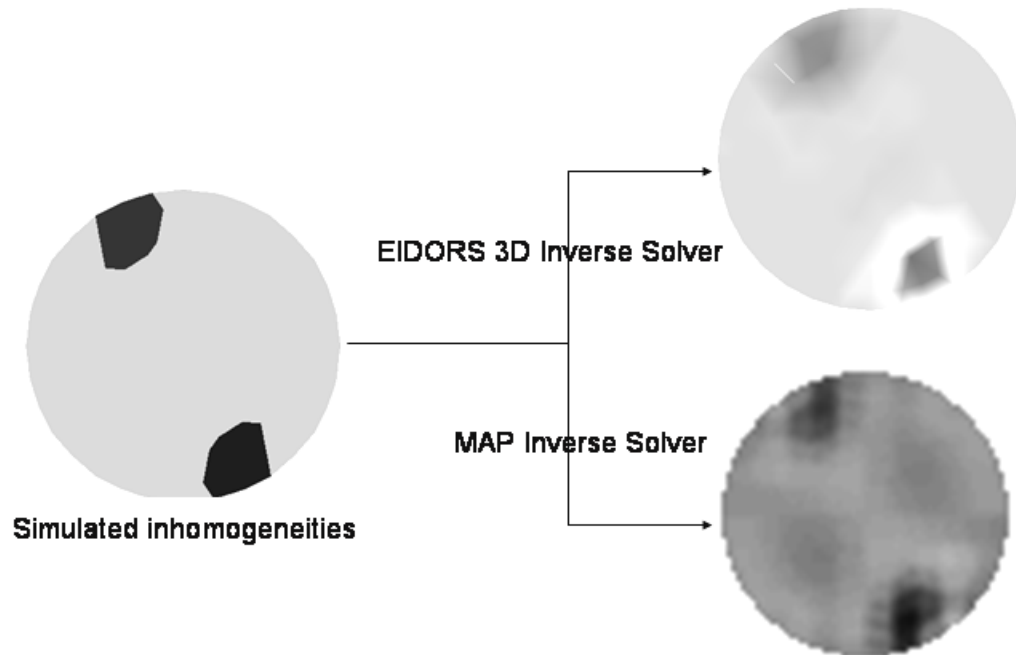


Figure 4.7 Reconstructed images of EIDORS3D inverse solver and MAP inverse solver (Adler and Guardo, 1996)

4.6.2 Real Erroneous Data

The gold standard for erroneous electrode data was based on human assessment. A graphic user interface was developed to evaluate test images by five experienced users, who were asked to classify each image as either: *no error*, *possible error*, or *definite error*. Identification of images with no error was consistent, but there were varying assessments of images considered to have possible error and definite error. For each experimental session, the reconstructed differential images were converted into a frame of a movie to allow for better identification major changes in conductivity caused by erroneous electrodes. The users reviewed a hundred images and classified each one to a particular category using the GUI shown in Figure 4.8. We used majority opinion to classify images.

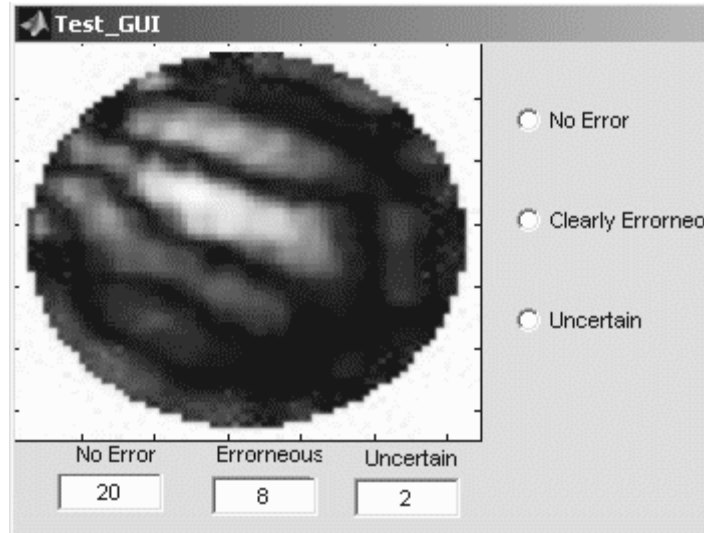


Figure 4.8 GUI used for classification of selected data by expert users

4.7 Results

Tests were carried out on both simulated erroneous data and real erroneous data described in the previous section. In addition, tests were performed to measure the level of accuracy/robustness of the method, such as SNR vs. PER (\pm std dev). The impact of multiple erroneous electrodes on the method developed for single electrode detection is also investigated.

4.7.1 Experimental data with simulated error

Figure 4.9 shows EIT data classified as *no error*. The original image was generated from data acquired from ventilated dog (of tidal volume 800ml) after the electrode had been attached for one hour. The graph of T vs. electrodes (Figure 4.9 (a)) shows consistent values of T corresponding to a PER of -13dB, which was found to indicate good electrodes. Figure 4.9 (b) shows the reconstructed image of data from Figure 4.9 (a) with additive white Gaussian noise (SNR= -10dB) to the data of electrode 5. The resulting reconstructed image is poor with large artefacts. When the detection method is applied to these data, T values from all electrodes except electrode 5 are consistent (Figure 4.9 (b), bottom), which suggests that electrode 5 is erroneous.

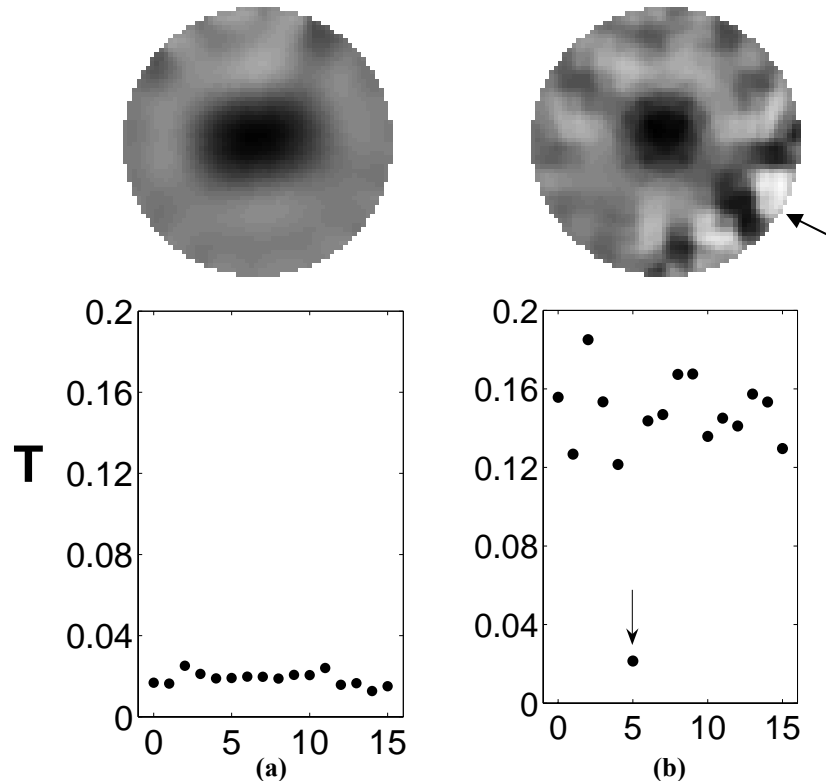


Figure 4.9 T vs. Erroneous electrode for experimental data with simulated error

4.7.2 Erroneous experimental data

Three sets of representative EIT data of ventilated dogs were used: data with no error (Figure 4.10 (a)), a small error (Figure 4.10 (b)), and major error (Figure 4.10 (c)) (based on our experience of EIT errors). The data set with no error was acquired from 100ml saline installation and 500ml ventilation into the lungs after approximately three hours of attaching the electrodes. Data with small error were acquired from a separate experiment where the electrodes have been attached for more than three hours with 500ml ventilation. The data set with major error (Figure 4.10 (c)) was taken from an experiment where the electrodes have been attached for more than seven hours and with ventilation of 500ml.

The reconstructed images and graphs of T vs. electrode number are shown. Data with errors (Figure 4.10 (b) and (c)) show higher overall values of T_i , compared to error free data (Figure 4.10 (a)). In the case of Figure 4.10 (c), two adjacent electrodes are detected. We have noted that this is not uncommon result for this method with larger data errors.

Based on our experience with this data set, we believe that the adjacent electrodes are both erroneous. To test this result, a data set with no errors was selected and varying levels of white Gaussian noise were added to two adjacent electrodes. Result shows that the two adjacent electrodes have a low T value compared to the remaining electrodes.

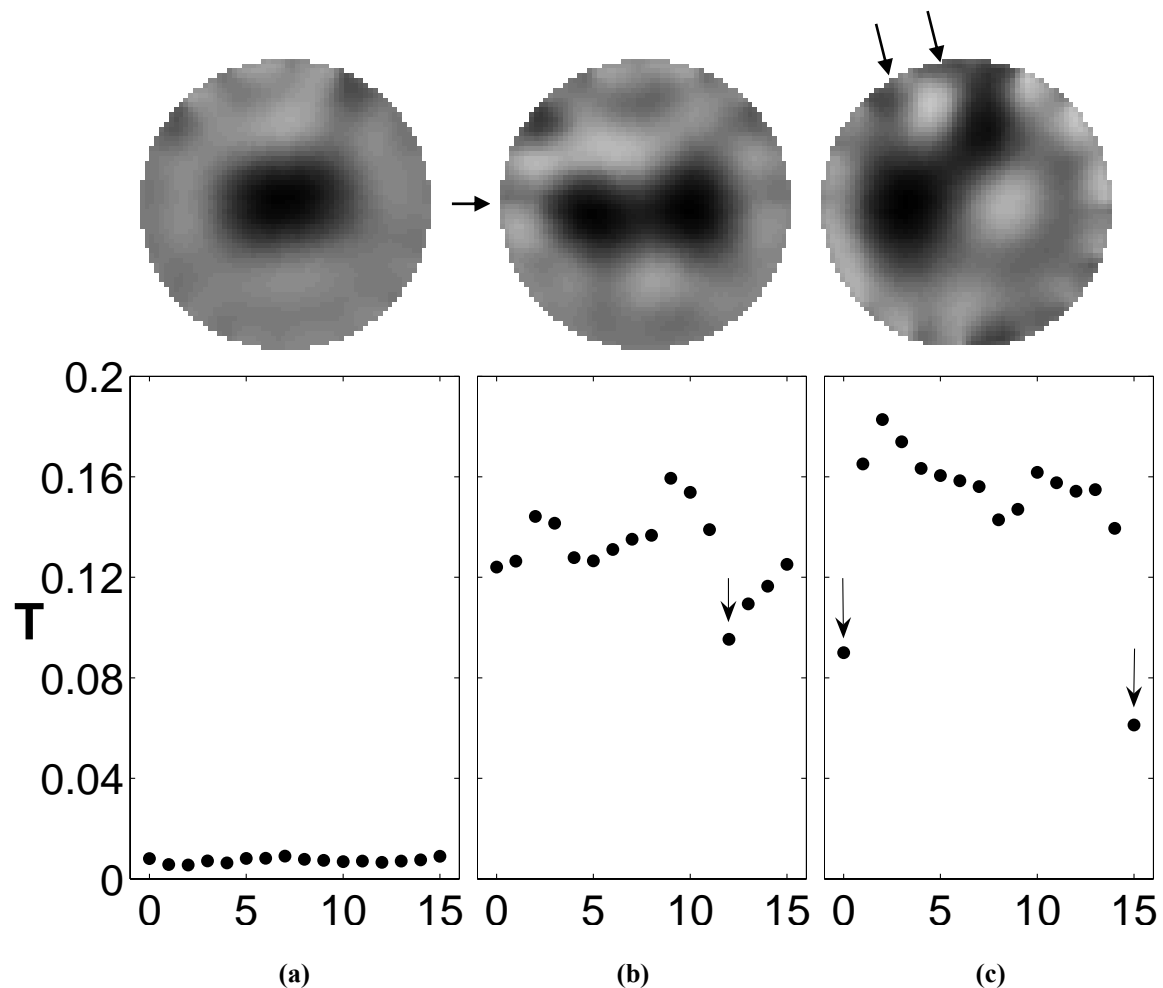


Figure 4.10 Electrode detection in real data: *Upper row:* (a), (b) and (c): images of tidal ventilation in a dog. Electrodes are numbered clockwise with electrode zero at the top centre. Images are individually normalized to the colourscale (arbitrary units) at right. *Bottom row:* parameter T for each electrode (a) no erroneous electrode (b) data with erroneous electrode with small error signal. (c) data with erroneous electrode with typical error signal. Arrows show the location of the erroneous electrode(s).

4.7.3 Simulated data with error

SNR vs. PER (\pm std dev): To determine the effectiveness of the method data for adjacent and opposite drive pattern was acquired from EIDORS3D. These calculations were made with simulated data in order to be sure to control the level of erroneous electrode data. The PER value is then calculated for varying levels of additive noise applied to the data from one particular electrode. For results shown in Figure 4.12, PER was calculated for SNR values (-60 dB to 60 dB). Each SNR simulation was repeated 100 times in order to calculate the estimation error. The noise introduced to the data was generated using the `awgn` function of Matlab, which uses the `randn` function to generate the white Gaussian noise values. The generator of the `randn` produces different values for each trials with a fixed SNR value, which gives varied results for the PER value.

Figure 4.12 shows SNR vs. PER (\pm std dev) and indicates that this method can reliably detect an erroneous electrode when the SNR less than 0 dB. Such a level of SNR has a little perceptible visual impact on the reconstructed image (Figure 4.11). The detection method works for each injection pattern. The detection threshold in both patterns is between -22 to -23 dB.

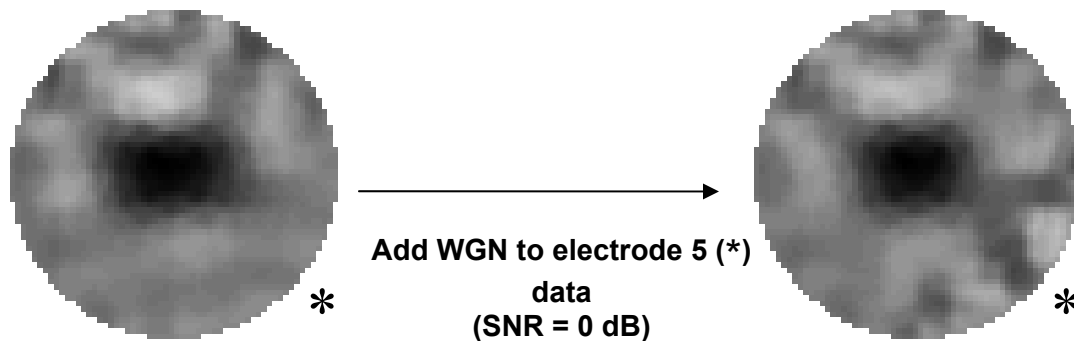


Figure 4.11 WGN to clean data: 0dB noise has a visually little imperceptible impact

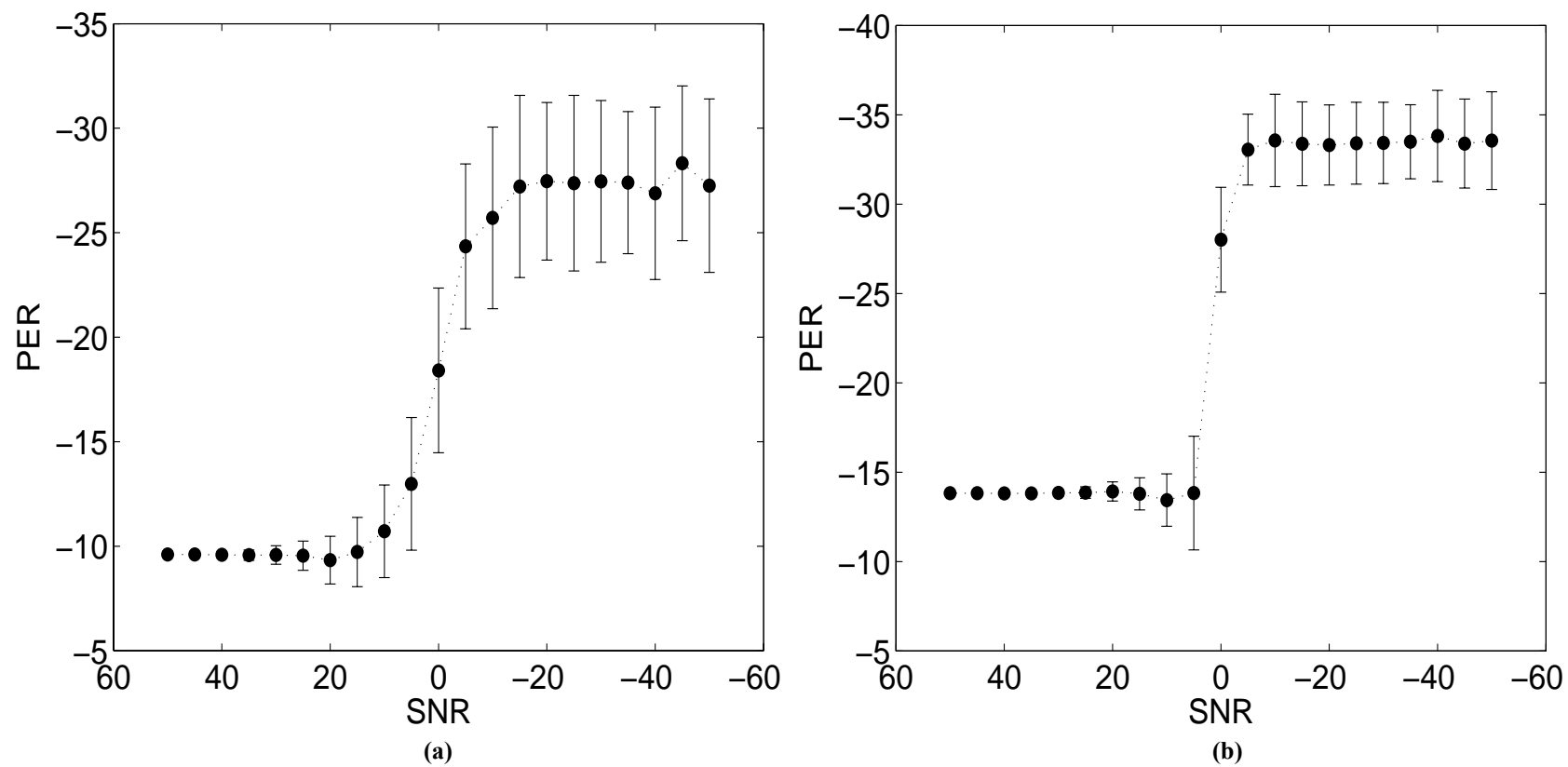


Figure 4.12 SNR vs. PER (\pm std dev) on simulated data: (a) Opposite Drive Pattern (b) Adjacent Drive Pattern

4.7.4 Multiple erroneous electrodes

When the method is applied to multiple erroneous electrodes the resulting T vs electrode graph appears like that of Figure 4.13. The data set was taken from one particular experiment where the dog had a skin condition that made it difficult to attach electrodes. The result shown in Figure 4.13 (a) was data acquired with 700ml ventilation after the electrode had been attached for an hour and twenty minutes. The second image (Figure 4.13 (b)) was from data acquired after one hour and forty minutes with 100ml saline instillation. The third image was with 700ml ventilation with 100ml saline instillation after one hour and fifty minutes of attaching the electrodes. Looking at the graph we can deduce that there are multiple erroneous electrodes on 3, 5, 12, and 13.

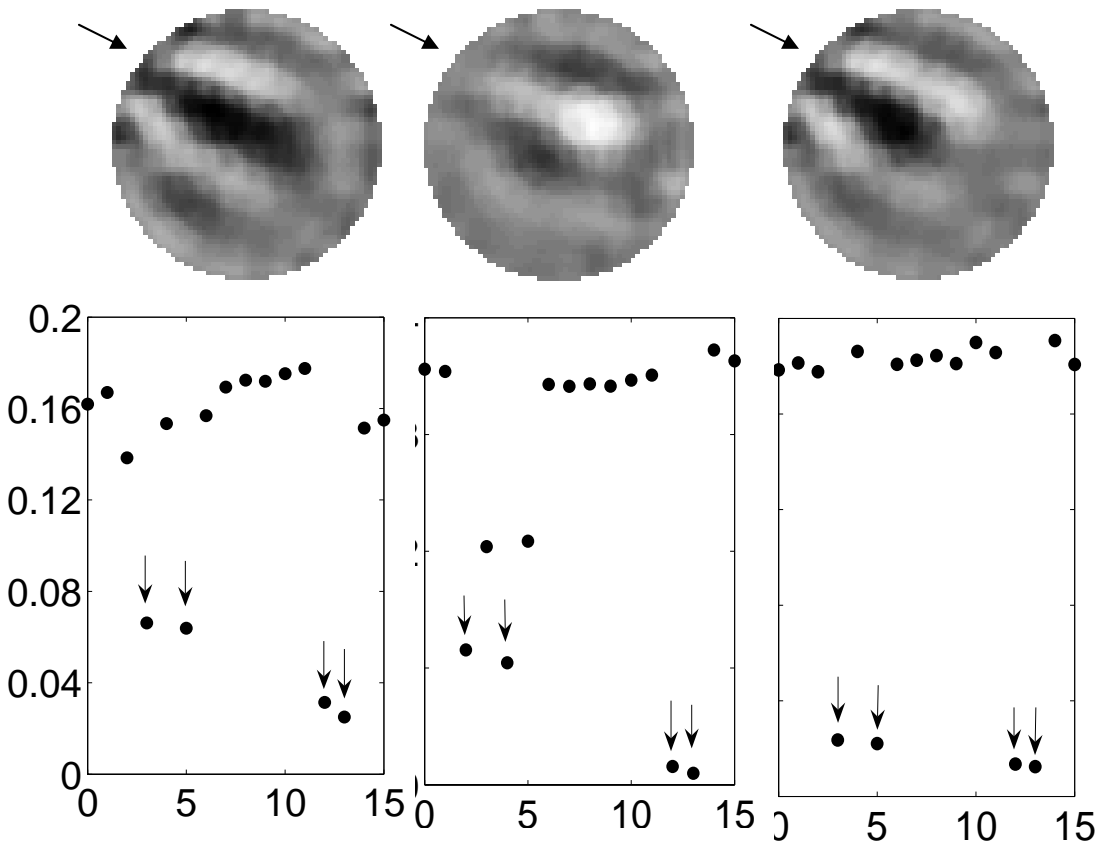


Figure 4.13 T vs. Erroneous electrode for real erroneous data. Note there are multiple erroneous electrodes near the arrows.

4.7.5 Compensation of erroneous data

Correction and compensation of data from erroneous electrode was implemented using the method introduced by Adler (2004). The result of the compensation is demonstrated in Figure 4.14(a) shows the original image of the experiment from the ventilated dog (700ml ventilated and 100ml saline installation). After applying the compensation scheme described in chapter 3, the resulting image is shown in Figure 4.14 (b). It is clear that the artefacts have disappeared and the result looks much like what we would expect if there was no erroneous electrode.

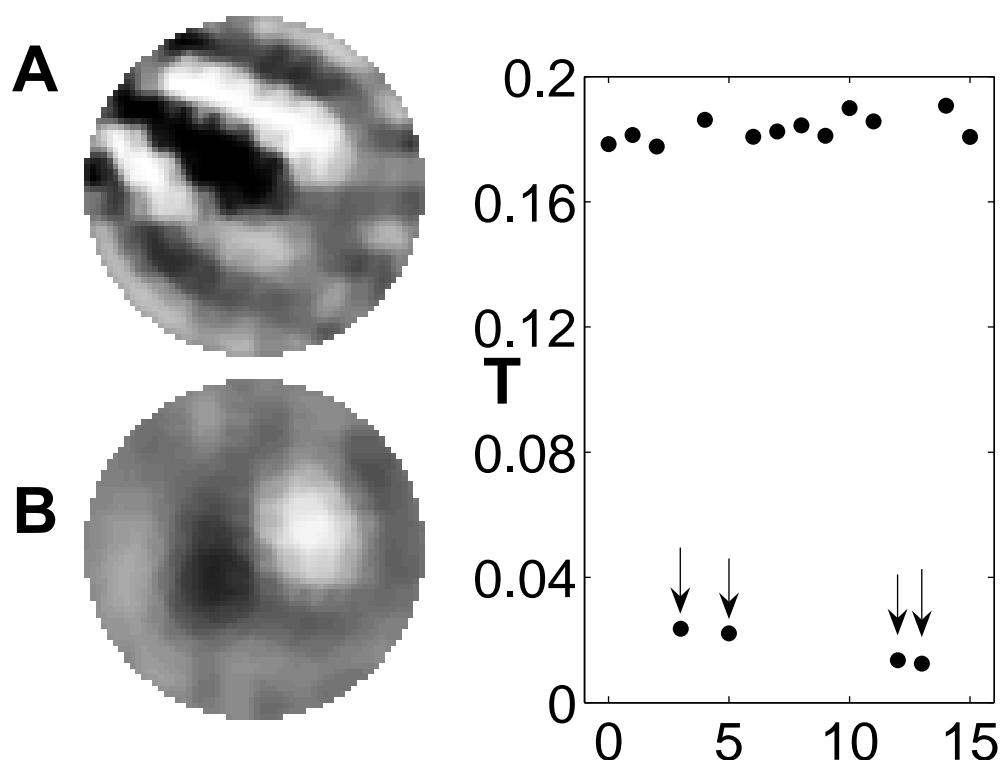


Figure 4.14 Compensation of Erroneous electrodes: *Left (A)*: difference image of 700ml inspiration and 100ml right lung fluid installation in a dog. Electrodes are numbered clockwise with electrode zero at the top centre. Both images normalized to same colourscale. *(B)*: Image of data from *(A)* using the method of Adler (2004) to compensate for the erroneous electrodes identified below. *Right*: T for each electrode in *(A)*. Based on these data, electrodes 3, 5, 12, 13 were identified as erroneous.

4.8 Discussion

The chapter presented a method to automatically detect an erroneous electrode in EIT. It presents a formal approach for detection of erroneous electrodes compared to the heuristic method discussed in section 4.1. The method is based on testing that an erroneous electrode produces measurements inconsistent with those from other good electrodes. Results show that the method is able to correctly detect the presence and identify the location of erroneous electrodes in experimental and simulation data.

The recommended detection threshold PER is -22dB determined from Figure 4.12. In comparing the results obtained from the method to the user classification, both the method and the user classification generated a comparable percentage of *definite error* data, 28% and 25%, respectively. The method detected 57% of the images as *no error*, while the user classification provided 67%, probably due to some errors not being visible in the reconstructed image as demonstrated in Figure 4.11. After detection of an erroneous electrode it would be possible, in a real time measurement scenario, to identify and correct the underlying problem. If data collection is already complete, it would be possible to compensate for the erroneous electrode using a technique such as that of Adler (2004). Figure 4.14 shows an example of such compensation for data that has large number of errors due to the animal's poor skin condition.

This method was also evaluated using simulated data for an opposite drive pattern and shows similar results to those in Figure 4.12. Unfortunately, we do not have experimental data to confirm the results of the opposite drive pattern. However, looking at the detection threshold and SNR vs. PER (\pm std dev) graph for opposite and adjacent drive pattern, we conclude that the method works well irrespective of the drive pattern.

Tests were carried out to evaluate the performance using different size finite element meshes, other than the 256 element mesh used for the results in this thesis. A finer mesh grid (>256 elements) results in longer execution time with a slight increase in separation of T values for erroneous electrodes. The finer mesh results in better estimate of the potential distribution of the forward model and more accurate estimate of the voltages.

Even though this method was not developed to detect multiple electrode errors, the results (Figure 4.13) appear to show the ability to detect two adjacent erroneous electrodes. The T value decreases at an erroneous electrode position because the error contribution from that electrode is eliminated. In the case of multiple erroneous electrodes, part of the error contribution is removed even though contribution from other electrodes remains. Thus, the technique can detect multiple erroneous electrodes, although with reduced sensitivity. To test this result, a data set with no errors was selected and varying levels of white Gaussian noise added to two adjacent electrodes. Results show that the two adjacent electrodes have a significantly lower T value than the remaining electrodes. A better approach to detect two erroneous electrodes would be selecting two or more candidate electrodes in the set S , and calculating the respective \mathbf{E}_j for all e_j in S' (Chapter 6).

This method for detection of erroneous electrodes could also be used for static EIT applications. Static EIT is more sensitive than difference EIT to measurement errors (Korjenevsky, 1997), and management of these errors is important for algorithm stability. Since an electrode error should be present whether measurements are interpreted as static or difference data, we propose that the method described here could be applied in static EIT by performing the test for errors on sets of EIT difference measurements, while the actual reconstruction is done statically.

Automatic detection of electrode errors in EIT has several possible applications. In offline processing, such a technique could identify and correct for such errors. More usefully, if implemented in EIT monitoring equipment, it would be possible to alert staff who could then attend to the problem. However, for such online applications, the algorithm is not real-time (3s per data set with a pre-processing time of one minute), but would permit erroneous error detection as a separate process.

Chapter 5

Error Detection in 3D EIT

Most industrial and medical electrical imaging problems are inherently three dimensional (Polydorides and Lionheart, 1999). Hence, the data collection and forward modelling would be most accurately carried out three dimensions. The Electrical Impedance and Diffuse Optical Reconstruction Software (EIDORS3D) is freely available software that can be used to reconstruct electrical or optical material properties from boundary measurements in 3D. As discussed previously, non-linear and ill-posed problems such as electrical impedance and optical tomography are typically approached using a finite element model for the forward calculation and a regularized non-linear solver for obtaining a unique and stable inverse solution.

In 3D EIT, various electrode configurations are possible. Typically, electrodes are placed in equally spaced rings on several parallel planes where each ring may have 8, 16, or 32 electrodes. A measurement is done using electrodes in the same plane as well as in electrodes in the lateral direction. The current pattern is selected so as it efficiently utilizes the electrode configuration. EIDORS3D provides the option of using opposite and adjacent current injection pairs that follow similar convention as in the two dimensional case. Figure 5.1 shows a finite element mesh used in EIDORS3D with two electrode rings, each ring with 16 electrodes.

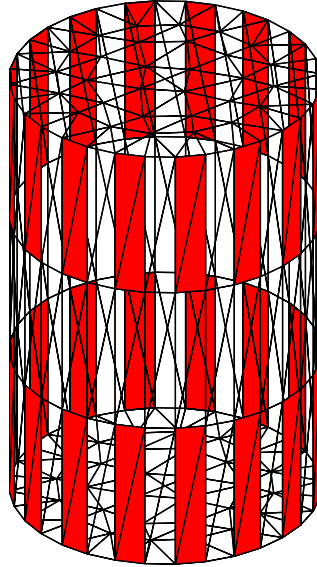


Figure 5.1 Finite Element mesh in EIDORS3D with two electrode rings

5.1 Finite Element Model and forward problem in EIDORS3D

EIDORS3D finite element solver uses the complete electrode model to compute approximate solutions to boundary value problems involving models with first order tetrahedral elements (Polydorides and Lionheart, 1999). Meshing is performed according to some preset meshing parameters such as the mesh granularity, maximum number of elements and maximum edge size. As in the two dimensional case it is important that the elements near the boundary and especially near the electrodes are small enough to preserve the accuracy of measurements.

Similar to the two dimensional case the forward problem deals with the construction of an admittance matrix (\mathbf{P}) and estimating the distribution of the electric field (\mathbf{U}). The electric field distribution is used to calculate the sensitivity matrix (\mathbf{H}). The assembly of the admittance matrix differs significantly due to the increased complexity caused by the increase in dimension and electrodes involved. A common ground is selected to be able to calculate a unique forward solution. EIDORS3D uses the Cholesky method or preconditioned conjugate gradients for real admittivity vector. Alternatively, LU method or biconjugate gradients are used when the admittivity vector is complex valued.

5.2 Regularization in EIDORS3D

EIDORS3D adopted a Tikhonov type regularization approach where a variable regularization parameter is employed. The idea is based on minimizing the residual error for a specific admittivity (ξ)

$$f(\xi) = \frac{1}{2} (F(\xi) - \mathbf{V})^* (F(\xi) - \mathbf{V}) = \frac{1}{2} \|F(\xi) - \mathbf{V}\|_2^2 \quad (5.1)$$

The difference is to be expressed as follows

$$D(\xi) = (F(\xi) - \mathbf{V}) \quad (5.2)$$

Where: $F(\xi)$ is the non-linear forward operator, $f(\xi)$ is the residual error and \mathbf{V} is the vector of voltage measurements. The Taylor series expansion of $D(\xi)$ is

$$D(\xi + h) = D(\xi) + D'(\xi)h + \frac{1}{2} D''(\xi)h^2 \quad (5.3)$$

h is a small step of increments. Simple minimization based on Newton-Raphson iteration can be accomplished using a step h where $D(\xi + h) = 0$. But the ill-posed and ill-conditioned nature of the problem does not change from two dimensions to three dimensions. Consequently, it is necessary to apply a regularized approach to the inverse problem. The Tikhonov regularization expressed as

$$f(\xi) = \|F(\xi) - \mathbf{V}\|_2^2 + \lambda \|L(\xi - \xi_k)\|_2^2 \quad (5.4)$$

The first term favours matching the measured data and the second term favours smoothing based on some prior assumptions about ξ . The hyper parameter value λ controls the amount of smoothing that is to be applied.

5.3 Electrode error detection in EIDORS3D

As in 2D, the linearized form of the forward and inverse solution is set up for 3D EIT in EIDORS3D. Both the sensitivity matrix (\mathbf{H}) and the reconstruction matrix (\mathbf{B}) are extracted to apply the method described in chapter 4. The toolbox for EIDORS3D provides us with the sensitivity matrix (Jacobian) using the `Jacobian_3D` function. The estimate of the conductivity distribution without e_j is calculated using the same MAP regularized scheme shown in equation (5.5).

$$\hat{\mathbf{x}} = (\mathbf{J}^T \mathbf{W}_{i,j} \mathbf{J} + \lambda \mathbf{Reg}^T \mathbf{Reg}) \setminus \mathbf{J}^T \mathbf{W}_{i,j} \quad (5.5)$$

Where \mathbf{J} is the sensitivity matrix, λ is the hyperparameter and \mathbf{Reg} is the first order smoothing prior. $\mathbf{W}_{i,j}$ is the weighting matrix used to remove contribution from electrode e_j and e_i . The data are estimated back by applying the forward model:

$$\mathbf{z}_j = \mathbf{J} \hat{\mathbf{x}} \quad (5.6)$$

The equations (5.5) and (5.6) are combined to into one matrix, which needs to be recalculated for each pair of electrodes. The step for detection and identification of erroneous electrode is similar to that of the case in 2D. However, due to increased number of electrodes and elements the matrices are much bigger and the execution time is considerably longer.

5.4 Data

We do not have 3D EIT data other than from EIDORS3D simulations. We used FEM mesh with simulated conductivity difference shown in Figure 5.2. As discussed in chapter 4, validation of the detection method through simulated data needs careful consideration due to the possibility of committing the inverse crime (Wirgin, 2004). To avoid the inverse crime, we have to use a forward model that is mathematically distinct from the inverse model. For the result shown in Figure 5.2, the forward model uses the preconditioned conjugate gradients and the inverse model uses the regularized Tikhonov approach. The simulated voltage measurements were generated based on the forward model, after which a measured simulated noise is added. The sensitivity matrix

(Jacobian) used in the Tikhonov regularization is constructed based on the same forward solver of the preconditioned conjugate gradients. Figure 5.2 shows the performance of the EIDORS3D inverse solver. The result shows the reconstructed image along different slices. Based on the above simulated result, we are able to test the detection algorithm for 3D EIT.

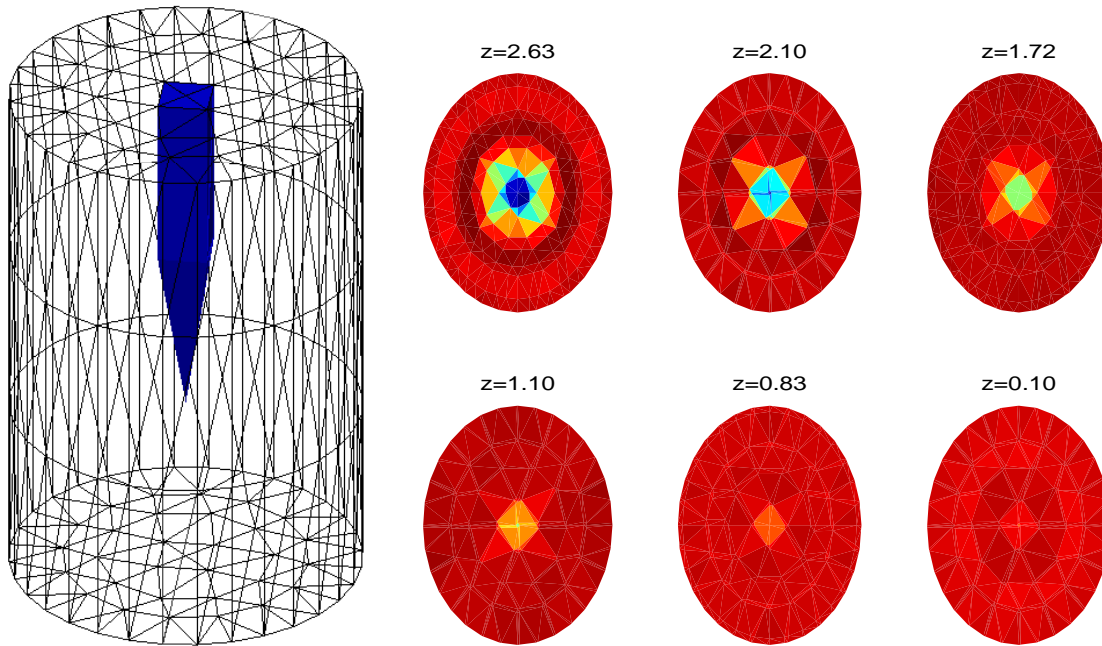


Figure 5.2 Simulated conductivity difference and its reconstruction at different positions

An adjacent drive pattern protocol was selected, where measurements are carried out using adjacent electrodes regardless of plane they are located in. Hence, measurements are carried out between electrodes of the same plane as well as electrodes of different planes.

5.5 Result

The forward model of the EIDORS3D provides us with simulated voltage measurements. Following a similar procedure as in 2D EIT, the data from a specific electrode are selected and white Gaussian noise is added. When adding noise to the simulated difference measurement, the detection method consistently identifies the erroneous electrode for SNR below 10 dB. Figure 5.3 (a) is the result of the detection method when

simulated white Gaussian noise was added to data of electrode 8. The corresponding SNR vs. PER (\pm std dev) graph shows that the detection threshold is approximately PER=-22.5 dB.

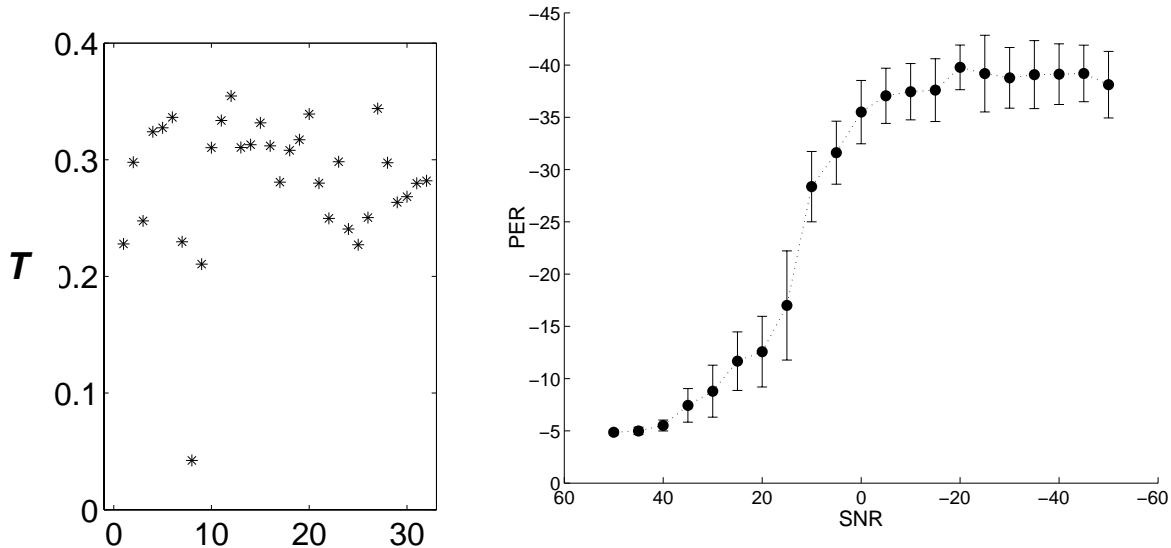


Figure 5.3 SNR vs. PER (\pm std dev): (a) -20 dB noise on data from electrode 8. (b) Corresponding PER value for different SNR values.

5.6 Discussion

The detection method described in chapter 4 appears to be independent of measurement process or dimensionality of the problem. The one essential requirement is that the measurement from an electrode be related to the measurements from the other electrodes. In both 3D and 2D EIT, these measurements are related via the sensitivity matrix and reconstruction matrix. Thus, it is expected that the method would work for 3D EIT under EIDORS3D. However, a number of questions were raised by the EIDORS3D results. The most important one was: by using simulated data from EIDORS3D and running detection algorithm using EIDORS3D are we committing an inverse crime? Lionheart (2004) suggests using a much finer mesh for the inverse problem, if finite element based forward solver is used. The issue of inverse crime was handled based on the suggestion of Lionheart (2004). We use conjugate gradient method for the forward model and Tikhonov regularization approach for the inverse model. The two methods do have

mathematical connectivity and we cannot confidently say that inverse crime is not committed as defined by Wirgin (2004).

This method cannot be used as real time detection method due to the considerable amount of computation that needs to be done. On an Athlon 1.8 GHz, 384 MB system, one run for detection an electrode takes approximately 5 minutes for a 32 electrode system. This 5 minute compares to 3s for the 2D results of chapter 4. The primary reason for this long computation time is the memory limitation, and the requirement to load and unload Jacobian matrices on demand. Most of the computation time takes place when combined/modified sensitivity and reconstruction matrix is multiplied by the original voltage measurement to calculate the estimated voltage measurement for electrode e_j per each candidate electrode e_i . The combined sensitivity and reconstruction matrix is pre-calculated for each possible e_j and e_i pair.

Chapter 6

Detection of Multiple Erroneous Electrodes

The method described in chapter 4 only explored the possibility of error detection of a single erroneous electrode. But in long term applications of EIT, it is likely that multiple erroneous electrodes will occur. This chapter explores the manner in which the single electrode error detection method can be modified to allow for detection of multiple erroneous electrodes. The approach to detection of two erroneous electrodes is provided along with results based on simulation and experimental data.

6.1 Identification of Multiple erroneous electrodes

Poor electrode contact can occur due to patient movement (Blott *et al*, 1998), or sweat and peripheral edema, especially in long term monitoring applications (Lozano *et al*, 1995). For the above reasons it is possible to have more than one electrode having poor contact. Experience has shown that it is not possible to judge the number of erroneous electrodes based on the resulting reconstructed image, but simply the presence of at least one erroneous electrode.

While testing the method developed for a single erroneous electrode, some of the data sets that have been clearly identified as having an erroneous electrode exhibited unusual results. One possible example is the data set shown in Figure 6.1 (a); the image shows that there is a possible erroneous electrode around electrode 0 or 15. When the method for detection of single erroneous electrode was applied the result suggested that both electrode 0 and 15 were erroneous with reduced sensitivity. The existence of multiple erroneous electrodes had to be confirmed through simulated results. Simulated erroneous data were generated from representative clean data by applying white Gaussian noise on data sets contributed by the candidate electrodes.

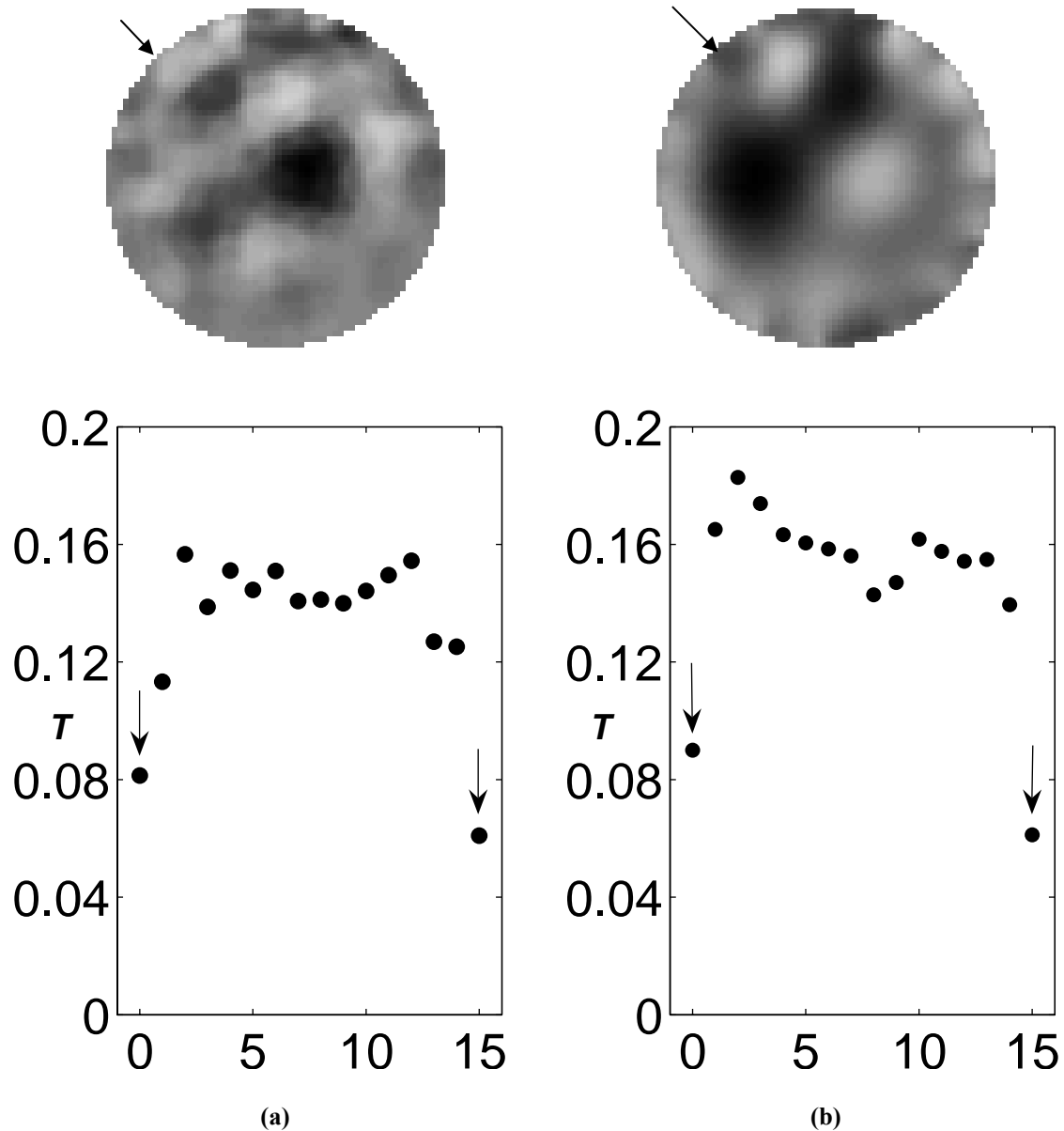


Figure 6.1 Two erroneous electrodes from both simulated noise and experimental noise: (a) simulated noise added to representative non-erroneous experimental data for electrodes 0 and 15 (b) experimental noise observed on electrode 0 and 15

The T vs. electrodes for both simulated and experimental erroneous data show similar results. In both cases, electrodes 0 and 15 have the lowest T values qualifying them as erroneous electrodes. In addition, the result gives reason to develop a method for detection of multiple erroneous electrodes.

6.2 Multiple erroneous electrodes detection method

Chapter 4 illustrates the success at detection of a single erroneous electrode. In addition, it showed a measure of success in detection of multiple erroneous electrodes. This prospect leads us to consider a formal approach for multiple erroneous electrodes. The core idea for detection of single erroneous electrode is based on an accurate estimation of measurements from all good electrodes through the reconstruction algorithm. Moreover, significant discrepancy exists between actual and estimated data for erroneous electrode due low signal level of EIT and dominant nature of noise. The same concept is extended to the detection of multiple erroneous electrodes.

Generally, the extension of the original method is based on removing all electrodes suspected to be erroneous. Hence, if two electrodes are suspected to be erroneous, a set S is defined such that all possible combinations of two electrodes are listed. Each possible pair is removed and an estimation of measurements is carried out on the remaining electrodes, see Figure 6.3. A reconstruction matrix (\mathbf{B}) is generated such that all contributions from e_i, e_j and e_k are removed, expressed as $\mathbf{B}(e_i, e_j, e_k)$. Based on the modified reconstruction matrix, the estimated conductivity distribution ($\hat{\mathbf{x}}$) is calculated for e_k . The estimation error is determined for all electrodes defined in S (Figure 6.2) and T is determined for each pair of electrodes defined in S . If the T value of a specific pair stands out the two electrodes are labelled as erroneous.

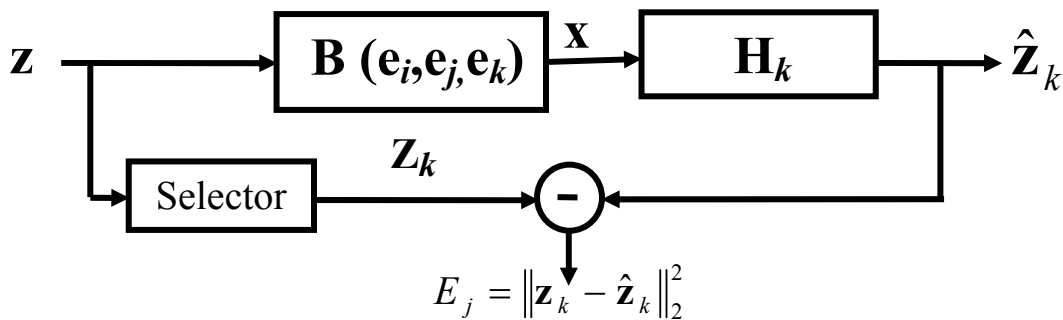


Figure 6.2 Estimation error scheme for two erroneous electrodes

In the event that no conclusive result is obtained, the method should continue the search for the possibility of three or more erroneous electrodes. Obviously, as the number of possible erroneous electrodes increases the percentage of data available for cross-validation decreases. In addition, the total execution time is extended significantly, rendering the method ineffective.

```

Define set  $S = \{(e_i, e_j) \mid i = 1 \dots N \text{ and } j = 1 \dots N, j \neq i\}$ 

For all  $(e_i, e_j)$  in  $S$ 
    Define set,  $S'$ , without electrode  $(e_i, e_j)$ :  $S' = \{e_k : k = 1 \dots N, k \neq i, k \neq j\}$ 
    For all  $e_k$  in  $S'$ 
        Calculate image:  $\hat{\mathbf{x}} = \mathbf{B}(e_i, e_j, e_k)\mathbf{z}$ 
        Estimate measurements on  $e_k$ :  $\hat{\mathbf{z}}_k = \mathbf{H}_k \hat{\mathbf{x}}$ 
        Calculate:  $E_k = \|\mathbf{z}_k - \hat{\mathbf{z}}_k\|_2^2$ 

    Calculate:  $T_{i,j} = \sum_{k=1, k \neq i, k \neq j}^N E_k$ 

    If  $T_{i,j}$  is less than other values of  $T$ , detect  $(e_i, e_j)$  as erroneous electrodes
  
```

Figure 6.3 Pseudo code for detection of two erroneous electrodes.

The pseudo code shown in Figure 6.3 is implemented using Matlab. The computation time for each T value is significantly longer due to the total number of electrodes and the increase in the number of $\mathbf{B}(e_i, e_j, e_k)$ matrices to pre calculated. Data used to validate the method and the subsequent result are covered in the sections to follow.

6.3 Data

Data used for validation of multiple erroneous electrodes are data acquired by Adler *et al* (1997) from ventilated dogs. This data set was used to validate the detection for single erroneous electrode. We have demonstrated in chapter 4 that the single erroneous electrode detection method is capable of detecting erroneous electrodes but at a much reduced sensitivity. To validate the results for two erroneous electrodes, we select data sets that have been shown to have multiple erroneous electrodes.

Simulated data are used to validate the PER threshold for detection. The amount of noise used is regulated by `awgn` function of Matlab. Since the signal level is very low, the `awgn` calculates the power of signal so as to not completely dominate the very low signal that are measured with electrode far away from the injection pair.

6.4 Result

Tests were carried out on both simulated erroneous data and real erroneous data. The test procedures are similar to the ones for single erroneous electrode detection.

6.4.1 Simulated Erroneous Data

Before testing on real multiple erroneous electrodes, tests were performed using simulated erroneous data. Similar to the procedure followed in chapter 4, we select erroneous electrode pairs and add either the same or a different level of white Gaussian noise to all data from those pairs. As expected, the reconstructed image with added noise to a pair of electrodes shows artefacts.

To demonstrate the effectiveness of the method we added -10dB of noise to electrodes 0 and 15; where the corresponding T values are shown in Figure 6.4(a) for all pairs involving electrode 0 and Figure 6.4(b) for all pair involving electrode 5. Comparing Figure 6.4(a) and Figure 6.4(b) we can see that the overall T value is much less when one of the erroneous electrode is removed. We can see that the combination involving electrode 5 has the lowest value at pair [0,5]. Therefore, when either one of the erroneous electrodes are removed the T value is significantly lower than when none are removed,

however it is not as low as when both erroneous electrodes are removed. The lowest value out of all possible combinations is with pair $[0, 15]$, where the white Gaussian noise was added, see Figure 6.4(a).

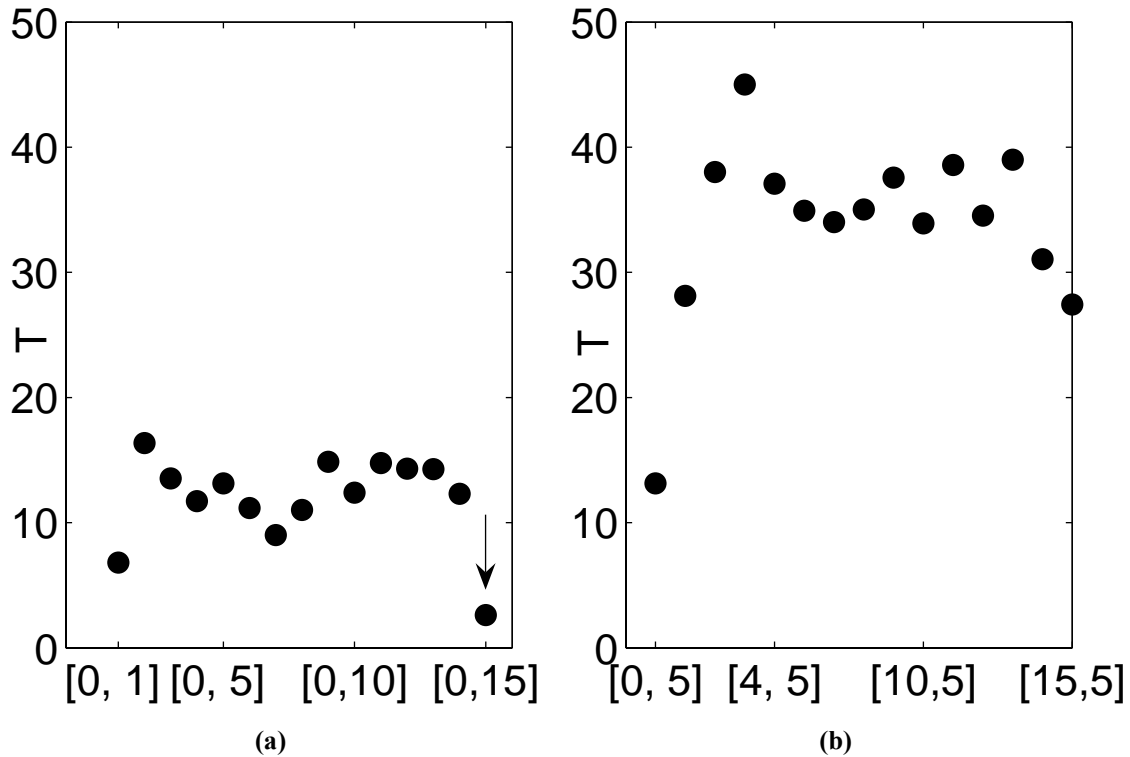


Figure 6.4 Detection of two erroneous electrodes using simulated noise of -10dB: (a) T values for all pairs involving electrode 0 (b) T Value for all pairs involving electrode 5

6.4.2 Erroneous experimental data

As demonstrated in Figure 6.1, some of the real data acquired from ventilated dogs do have multiple erroneous electrodes. These data sets are used to carry out detection of two electrodes. Applying the method for detection of two erroneous electrodes to the data set for Figure 4.13 (a), the T values of non-erroneous electrode pairs are very high compared to pairs that have either one or two erroneous electrodes. Interestingly, electrode 14 which did not exhibit erroneous electrode behaviour with the single electrode detector is erroneous electrode along with 4, 5, and 13. Additionally, electrode 12 is detected to be erroneous electrode by the single erroneous electrode detector is not detected here. However, the electrode pair $[12,13]$ does provide one of the lowest T values out of all possible pairs.

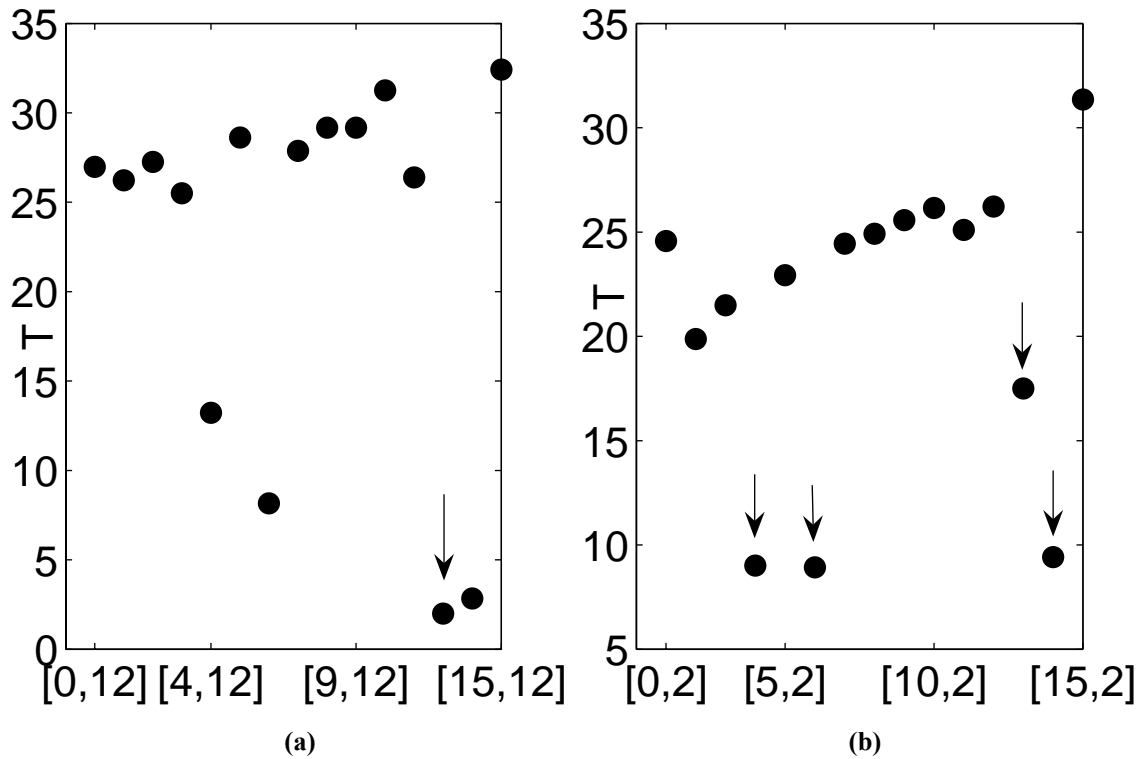


Figure 6.5: *T* graph for two erroneous electrode detection: (a) A low *T* value when both electrode 12 and 13 are removed. (b) *T* values when a non-erroneous electrode 2 is removed. Note the low *T* values for electrodes that are erroneous.

The data set explored in Figure 6.5 is by no means a benchmark for two erroneous electrodes detection. As we have explained previously, the data set was acquired from a dog with some skin conditions which may have caused numerous electrodes to register faulty measurements. For a more representative data, we have selected a different data set from a separate experiment on another ventilated dog. Applying the single electrode detection method, the electrodes 13 and 14 are shown to be erroneous, see Figure 6.6. In addition, electrode 4, 6 and 15 do have a certain degree of error to their measurements.

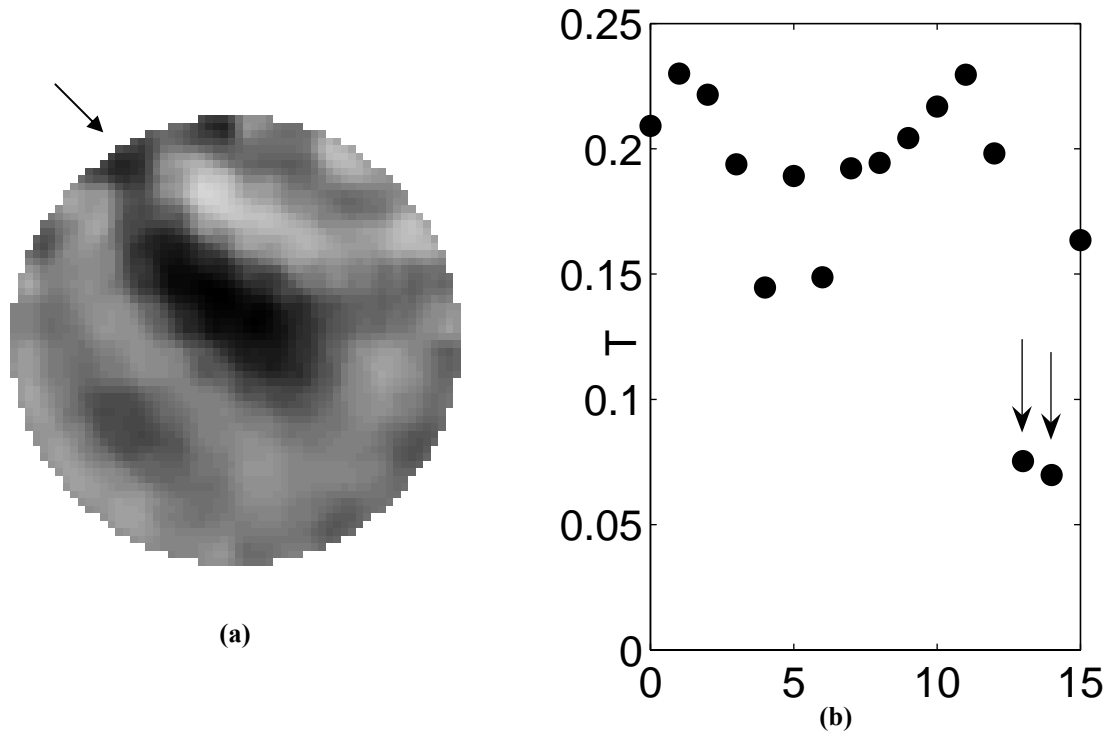


Figure 6.6 Single electrode detection method applied to data with two erroneous electrodes

To verify this finding the same data set was applied using two electrode detection method. We have shown results for pairs involving 10, 11, 13 and 14. According to the single electrode detection method, electrodes 10 and 11 are non-erroneous. The result for two erroneous detection method also shows that these two electrodes do have a higher overall T value when paired with other electrodes other than electrode 14. Examining the result for pairings involving electrode 13, we can see that electrode 13 does have a similar overall T value to electrodes 10, and 11. However, the smallest possible T value occurs when electrode 13 is paired up with 14. T value for all pairs involving electrode 14 is much smaller than T values involving electrodes 10, 11 or 13, which suggests that electrode 14 is the most dominant erroneous electrode. We do not have a good explanation for the T value for [1, 14] pair and a low T value for [15, 14].

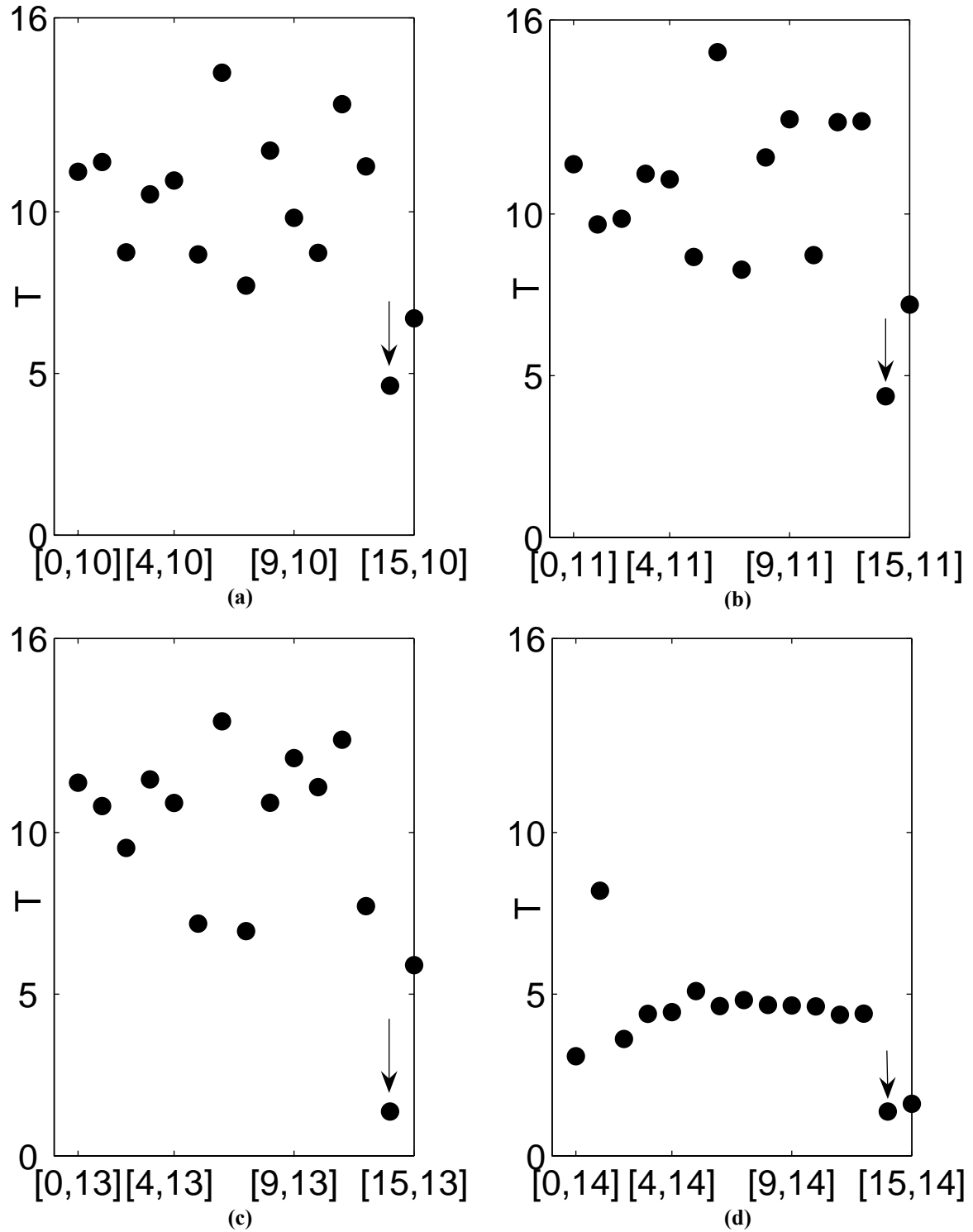


Figure 6.7 Two electrode detection method: (a) pairs involving non-erroneous electrode 10 (b) pairs involving non-erroneous electrode 11 (c) pairs involving erroneous electrode 13 (d) pairs involving erroneous electrode 14

6.5 Discussion

In this chapter, the estimation scheme of chapter 4 is expanded to detect two erroneous electrodes. The modified version of the estimation method removes a pair of electrodes and estimates a third independent electrode. The sensitivity matrix is reconstructed without contributions from the three eliminated electrodes. In a 16 electrode system using adjacent measurement pattern, a total of 208 data points are available; when three of the electrodes out of 16 are removed only 176 data points remain. Hence, the prediction of data from 84% of the remaining is valid. However, we need to be careful while extending this method for more than two erroneous electrodes. Analysis of prediction accuracy vs. percentage of remaining data with different measurement patterns needs to be carried out.

Detection of two erroneous electrodes with simulated erroneous data is clearly demonstrated in Figure 6.4 (a) and (b). The T value for both electrode 0 and 15 is much less than all other possible pairs. Even though both electrodes have the same amount of Gaussian noise, results from Figure 6.4 (b) suggest that removing electrode 0 with electrode 5 provide much lower T value rather than electrode 15 with electrode 5. The result suggests certain electrode position dependence on the estimation scheme. This dependence needs to be analyzed through a controlled experiment that we are not able to carry out at this time.

In applying the method to real data, results were somewhat unclear for the data acquired from a ventilated dog with a skin condition. The single electrode detection method result shown in Figure 4.13 (a) suggests the existence of more than two erroneous electrodes. The result of Figure 6.5 also suggests the data set contains more than two erroneous electrodes. Several pairs have significantly lower T value; especially ones that involve all electrodes that had low T value in single electrode detection method (Figure 4.13).

In analyzing another set of data classified as having multiple erroneous electrodes, we noticed a result more in agreement with the prediction of the single erroneous detection method. The electrode pair [13, 14] has the lowest T value. Figure 6.7 shows electrode 14

is much more erroneous than any of the other electrodes, since the overall T value is much less. Electrode pair [15, 14] has T value much less than expected.

The results from real data of multiple electrode error detection suggest that the problem is much more complex than with single electrode detection. The robustness of the method depends on the total number of independent voltage measurements that are available, the electrode layout, and the measurement pair applied. Nevertheless, we have shown that it is possible to detect two erroneous electrodes using the same mathematical framework as in Chapter 4.

On the 16 electrode system, two erroneous electrodes detection method has a total of 120 pairs. For each individual pair we pre-calculate equation (4.8) in order speed up the execution time. The calculation of each T value for a pair takes approximately 1s, and overall one data set takes approximately 2 minutes on 1.8GHz Athlon processor. The approach is not suitable for real time processing in its current state.

Chapter 7

Conclusion

The objective of this thesis was to provide a systematic and robust detection method for erroneous electrode data in EIT. The idea of cross validating electrode measurements based on the remaining electrode data was applied. The method was applied to 2D and 3D EIT on simulated and experimental data. Results from simulated data suggest the method can consistently detect erroneous electrodes with SNR below 10dB additive Gaussian noise in both 3D and 2D EIT. For detection of a single erroneous electrode in 2D EIT, we have demonstrated that the method achieves the same PER detection threshold of -22dB for both opposite and adjacent drive pattern (Figure 4.12). In 3D EIT, the detection method was tested exclusively on simulated data. The results we observe (Figure 5.3) are similar to the 2D EIT even though we may have committed the inverse crime as defined Wirgin (2004).

Results based on experimental data for 2D EIT show consistent detection results as classified by the expert users. As we have demonstrated in Figure 4.11, a 0dB noise level has little perceptual impact on the reconstructed image. Analyzing the results based on experimental data, we encountered data sets with multiple erroneous electrodes. The single electrode detection method was able to detect the electrodes at a reduced sensitivity for several of the data sets (Figure 4.13).

Encountering multiple erroneous electrodes prompted us to look at ways of extending the single erroneous electrode detection method into multiple erroneous electrode detection. The approach for extension of the original method was through cross validation of data from the remaining electrodes after removing all electrodes suspected to have been

erroneous. The method was applied to the same experimental data used in single erroneous electrode detection and simulated data. Tests for the case of detecting a pair of erroneous electrodes in simulated data provided accurate results (Figure 6.4). Experimental data provided mixed results depending on the number of erroneous electrodes present in the data set as determined by the single erroneous detection method (Figure 6.5). Nevertheless, data sets shown to have only two erroneous electrodes gave accurate results when applied to two erroneous electrodes detection method (Figure 6.6 and Figure 6.7).

The method in general shows an interesting potential for use in EIT clinical and experimental applications. In real-time application it would be possible for single electrode error detection method through increases in computing power or parallel processing. Currently, single electrode detection requires 74s pre-calculation and 3s for each data set. For 3D EIT and multiple erroneous electrode detection, the application of the method becomes cumbersome in its current form due to the increase number of electrodes for 3D EIT and increase in possible pairs in multiple erroneous electrodes detection. Even so, the performance results for both 3D EIT and multiple erroneous electrodes detection are in line single erroneous electrode detection.

Future Work

Detection of erroneous electrodes in EIT is an important aspect to making the technology viable for clinical use; this thesis has contributed the possibility of detection of single or multiple erroneous electrodes. The methods were applied under the premise of all noise characteristics is Gaussian, similar to the probability distribution function of the conductivity distributions. However, we have shown in section 3.3 that the noise has a variety of sources and characteristics, especially being non-stationary. Further understanding and modelling of these noise characteristics would improve the ability of the detection algorithm. For example, error propagation due to an erroneous electrode used for current injection is far greater than when that same electrode is used for voltage measurement. Careful study of this fact and its impact on detection of erroneous

electrodes needs to be studied. Hence, distinguishing between the noise characteristics when an electrode is used for measurement and when it is used for injection would allow us to modify the detection scheme. Study of the noise characteristics could be done through analysis of the impact of electrode type, reusability, and skin-electrode interaction.

Apart from modelling of electrode error and exploiting the knowledge for detection, the impact of removing electrodes positioned near regions of high conductivity change has to be carefully looked at. These electrodes represent the majority of the information and removing them leaves only electrodes with the least amount of inter-dependence. Thus, it is necessary to investigate the accuracy of the voltage difference estimation for electrodes that carry a higher percentage of the change in conductivity. If indeed there is significant dependence, equation (4.8) can be modified by introducing a weight factor to account for the bias of the estimator.

For multiple erroneous electrode detection the estimation scheme removes certain percentage of data and image estimation is then made with the remaining data. Intuitively, we can guess that as the number of erroneous electrodes increases detection using multiple erroneous electrodes will become more difficult. Hence, a study of the limits for the multiple erroneous electrodes needs to be investigated. One drawback of a multiple erroneous electrode detection method is the amount of time it takes to do the computation. The computation time can be reduced using a more powerful computer and/or through parallel processing. Still this solution may not be suitable for a real time application which is one of the methods' intended use. Hence, a more compact method such as Jackknife method (Efron, 1982) is worth exploring (see Appendix 1). The Jackknife method, cross validates certain statistical characteristics of a data set (in our case statistical characteristics of individual electrodes), such as the mean or standard deviation rather than cross-validating the actual data. To be able to apply this method, a statistical parameter that reflects the presence of an erroneous electrode needs to be identified.

The current detection method is applied on a single difference measurement based on two data sets at two time instances. However, sources of error such as detached electrode and sweat are major contributors, which are dependent on time. It may be possible to carry out time based detection method that incorporates our approach. Preliminary analysis of estimation error vs. time shown in Appendix 2 demonstrates that the estimation error does change over time.

Application of this method to verify the goodness of data is not constrained to EIT but may also be used to for other multi-sensor systems. However, it can only be applied if there is certain inter-dependence of data from different sensors. Therefore for systems such as Positron Emission Tomography (PET), it is necessary to first prove that data from one sensor can be cross-validated based on data from other sensors. Furthermore, it is essential to justify the need for a detection scheme by showing that the failure of a sensor or sensors affects the overall performance of the system. If a system fulfills the above two criteria the method can be applied and its detection threshold can be determined.

Bibliography

Adler A (2004) Accounting for erroneous electrode data in Electrical Impedance Tomography *Physiol. Meas.* **25** 227-238

Adler A, Amyot R, Guardo R, Bates J H T and Berthiaume Y (1997) Monitoring changes in lung air and liquid volumes with electrical impedance tomography *J. Appl. Physiol.* **83** 1762-1767

Adler A and Guardo R (1996) Electrical Impedance Tomography: Regularised imaging and Contrast Detection, *IEEE Trans. Medical Imag.* **15** 170-179

Adler A (1995) Measurement of pulmonary function with Electrical Impedance Tomography *Université de Montreal: Institut de genie biomédical école polytechnique de montréal*

Al-Hatib F (1998) Patient-instrument connection errors in bioelectrical impedance measurement, *Physiol. Meas.*, **19** 285-296

Asfaw Y and Adler A (2005) Automatic detection of detached and erroneous electrodes in Electrical Impedance Tomography, *Physiol. Meas.*, Accepted for publication

Barber D C and Brown B H (1985) Recent Developments in Applied Potential Tomography – APT , *Information Processing in Medical Imaging*, 106-21.

Barber D C and Brown B H (1988) Errors In Reconstruction of Resistivity Images Using a Linear Reconstruction Technique, ", *Clin. Phys. Physiol. Meas.*, **9** (A), 101-104.

Barber D C and Brown B H (1987) Fast reconstruction of resistance images, *Clin. Phys. Physiol. Mes.*, **8** (A), 47-54.

Blott B H, Daniell G J and Meeson S (1998) Electrical impedance tomography with compensation for electrode positioning variations *Phys. Med. Biol.* **43** 1731-1739

Borsic A (2002) Regularisation Methods for Imaging from Electrical Measurements *Phd Thesis, Oxford Brookes University*

Booth M J and Basarab-Horwath I (1996) Comparing electrode configurations for electrical impedance tomography, *IEEE Electronics Letters*, **7** 648-649

Cheng K, Isaacson D, Newell J C, and Gisser D G (1989) Electrode models for electric current computed tomography *IEEE Transactions on Biomedical Engineering* **36** 918 – 924

Church P, Wort P, Gagnon S and McFee J E (2001) Performance assessment of an electrical impedance tomography detector for mine-like objects. *Proc. SPIE Conference on Detection and Remediation Technologies for Mines and Mine-like Targets VI.* **4394** 16-20

Dalziel C F (1956) Effect of electric shock on man *IRE Trans. Med. Electron.* **5** 44-62.

Efron B (1982) The Jackknife, The Bootstrap and Other Resampling Plans *Society for Industrial and Applied Mathematics* **38** 49-59

Eyüboğlu B M (1996) An interleaved drive electrical impedance tomography image reconstruction algorithm *Physiol. Meas.* **17** A59–A71

Frangi A R, Riu P J, Rosell J, and Viergever M A (2002) Propagation of measurement noise through backprojection reconstruction in electrical impedance tomography *IEEE Trans. on Medical Imaging* **21** 566 - 578

Geddes L A, and Baker L E (1971) Response to the passage of electric current through the body, *J. Assoc. Adv. Med. Instrum.* **5** 13-18.

Gholam-Hosseini H, Nazerun H and Reynolds K J (1998) ECG Noise Cancellation Using Digital Filters, *2nd International Conference on Bioelectromagnetism*, 151-152

Gritzali F, Frangakis G, and Papakonstantinou G (1988) Detection of the P and T waves in an ECG, *Comput. Biomed. Res.* **22** 83-91

Hansen P C (1998) Rank-Deficient and Discrete Ill-Posed Problems: Numerical Aspects of Linear Inversion, *SIAM Pub.*

Herrera R E, Sun M, Charles P J, Dahl R E, Ryan N D, and Sciabassi R J (2000) Removal of non-white noise from single trial event-related EEG signals using soft-thresholding *Proc. IEEE Eng. in Med. and Bio. Society* **1** 793 - 795

Hu M-Q, Hua P and Webster J (1987) Measurement error in an electrical impedance tomography system *Proc. 9th Int. Conf. IEEE Eng. Med. Biol. Soc.* 1425-6

Hua P, Woo E J, and Webster J G (1993) Using Compound Electrodes in Electrical Impedance Tomography *IEEE Trans. on Biomed. Eng.* 40 29-34

Huebner K H (1974) The Finite Element Method for Engineers. *John Wiley & Sons*, New York

Khosla D, Don M, and Kwong B (1999) Spatial mislocalization of EEG electrodes – effects on accuracy of dipole estimation *Clinical Neurophysiology* **110** 261-271

Kolehmainen V, Vauhkonen M, Karjalainen P M and Kaipio J P (1997) Assessment of Errors in Static Electrical Tomography with Adjacent and Trigonometric Current Patterns *Physiol. Meas.* 18 289-303

Korjnevsky A V, Kornienko V N, Kul'tiasov M Y, Kul'tiasov Y S, and Cherepenin M (1997) Electrical Impedance Computerized Tomograph for Medical Applications *Instruments and Experimental Techniques* **40** 415-421

Kreyszig (1983) Erwin Advanced Engineering Mathematics *John wiley & sons* 5^{ed}
Ksienski D A 1992 A Minimum Profile Uniform Current Density Electrode, *IEEE Trans. on Biomed. Eng.* **39**, 682-692

Kun S and Peura R A (1995) Influence Of The Electrode Configuration On The Results Of Electrophysiological Studies *IEEE-EMBC and CMBEC* 1551-1552

Leksell L G (1991) Measurement of extravascular lung water- methods and clinical implications *Acta. Anaesthesiol. Scand.*, **35** 81-86

Lionheart B (1997) Conformal uniqueness results in anisotropic electrical impedance imaging *Inverse Problems* **13** 25–134.

Lionheart B (2004) EIT reconstruction algorithms: pitfalls, challenges and recent developments *Physiol. Meas.* **25** 125–142

Lozano A, Rosell J and Pallás-Areny R (1995) Errors in prolonged electrical impedance measurements due to electrode repositioning and postural changes *Physiol. Meas.* **16** 121-130

Luo S, Afonso V X, Webster J G, and Tompkins W J (1992) The Electrode System In Impedance Based Ventilation Measurement *IEEE Trans. On Biomed. Eng.* **39**, 1130-1141

Meeson S, Blott B, and Killingback A (1996) EIT data noise evaluation in the clinical environment *Physiol. Meas.* **17**(suppl.) A33-A38

(1998) Montreal Neurological Institute, Electricity on the BRAIN. Retrieved November 7, 2004 from <http://www.mni.mcgill.ca/nm/1998s/en/EEG.html>

Ollikainen J O, Vauhkonen M, Karjalainen P A, and Kaipio J A (2000) Effects of electrode properties on EEG measurements and a related inverse problem *Medical Eng. & Physics* **22** 535–545

Oostendorp T and Oosterom A V (1991) The Potential Distribution Generated By Surface Electrodes In Inhomogeneous Volume Conductor Of Arbitrary Shape *IEEE Trans. on Biomed. Eng.* **38** 409-417

Ortolan R L, Mori R N, Pereira R R, Cabral C M N, Pereira J C, and Cliquet A (2003) Evaluation of nonadaptive filtering and wavelet transform techniques for noise reduction in EMG mobile acquisition equipment *IEEE Trans. on Rehab. Eng.* **11** 60-69

Ouyang G, Li C, and Jiang G (2001) A distinguishing method of epileptic EEG and deglutition EEG based on chaotic noise-reduction *IEEE Eng. in Med. and Bio. Society* **1** 647-650

Palaniappan R, Anandan S and Raveendran P (2002) Two Level PCA To Reduce Noise and EEG From Evoked Potential Signals 7th Inter. Conf. on Control, Automation, Robotics and Vision 3 1688-1693

Patriciu K, DeMonte T P, Joy M and Struijk J J (2001) Investigation Of Current Densities Produced By Surface Electrodes Using Finite Element Modeling And Current Density Imaging *Proc. of the 23rd Ann. EMBS Inter. Conf.* 2403-2406

Patriciu K, Yoshida K, DeMonte T P and Joy M (2001) Detecting Skin Burns Induced By Surface Electrodes *Proceedings of the 23rd Annual EMBS Inter. Conf.* 3129-3131

Patterson R P and Lockwood J S (1993) The Influence of Electrode Size and Type on Surface Stimulation of the Quadriceps *IEEE Trans. on Rehab. Eng.* **1** 59-62

Perz S and Kufner R (1995) Estimation of Noise Effects on Computerized ECG Analysis: A new Approach *Computers in Cardiology* 389-392

Ramos J and Pallas-Areny Y (1996) ECG Noise Reduction by Ordered Averaging Bridging Disciplines for Biomedicine. *Proc. of 18th Ann. Inter. Conf. of the IEEE Eng. in Medicine and Biology Society* **3** 960-961

Sansen W, Geeraerts B, Van Petegem W, Dehaene W, and Steyaert M (1992) Voltage versus current driven high frequency EIT systems *Proc. of 1992 Inter. Biomed. Eng.* 102-106

Seitsonen E, Yli-Hankala A, and Korttila K (2000) Are electrocardiogram electrodes acceptable for electroencephalogram bispectral index monitoring? *Acta Anaesthesiologica Scandinavica* **44** 1266

Tungjitkusolmun S, Woo E J, Cao H, Tsai J, Vorperian V R, and Webster J G (2000) Finite Element Analysis of Uniform Current Density Electrodes for Radio-Frequency Cardiac Ablation *IEEE Trans. on Biomed. Eng.* **47** 32-40

Wang Y and Gotman J (2001) The influence of electrode location errors on EEG dipole source localization with a realistic head model *Clinical Neurophysiology* **112** 1777-1780

Waugaman W A and Schrader C B (1994) Optimal Current Model from Surface Electrodes *Proceedings of the 33rd Conference on Decision and Control* **4** 4112-4113

Williams R J, Leung H L, and Griffiths H (1992) Electrical Impedance Tomography. The role of computer aided engineering *IEE Colloquium on Medical Imaging: Image processing and Analysis* 6/1-6/3

Wirgn A (2004) The Inverse Crime Retrieved November 25, 2004 from
<http://hal.ccsd.cnrs.fr/docs/00/00/10/84/PDF/invercim.pdf>

Wright J J and Kydd R R (1992) The electroencephalogram and cortical neural networks
IOP Network: Comput. Neural Syst **3** 341-362

Yacoub S, Gumery P Y, and Raoof K (1994) A novel signal processing method for multi-electrode surface electromyography *Proceedings of the 16th Annual Inter. Conf. of the IEEE Eng. in Medicine and Biology Society* **2** 1336-1337

Yorkey T J, Webster J G, and Tompkins W J (1987) Comparing Reconstruction Algorithms for Electrical Impedance Tomography *IEEE Trans. on Biomed. Eng.* **34**, 843-852.

Appendix 1: Using Jackknife method for detection

We have introduced a detection method that uses the cross-validation concept (Efron, 1982). The drawback to this approach is the amount of time required to complete the cross validation. Another approach is known as the Jackknife estimate, where some statistical characteristic is cross validated instead of the actual data points. Hence assuming a set of electrodes, S , we compute some statistics of interest (θ) such as the mean. The Jackknife method is based on sequentially deleting an element from S and re-computing the statistics of interest. Efron (1982) has shown that the recomputed statistical characteristic is averaged and it is used to calculate the bias from the overall statistical characteristics:

$$BIAS = (n-1)(\hat{\theta}_{(.)} - \hat{\theta}) \quad (10.1)$$

Where $\hat{\theta}_{(.)}$ the mean of the statistic of interest is calculated by eliminating each element of S and $\hat{\theta}$ is the overall estimate. The bias corrected jackknife estimate of θ is

$$\tilde{\theta} = n\hat{\theta} - (n-1)\hat{\theta}_{(.)} \quad (10.2)$$

The Jackknife statistics can be potentially exploited for detection of erroneous electrode considering that the data from an erroneous electrode is different in magnitude. For example, if we calculate the mean of the data for the each electrode the erroneous electrode will have a higher value than non-erroneous ones. However, simple statistical characteristic such as the mean is not reliable unless the noise is considerably high. Figure A1.2 shows the difference in average magnitude of difference voltage measurements per electrode when Gaussian noise of -10 dB, -5 dB and 0 dB is added to electrode 5. The average magnitude of electrode 5 has much higher value than the rest of the data points at -10 dB and -5 dB but it becomes increasingly difficult to distinguish as the noise decreases. With careful modelling of error and knowledge of the noise characteristics it would be possible to detect erroneous electrodes.

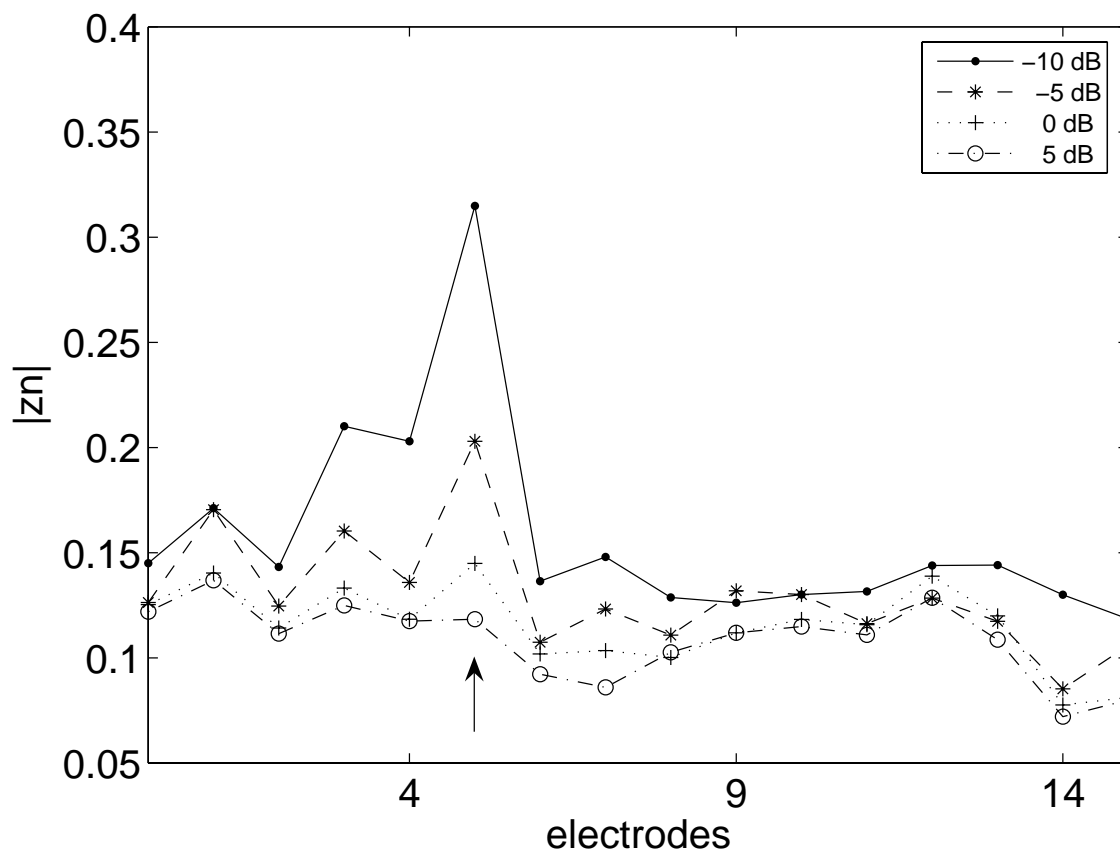


Figure A1.2 Detection using the Jackknife method: electrode 5 is erroneous

Appendix 2: Analysis of Electrode error with time

In this section, we offer analysis of a specific experimental data and the estimation error of a certain candidate electrodes. The graph shows the change in estimation error for 4 electrodes within a data set over a period of one hour and ten minutes. This particular data set has no erroneous electrodes. A reference data of similar ventilation and instillation was selected for each session of the experiment. The result shows a gradual increase of the estimation error which is consistent with the understanding that electrode error increases with time. The drop in estimation error takes place just after 45 minutes during the instillation procedure, which may have caused electrode movement. The estimation error decreases after the instillation procedure and gradually starts to increase. It is interesting to note that all the electrodes exhibit the same pattern of estimation error, suggesting that the cause for error is of the global nature and is not confined to a specific electrode.

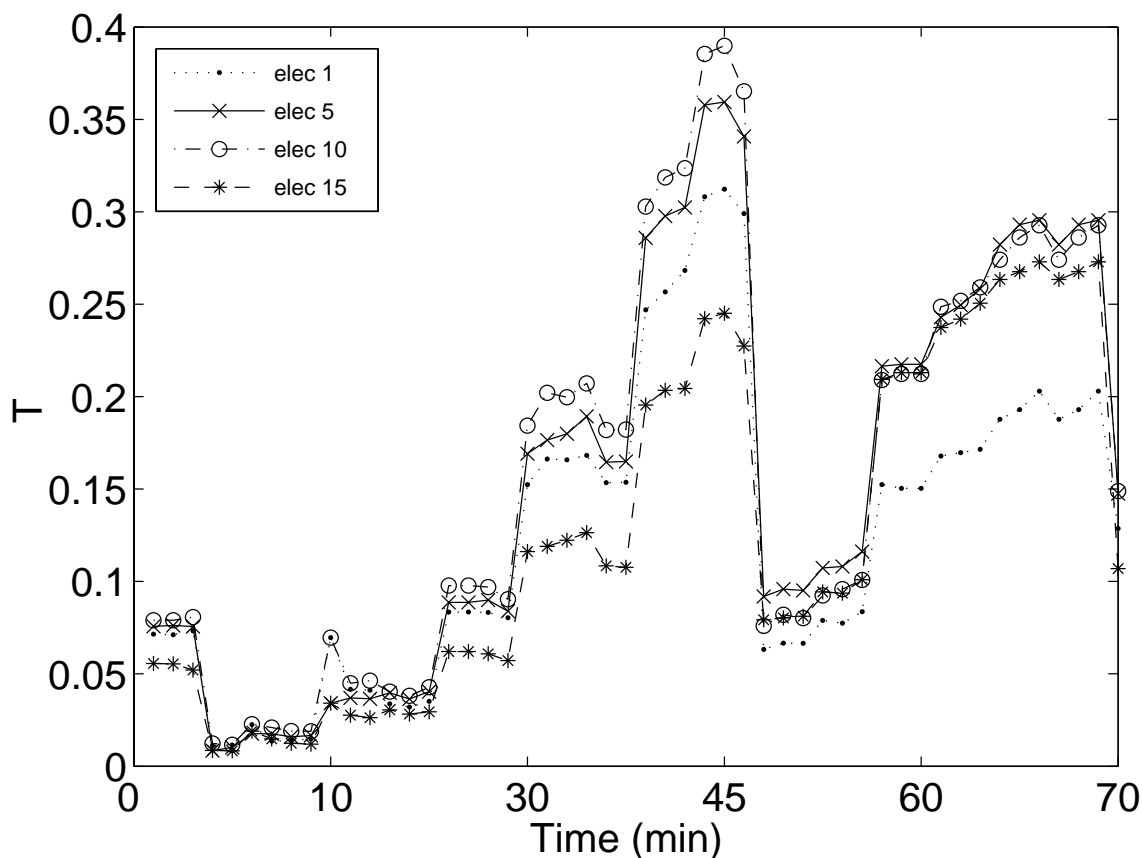


Figure A2.2 Average change of estimation error with time for electrodes 1, 5, 15, 10

Appendix 3: 2D erroneous electrode detection code

Appendix 3 lists the Matlab code used for detection of erroneous electrode in 2D EIT. The main function is `elec_detect` which implements the method described in chapter 4. In addition, the values in equation (4.8) are calculated only once using the function `prep_predictor`. The function `add_noise` is used to add simulated noise to a particular electrode's data.

```
function [err,PER]=elec_detect(e,vi,ve,repeat,snr1,elec)
% ELEC_Detect: runs the erroneous electrode detection method on selected
% samples data from ventilated dog data of 1994. User must select the data
% set. The result shows the graph of the estimation for each electrode. The
% electrode with the lowest total erms is assumed to be the erroneous
% electrode
%
% e:      Experimental data number
% vi:     Measurement during inspiration or at time t1
% ve:     Measurement during expiration or at time t2, where t2>t1
% repeat: Number of times to repeat experiment
% snr1:   Signal to noise ratio specifying the noise to be added if any
% elec:   Noise is added to data from elec, elec=-2 if there is no noise
%         to be added
% err:    estimation error for each electrode in the EIT system
% PER:    Prediction error of experimental data e or if simulation PER for
%         different snr values for each iteration
%
% (C) 2004 Yednek Asfaw
% $Id: elec_detect.m,v 1.3 2004/11/03 22:57:01 yasfaw Exp $

%clear all;
DEBUGM=0;
%constructor is the set matrices generated by prep_predictor.m
load constructor

%index of all valid measurements
global ELS
n=1;
for r=1:repeat
    k=1;
    for snr=snr1
        j=1;

        %calculate the voltage difference
        if (e==59 | e==60 | e==61)
            z=(vi(:,1) - ve(:,1)); %simulated data already normalized
        else
            z=(vi(:,1) - ve(:,1))./(0.5*(vi(:,1)+ve(:,1)));
        end

        %add noise to data from elec, if none elec=-2
        zn=add_noise(elec,z,snr);

        if DEBUGM==1

            %show the amplitude of voltage difference for each pair
            %without noise
```

```

figure,plot(z(ELS),'.')
xlabel('Index for measurement and injection pair');
ylabel('amplitude of the voltage difference');

%with noise
figure,plot(zn(ELS),'.')
xlabel('Index for measurement and injection pair');
ylabel('amplitude of the voltage difference');

%calculate the conductivity distribution
exp_image=imgr(irec(-zn,zeros(256,1),'filt',2));
filename=['e', num2str(e),'.png'];
cmap=[flipud(fliplr(hot(33)));hot(33);1,1,1];cmap(33,:)=[];
colormap(cmap)

%save the reconstructed image into png format
imwrite(exp_image,cmap,filename); %bmpwrite
image(exp_image);
figure,mesh(exp_image); pause;
end

%start the detection method
for remapped=zn %for each individual data set
for i=1:16 %select a candidate electrode ei
err(i)=0; %initialize the total erms
for j=1:16 %select an electrode ej different from ei
if i~=j;
%determine the estimation error
err(i)=err(i)+ remapped'*IM{i,j}*remapped;
end
end
err(i)=err(i)/15; %normalize

if DEBUGM==1
disp([i, err(i)]); %show estimation error for each ei
end
end

j=j+1;
if DEBUGM==1
std_err=std(err);
mean_err=mean(err);
erf_val=( mean_err- min(err))/ std_err;
erf_array=(mean_err-err)/std_err;
z=1-erf(erf_val);
z_array=1-erf(erf_array);
fprintf('estimation accuracy is %d\n',z);
end
end
if (DEBUGM==1) %T vs. electrode ei
figure,plot(0:15,err,'*')
axis([-1 16 0 0.04])
xlabel('electrode #')
ylabel('T_e_r_m_s');
end

%determine if there is an erroneous electrode in this data set
norm_sample=(err-mean(err))/var(err);
%calculate the distance of each T value for electrode ei from the
%other T values
for i=1:16
if norm_sample(i)>=0 val=0; else val=norm_sample(i); end
dist(i)=sum(abs(norm_sample-val));

```

```

end

%determine the min to max distance ratio and PER
maxdist_ratio(n,k)=min(dist)/max(dist);
PER(n,k)=20*log(maxdist_ratio(n,k));

disp([r snr e maxdist_ratio(n,k) 20*log(maxdist_ratio(n,k))]);
k=k+1;
end
n=n+1;
end

```

```

function innerM=prep_predictor(dpos,dvv,j,elec)
% prep_predictor: calculates the overall matrix of equation 4.9
% dpos: The difference between first pair ie. [0 2] injection pair-> dpos:2
% dvv: Sensitivity matrix (H)
% j: Electrode ej for which data is to be estimated
% elec: Pre_removed electrodes (use [] for none)
%
% (C) 2004 Yednek Asfaw
% $Id: prep_predictor.m,v 1.1 2004/11/03 23:03:43 yasfaw Exp $

%Prepare the index of data that is already removed (els), eg. data of electrode
%ei for single erroneous electrode estimation
els=rem(rem(0:255,16)-floor((0:255)/16)+16,16)';
els=~any(rem([15 16 [15 16]+dpos] ,16)' ...
*ones(1,256)==ones(4,1)*els)';
els= reshape(els,16,16);
for i=1:length(elec)
    ee=elec(i)+16;
    els(rem(ee,16)+1,:)=zeros(1,16);
    els(rem(ee-1,16)+1,:)=zeros(1,16);
    els(:,rem(ee,16)+1)=zeros(16,1);
    els(:,rem(ee-dpos,16)+1)=zeros(16,1);
end %for i
els_preremoved= els(:);

global ELS E;

ELS= els_preremoved;
%remove data of electrode ej
kill_el(j);

%isolate the data from electrode ej
el_data= els_preremoved & (~ELS);

%prepare equation 4.9
S=diag(double(el_data)); %selector
I=diag(ones(1,256)); %identity matrix
prog='mkfilt'; param=[1 0 .1 0];

%recalculate the reconstruction matrix
B=feval(prog,param(1:3));
B_full=zeros(256);
B_full(:,ELS)=B;

%calculate matrix the estimation error for pair ei and ej
innerM= ((I'-B_full'*dvv)*S')*(S*(I-dvv*B_full));

```

```

function zn=add_noise(elec,z,snr)
% add_noise: introduces gaussian to the data related to electrode elec
% elec: Gaussian noise is added to data that comes from elec
% z:    Original Difference measurement
% snr:  The signal to noise ratio snr=20*log(signal power/noise power)
%
% (C) 2004 Yednek Asfaw
% $Id: add_noise.m,v 1.2 2004/11/03 22:58:04 yasfaw Exp $

if(elec>=0)
    global ELS ChoiX

    %find out the configuration
    dpos= rem(16+ChoiX(3:4)*[-1;1] + (ChoiX(3:4)>='a')*[1;-1] ...
        *('0a'*[-1;1]-10),16);

    %find the index of data related to elec
    els= reshape(ELS,16,16);
    for i=1:length(elec)
        ee=elec(i)+16;
        els(rem(ee,16)+1,:)=zeros(1,16);
        els(rem(ee-1,16)+1,:)=zeros(1,16);
        els(:,rem(ee,16)+1)=zeros(16,1);
        els(:,rem(ee-dpos,16)+1)=zeros(16,1);
    end %for i
    new_index=find((els(:) ~= ELS));

    %add noise, awgn needs to be in measured mode
    zn=z;
    zn(new_index) = awgn(z(new_index),snr,'measured');
else
    %no noise
    zn=z;
end

```

Appendix 4: 3D erroneous electrode detection code

Appendix 4 lists the Matlab code used for detection of erroneous electrode in 3D EIT. The main function is `elec_detect_3D` which implements the method described in chapter 4 and 5. The matrices $\mathbf{B}(e_i, e_j)$ are calculated by `err_jacobian` function after which the values are saved for future use. The function `awgn` is used to add simulated noise to a particular electrode's data.

```
function [err, PER]=elec_detect_3D ()

% ELEC_Detect_3D: runs the erroneous electrode detection method simulated
% data. The result shows the graph of the estimation for each electrode. The
% electrode with the lowest total erms is assumed to the erroneous
% electrode
%
% err:      estimation error for each electrode in the EIT system
% PER:      Prediction error of experimental data e or if simulation PER for
%           different snr values for each iteration
%
% (C) 2004 Yednek Asfaw
% $Id: elec_detect_3D.m,v 1.1 2004/11/05 14:00:00 yasfaw Exp $

%clear all;
errelec=input('Choose Erroneous electrode (1:32):');
disp(sprintf('\n'))

snr1=input('Noise level in dB to add to data from that electrode (-200:200):');
disp(sprintf('\n'))

rep=input('Number of times to repeat simulations (1:100):');
disp(sprintf('\n'))

%calculate the simulated difference measurements
%and the corresponding measurement pair
[dvaG, indH]=prep_elec_detect_3D;
dvaGn=dvaG;

%determine the index of data contributed by errelec
W=diag(Mod_Jacobian(errelec,indH));
err=zeros(32,1); %initialize the T values for each electrode
n=1;
for repeat=1:rep %repeat the simulation rep times
    k=1;
    for snr=snr1 %with a range of certain snr
        %add noise to data that comes errelec
        dvaGn(find(W==0)) = awgn(dvaG(find(W==0)), snr, 'measured');
        for i=1:32
            err(i)=0; %initialize the T value for ei
            for j=1:32 %for each electrode not including ei
                if(i~=j)
                    v=genvarname(['B', num2str(i), num2str(j)]);
                    v1=genvarname(['W', num2str(i), num2str(j)]);
                    eval(['load ', 'B', num2str(i), num2str(j)]);
                    eval(['load ', 'W', num2str(i), num2str(j)]);
                    %calculate the estimate
```

```

        Est_dva=eval([v '* dvaGn']);
        err(i)=err(i)+(norm(Est_dva(find(eval(v1)==0)) ...
            -dvaGn(find(eval(v1)==0))));
        eval(['clear ', 'B', num2str(i), num2str(j)]);
        eval(['clear ', 'W', num2str(i), num2str(j)]);
    end
end

end

%remove the added noise
dvaGn=dvaG;

%show the result of the estimation
figure,plot(1:32,err(:),'*');
title('T value for errenous electrode 1');
xlabel('electrodes');
ylabel('T value');

%determine if there is an error
norm_sample=(err-mean(err))/var(err);
for i=1:32
    if norm_sample(i)>=0 val=0; else val=norm_sample(i); end
    dist(i)=sum(abs(norm_sample-val));
end

ratiol(n,k)=min(dist)/max(dist);
PER(n,k)=20*log(ratiol(n,k));
format short e;
disp([repeat snr ratiol(n,k) PER(n,k)]);
save PER_3D PER;
k=k+1;
end
n=n+1;
end
return;

```

```

function err_jacobian ()
%err_Jacobian: This function is run once to calculate the modified
%jacobians for all possible pairs ei and ej. If the values exist for
%the particular setup this should not be executed
% (C) 2004 Yednek Asfaw
% $Id: err_jacobian.m,v 1.1 2004/11/06 9:00:00 yasfaw Exp $
[dvaG, indH, Reg, J]=prep_elec_detect_3D;

%add noise to data coming from electrode 1
W=diag(Mod_Jacobian(1,indH));
for i=1:32
    fprintf('%d',i);
    for j=1:32
        if(i~=j)
            W=Mod_Jacobian([i j],indH);
            JJ=W*J;
            v=genvarname(['B', num2str(i), num2str(j)]);
            eval([v '=J*((transpose(JJ)*JJ
                ...+tfac*transpose(Reg)*Reg)\transpose(JJ));']);
            cd Jacobians;
            eval(['save ', 'B', num2str(i), num2str(j), ' B' ...
                , num2str(i), num2str(j)]);
            cd ..
            clear(['B', num2str(i), num2str(j)]);
            v1=genvarname(['W', num2str(i), num2str(j)]);
            eval([v1 '= diag(Mod_Jacobian(j,indH));']);
        end
    end
end

```

```
        cd Jacobians;
        eval(['save ', 'W', num2str(i), num2str(j), ' W', ...
            num2str(i), num2str(j)]); cd ..
        clear(['W', num2str(i), num2str(j)]);
        fprintf('.');
    end
end
fprintf('\n');
end
```

Appendix 5: Multiple erroneous electrode detection code

Appendix 4 lists the Matlab code used for detection of multiple erroneous electrode in 2D EIT. The main function is `elec_multi_detect` which implements the method described in chapter 6. The matrices $\mathbf{B}(e_i, e_j, e_k)$ are calculated by `prep_multi_predictor` function after which the values are saved for future use. The function `add_noise` is used to add simulated noise to selected electrode pair data.

```
function [err,PER]=elec_multi_detect(e,vi,ve,repeat,snr1,elec)
% ELEC_Detect: runs a two erroneous electrode detection method on
% simulated data. The result shows the graph of the estimation for each
% electrode. The electrode with the lowest total erms is assumed to the
% erroneous electrode
%
% e:      Experimental data number
% vi:     Measurement during inspiration or at time t1
% ve:     Measurement during expiration or at time t2, where t2>t1
% repeat: Number of times to repeat experiment
% snr1:   Signal to noise ratio specifying the noise to be added if any
% elec:   Noise is added to data from elec, elec=-2 if there is no
%         noise to be added
%
% err:    estimation error for each electrode in the EIT system
% PER:    Prediction error of experimental data e or if simulation PER
%         for different snr values for each iteration
%
% (C) 2004 Yednek Asfaw
% $Id$

clear all;

DEBUGM=0;

global ELS
n=1;
for r=1:repeat
    p=1;
    for snr=snr1

        %calculate the voltage difference
        if (e==59 | e==60 | e==61)
            z=(vi(:,1) - ve(:,1)); %simulated data already normalized
        else
            z=(vi(:,1) - ve(:,1))./(0.5*(vi(:,1)+ve(:,1)));
        end

        zn=add_noise(elec,z,snr);

        if DEBUGM==1

            %show the amplitude of voltage difference for each pair
            %without noise
            figure,plot(z(ELS),'.')
```

```

xlabel('Index for measurement and injection pair');
ylabel('amplitude of the voltage difference');

%with noise
figure,plot(zn(ELS),'.')
xlabel('Index for measurement and injection pair');
ylabel('amplitude of the voltage difference');

%calculate the conductivity distribution
exp_image=imgr(irec(-zn,zeros(256,1),'filt',2));
filename=['e', num2str(e),'.png'];
cmap=[flipud(fliplr(hot(33)));hot(33);1,1,1];cmap(33,:)=[];
colormap(cmap)
imwrite(exp_image,cmap,filename); %bmpwrite
image(exp_image);
figure,mesh(exp_image)
pause;
end

%start the detection method
for remapped=zn
cd Constructors;
for j=0:15 %for each individual data set
for k=j:15 %select a candidate electrode ei
err(j+1,k+1)=0; %initialize the total erms
for i=0:15 %select an electrode ej, and ek
if i~=j & i~=k & j~=k;
v=genvarname(['B',num2str(i),num2str(j), ...
num2str(k)]);
eval(['load' ...
,'B',num2str(i),num2str(j),num2str(k)]);
%determine the estimation error
err(j+1,k+1)=err(j+1,k+1) ...
+eval(['transpose(remapped)*' v ...
'*remapped;']);
clear(['B',num2str(i),num2str(j) ...
,num2str(k)]);
end
end
if DEBUGM==1
if j~=k
%show estimation error for each ej and ek
disp([j, k, err(j+1,k+1)]);
end
end
end
end
end
cd ..

end
%determine if there is an erroneous electrode in this data set
norm_sample=(err(:)-mean(err(:)))/var(err(:));
for i=1:16
if norm_sample(i)>=0 val=0; else val=norm_sample(i); end
dist(i)=sum(abs(norm_sample-val));
end

%determine the min to max distance ratio and PER
maxdist_ratio(n,p)=min(dist)/max(dist);
PER(n,p)=20*log(maxdist_ratio(n,p));
disp([r snr e maxdist_ratio(n,p) 20*log(maxdist_ratio(n,p))]);
p=p+1;
end
n=n+1;

```

end

```

function prep_multi_predictor(dpos,dvv)
% prep_multi_predictor: calculates the total erms value of all possible
% pair electrodes. This function is run only once. The Constructors are
% save in a folder named Constructor. The result is used by
% elec_multi_detect.m
% dpos: The difference between a pair ie. [0 2] injection pair-> dpos:2
% dvv: Sensitivity matrix (H)
% $Id$

for i=0:15 %estimate electrode ei's data
  for j=0:15
    for k=0:15 %[ej ek] pre-removed electrodes
      if i~=j & i~=k & j~=k;
        %construct the name for the reconstruction matrix
        v=genvarname(['B',num2str(i),num2str(j),num2str(k)]);
        %calculate the reconstruction matrix using
        %prep_predictor
        innerM=prep_predictor(dpos,dvv, i,[j k]);
        eval([v '= innerM;']);
        %save it
        cd Constructors;
        eval(['save ', 'B',num2str(i),num2str(j) ...
            ,num2str(k), ' B',num2str(i),num2str(j),num2str(k) ]);
        cd ..
        clear(['B',num2str(i),num2str(j),num2str(k)]);
      end
    end
  end
  end
  fprintf('\n');
end

```
